Synthesis and Characterisation of Transition Metal Fluorides

Cameron Black

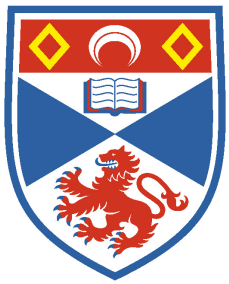

University of
St Andrews

This thesis is submitted in partial fulfilment for the degree of PhD
At the
University of St Andrews

June 2015

SYNTHESIS AND CHARACTERISATION OF TRANSITION METAL FLUORIDES

Cameron Black

A Thesis Submitted for the Degree of PhD
at the
University of St Andrews

2015

Full metadata for this item is available in
St Andrews Research Repository
at:
http://research-repository.st-andrews.ac.uk/

Please use this identifier to cite or link to this item:
http://hdl.handle.net/10023/9652

This item is protected by original copyright

Declarations

I, Cameron Black hereby certify that this thesis, which is approximately 30,000 words in length, has been written by me, and that it is the record of work carried out by me, or principally by myself in collaboration with others as acknowledged, and that it has not been submitted in any previous application for a higher degree.
I was admitted as a research student in September, 2011 and as a candidate for the degree of PhD in August, 2012; the higher study for which this is a record was carried out in the University of St Andrews between 2011 and 2015.

Date _____ Signature of candidate _____

I hereby certify that the candidate has fulfilled the conditions of the Resolution and Regulations appropriate for the degree of PhD in the University of St Andrews and that the candidate is qualified to submit this thesis in application for that degree.

Date _____ Signature of supervisor _____

In submitting this thesis to the University of St Andrews I understand that I am giving permission for it to be made available for use in accordance with the regulations of the University Library for the time being in force, subject to any copyright vested in the work not being affected thereby. I also understand that the title and the abstract will be published, and that a copy of the work may be made and supplied to any bona fide library or research worker, that my thesis will be electronically accessible for personal or research use unless exempt by award of an embargo as requested below, and that the library has the right to migrate my thesis into new electronic forms as required to ensure continued access to the thesis. I have obtained any third-party copyright permissions that may be required in order to allow such access and migration, or have requested the appropriate embargo below.

The following is an agreed request by candidate and supervisor regarding the publication of this thesis:

PRINTED COPY

Embargo on all or part of print copy for a period of one year (maximum five) on the following ground:

- Publication would preclude future publication

Supporting statement for printed embargo request:

Two further papers are still to be published that describe work discussed in the thesis.

ELECTRONIC COPY

Embargo on all or part of electronic copy for a period of one year (maximum five) on the following ground:

- Publication would preclude future publication

Supporting statement for electronic embargo request:

Two further papers are still to be published that describe work discussed in the thesis.

Date_____ Signature of candidate_____

Signature of supervisor _____

Abstract

This thesis reports exploratory studies on the synthesis of new vanadium and copper-containing compounds, with a particular emphasis on preparing new magnetically-active materials with $S = ½$ spin configurations. Eighteen crystal structures are reported, sixteen of which represent new compounds. These materials were studied for magnetic behaviour where appropriate.

The sixteen vanadium-containing compounds were prepared using either the hydrothermal, solvothermal or ionothermal synthesis methods at temperatures ranging from 60 ^{o}C to 200 ^{o}C. Inorganic cations and organic moieties were used as templating agents to direct the structures, often targeting potentially frustrated lattices based on triangular motifs by using 'triangular' templating molecules such as guanidine. Solvent choices, as well as reactant ratios were all varied in order to produce the new oxide, fluoride and oxyfluoride compounds of vanadium.

Three families of vanadium compounds were prepared from these methods; a family of 1D vanadium (IV) oxfluoride ladder compounds of general formula $AVOF_3$ ($A = K^+$, Rb^+, Cs^+ or NH_4^+), and a family of 1D vanadium fluoride chain compounds of general formula A_2VF_5 ($A = K^+$ or NH_4^+). The third family is comprised of three vanadium-containing compounds of varying dimensionality that share guanidine as the common organic moiety. Several miscellaneous compounds of vanadium such as clusters and a new V (IV) layer were synthesized, and are reported.

The two copper containing compounds, analogous to the pseudo-kagome compound, $Cu_3Bi(SeO_3)_2O_2Br$, were prepared via solid-state techniques. A detailed neutron diffraction study was carried out on the two compounds to measure the evolution of the magnetic properties from room temperature down to 2.5 K. Representational analysis was utilised in order to provide a detailed magnetic model of the compounds.

Acknowledgements

I would like to thank my supervisors Phil and Russell, for giving me the opportunity to work on this project. Phil's guidance and ideas were an invaluable help during my time at St Andrews University.

Prof. Alex Slawin and Dr. David Cordes are thanked for their help in collecting some of the single crystal data, as well as for advice on crystallography. Dr. Winfried Kocklemann is thanked for his help with data collection at ISIS. Thank you to Dr. Lucy Clark for assistance collecting magnetic data, as well as for help with the analysis. Also, Dr. Peter Berdonosov is thanked for his assistance in sample preparation.

Thanks to all of my friends in and out of chemistry. I am particularly grateful to Irene for keeping me constantly entertained in the lab with Italian lessons, and Sam for our lengthy afternoon chats and Freddo bets.

Finally I would like to say thank you to my family for their continued support and encouragement.

Contents

1.0 Introduction

The work that comprises this thesis is concerned with the synthesis of new transition metal oxides, fluorides and oxyfluorides. The solvothermal, hydrothermal, ionothermal and solid state synthesis methods used to create these compounds will be discussed along with any interesting physical properties that were measured. This chapter will introduce the concept of building units and the effect of structure on material properties, discussing known compounds of varying structure type that display interesting physical properties.

1.1 Building Units

The term 'building unit' refers to the motif that makes up a full structure regardless of symmetry.[1-3] This is, however, not the same as an asymmetric unit, which refers to crystallographic sites and, by extension, symmetry. The concept of building units has been used for nearly eight decades, and can be thought of as the building blocks of a structure, regardless of their size in relation to the final structure (in a similar manner to the bricks used to build a house).[1] Zeolites are a good example of structures in which building units can be easily viewed as they are often made up of simple units; MO_4 tetrahedra, where M = silicon or aluminium (Fig. 1. 1). These tetrahedral building units can then be assembled into more complicated secondary building units such as the 6-ring cluster (Fig. 1. 2).

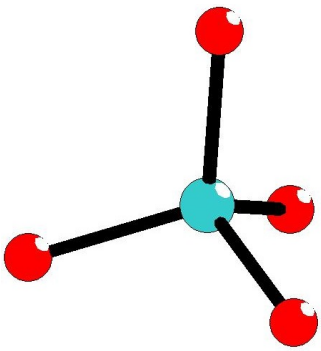

Fig. 1. 1: The Al/SiO_4 tetrahedral unit found in zeolites.

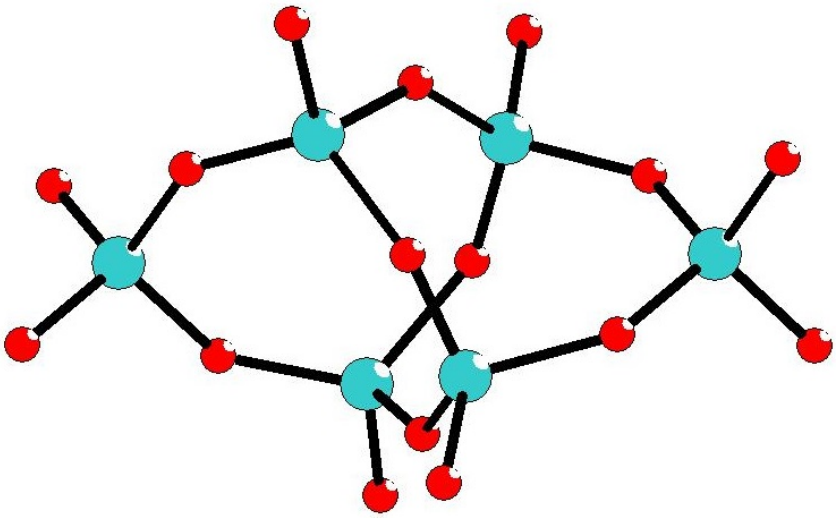

Fig. 1. 2: A 6-ring cluster comprised of simple MO_4 building units.

1.1.2 Building Units in Oxyfluorides

Oxide, fluoride and oxyfluoride building units come in a variety of topologies. These include 5-coordinate square-base pyramids, 6-coordinate octahedra and 8-coordinate square antiprisms (Fig. 1. 3). These units can have an out-of-centre distortion under certain circumstances, for example due to a short metal-oxide bond. In octahedral building units, these distortions can often be the cause of any interesting physical properties in the material. When an octahedral unit with a metal centre becomes distorted, it can cause the gap between the lowest unoccupied molecular orbitals and the highest occupied molecular orbitals to decrease.

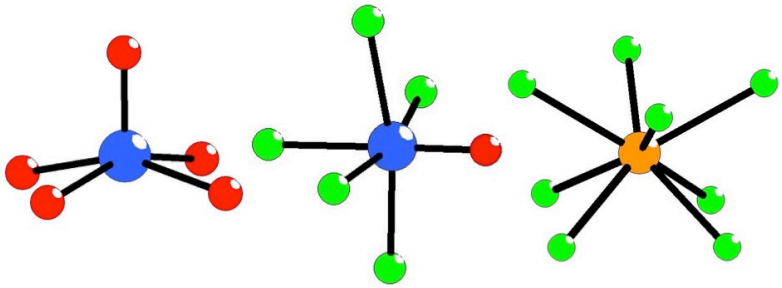

Fig. 1. 3: 5-coordinate MoO_5, 6-coordinate VOF_5 and 8-coordinate TaF_8.

If the gap becomes small enough, the two orbitals can be stabilised by a Jahn-Teller effect, hence a larger distortion produces a smaller orbital gap, which in turn has

a greater effect on the physical properties displayed by the material.[2] These out-of-centre distortions can have effects on the symmetry of the overall structure, leading to non-centrosymmetric crystal classes.[4] These non-centrosymmetric structures are of particular interest as they can posses a large array of physical properties due to the formation of a dipole moment caused by the distortions, such as piezoelectricity, pyroelectricity or optical activity.[5]

1.2 Structural properties

In the following subsections, certain materials of varying dimensionality will be discussed along with their structural and physical properties. This is not intended as a comprehensive review due to the scope of such an undertaking. Recently, Leblanc et al. have published a review article, covering most transition metal fluorides and oxide-fluorides.[6]

1.2.1 0D structures

1.2.1.1 Monomers

Monomers are the simplest form of MX_y structure, where M = any early transition metal, X = oxygen, fluorine, nitrogen or chlorine and y = a non-zero integer. Many mineral classes, such as elpasolite, are made up of A_3MX_6 structures containing momomeric inorganic units. K_2NaAlF_6[7], Cs_2NaGaF_6[8], Ba_2NiTeO_6[9], and $[NH_4]_3WO_3F_3$[10] are all examples of this mineral type. These each have isolated metal oxide, fluoride or oxyfluoride octahedral units spaced by the counter cations, one of which sits in a 6-coordinate site itself, making these minerals perovskite-like in nature. This is easily observed in Li_3TiF_6[11] which has two Li^+ sites that are 8-coordinate and one that is 6-coordinate, separating this TiF_6 octahedral units (Fig. 1. 4). Li_3TiF_6 was prepared at 820 °C, and crystallises in the monoclinic $C2/c$ space group with Ti^{3+}, S = ½ oxidation state. Its magnetic properties were measured, and its extrapolated μ_{eff} value (1.83 μB) correlates well with the spin

only value for μ_{eff}(1.73 μB).

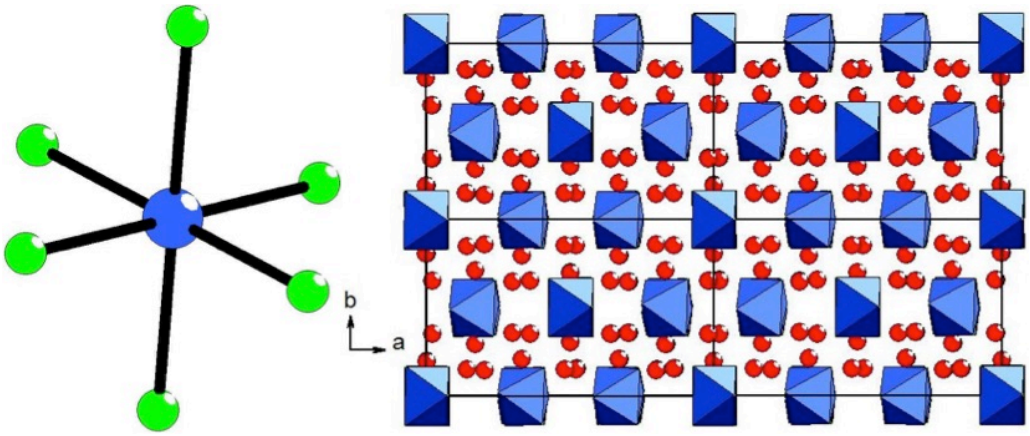

Fig. 1. 4: The $Ti(III)F_6$ octahedral unit, and the extended 2x2 unit cell of $Li_3Ti(III)F_6$ viewed along axis *c*.

The Na_2TiF_6 structure crystallises in the *P*1 space group with Ti^{4+}, $S = 0$, oxidation state.[12] This structure is also composed of isolated TiF_6 octahedral units spaced by Na^+ cations (Fig. 1. 5). The space group *P*1 is non-centrosymmetirc, which means that, while it is magnetically inactive, Na_2TiF_6 should exhibit second harmonic generation. This is a property which nearly all crystal structures that are non-centrosymmetric are thought to exhibit.[13]

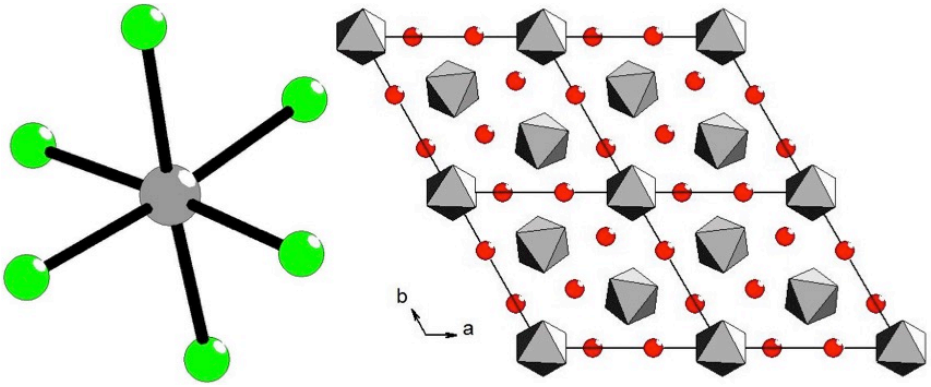

Fig. 1. 5: The TiF_6 octahedral unit, and the extended 2x2 unit cell of $Na_2Ti(IV)F_6$ viewed along axis *c*.

The material $[(CH_3)_4N]OsO_3F_3$[14] crystallises in the monoclinic $C2/c$ space group, and is another example of a structure that consists solely of octahedral

monomeric units. This is a hybrid compound, so instead of being separated by alkali metal cations, the octahedral units are surrounded by $[(CH_3)_4N]$ organic moieties (Fig. 1. 6). It is also not uncommon to see materials that form chains of monomers by linking them together either via hydrogen bonding in $[C_4H_{12}N_2][TiF_5(H_2O)]_2$[15] or via an intermediate species in $[Ag_3MoO_3F_3][Ag_3MoO_4]Cl$.[16] These are still considered to be 0D structures, not extended inorganic compounds (e.g. 1D chains), due to the connectivity not occurring between polyhedral units of the same metal centre.

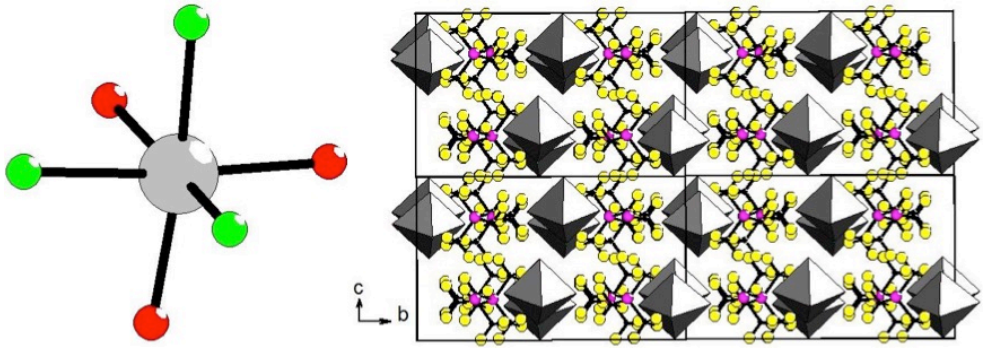

Fig. 1. 6: The $Os(VIII)O_3F_3$ octahedral unit, and the extended 2x2 unit cell of $[(CH_3)_4N]OsO_3F_3$ viewed along axis *a*.

1.2.1.2 Dimers

When two monomers are connected, either via corners, edges or faces, dimer units are produced. These are good examples of building units that make up a great number of fluoride and oxyfluoride structures, such as $Na_5Zr_2F_{13}$[17], $Cs[C_4H_{12}N]pV_2O_2F_8(H_2O)]$[18] and $[C_4H_{12}N_2]_2[Ti_2OF_{10}].2H_2O$[15], which contain corner-sharing dimers. $K_5Eu_2Si_4O_{13}F$[19] is another example of a corner-sharing dimer. The structure is comprised of octahedral $EuO_5F_{1/2}$ units (where the ½ indicates the shared, bridging fluorine atom), bridging to other europium-centred units through fluorine (Fig. 1. 7).

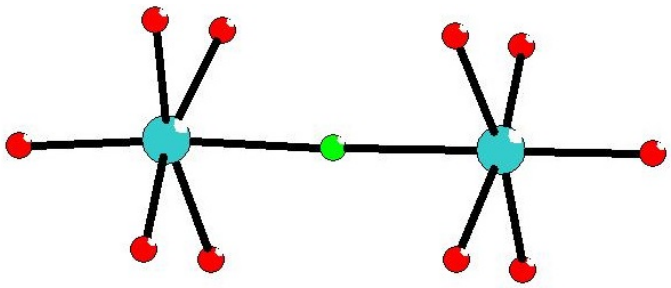

Fig. 1. 7: The $Eu(III)_2O_{10}F$ dimer building unit.

These $Eu_2O_{10}F$ units are connected by SiO_4 tetrahedral units into the full 3D structure (Fig. 1. 8). This is another example of how 0D structures can be connected by other polyhedral units into structures with higher dimensionality. $Cs_2Zn(H_2O)_6(Zr_2F_{12})^{20}$ is comprised of 7-coordinate zirconium-centred units that are connected into edge-sharing dimers via fluorine atoms (Fig. 1. 9). When fully packed, the dimer units are separated by the $Zn(OH_2)_6$ octahedral units as well as the large Cs^+ cations (Fig. 1. 10).

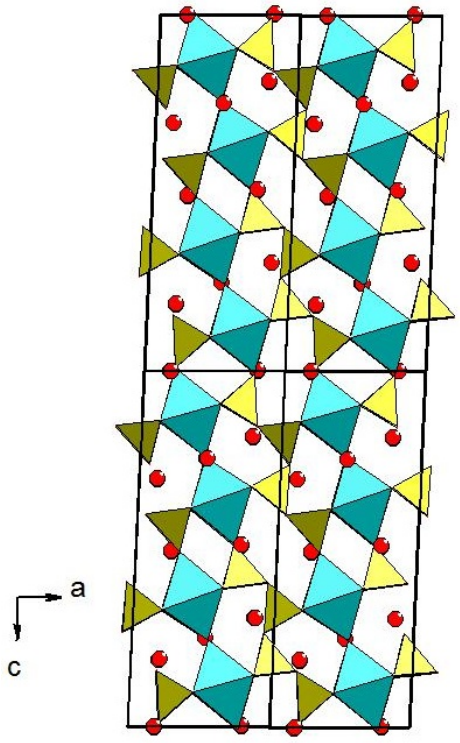

Fig. 1. 8: The extended 2x2 unit cell of $K_5Eu(III)_2Si_4O_{13}F$, showing the packing of the K^+ cations and the bridging of the dimers via SiO_4.

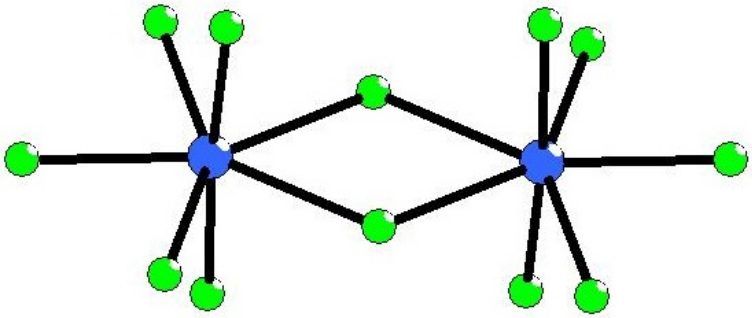

Fig. 1. 9: The $Zr(IV)_2F_{12}$ edge-sharing dimer unit.

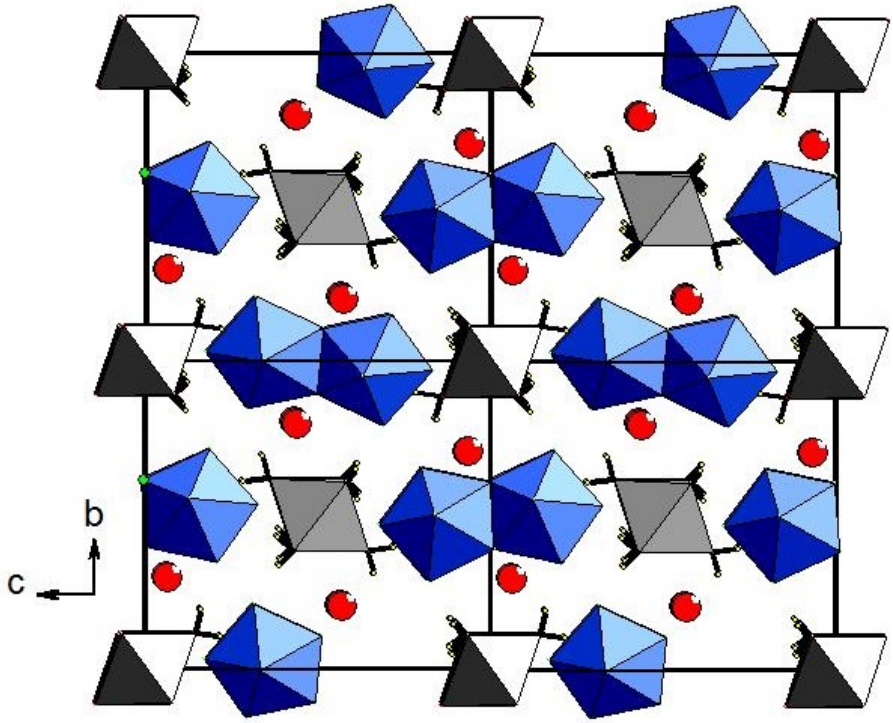

Fig. 1. 10: The extended 2x2 unit cell of $Cs_2Zn(H_2O)_6(Zr(IV)_2F_{12})$, showing the full packing of the structure. The Zr_2F_{12} dimers are separated by the $Zn(H_2O)_6$ octahedral units and the Cs^+ cations.

1.2.1.3 Trimers

There are relatively few transition metal oxyfluoride trimer structures compared with dimers.[6] A few examples of such structures include $K[C_4H_{12}N][VOF_4]_3$[18], $K_2Cu(PO_3F)_4$[21] and $(NH_4)_4Fe_3(OH)_2.[(HPO_4)_4F_2]$.[22] Trimeric transition metal

structures are desirable due to their structural properties, which can lead to three-fold symmetry which, in turn, can lead to magnetic frustration in the appropriate oxidation state (e.g. $S = ½$). $(NH_4)_4Fe_3(OH)_2.[(HPO_4)_4F_2]$ is comprised of $Fe_3(OH)_6O_8F_2$ octahedral units that are linked via fluorine into linear trimers (Fig. 1. 11) These are linked via HPO_4 tetrahedral units to form the full 3D structure with the NH_4 units occupying the interstitial sites (Fig. 1. 12). $K[C_4H_{12}N][VOF_4]_3$ is comprised of $V_3O_3F_{12}$ octahedral units bridged via fluorine into trigonal trimer units (Fig. 1. 13). These trigonal units stack in a manner that is slightly offset from each other (Fig. 1. 13), and are surrounded by the $[C_4H_{12}N]$ units and the K^+ cations (Fig. 1. 14). This is an example of a structural configuration that could lead to magnetic frustration, but the V^{4+} oxidation state and is diamagnetic.

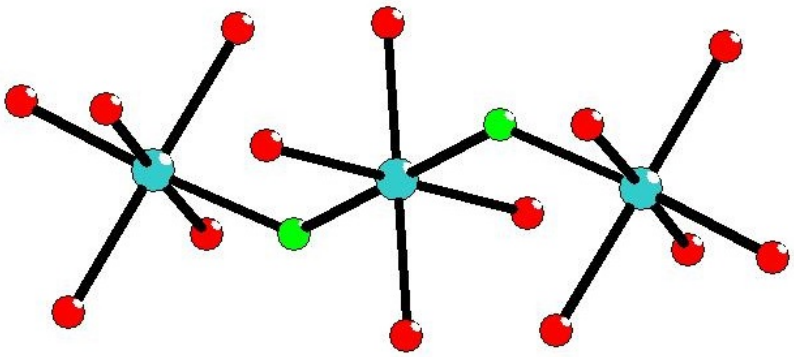

Fig. 1. 11: The linear trimer unit in $(NH_4)_4F(III)e_3(OH)_2.[(H_3PO_4)_4F_2]$

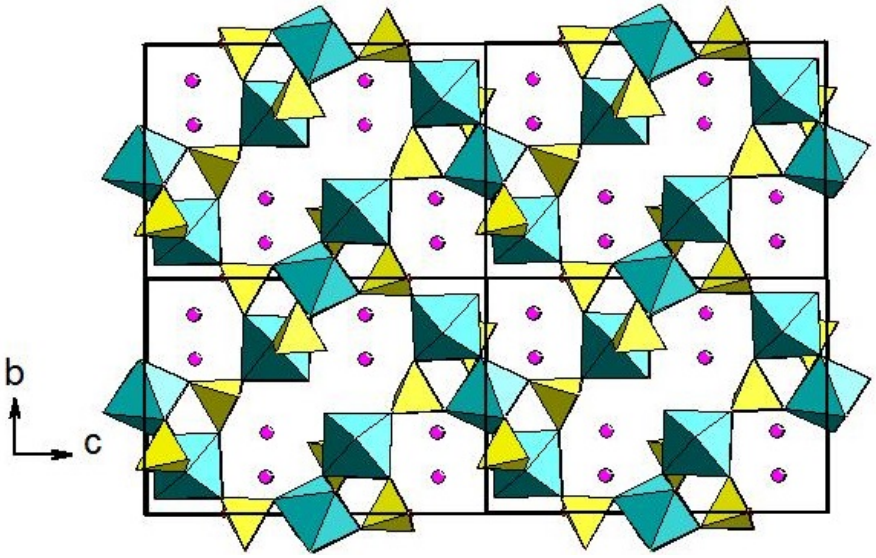

Fig. 1. 12: The packed structure of $(NH_4)_4Fe(III)_3(OH)_2.[(H_3PO_4)_4F_2]$, showing the 3D connectivity via H_3PO_4

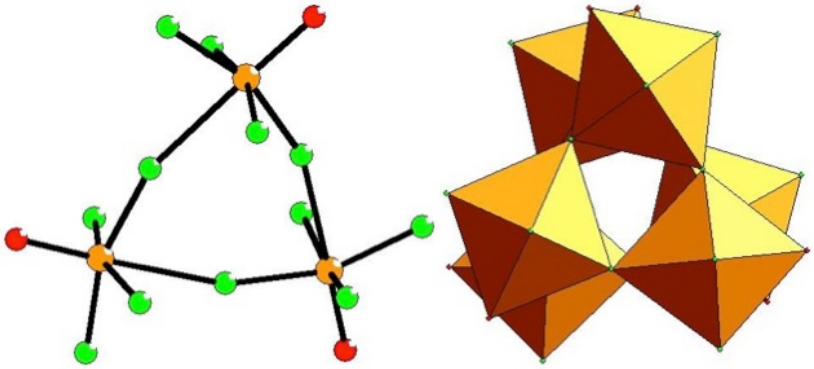

Fig. 1. 13: The trigonal trimer unit in $K[C_4H_{12}N][V(V)OF_4]_3$ and the staggered packing present.

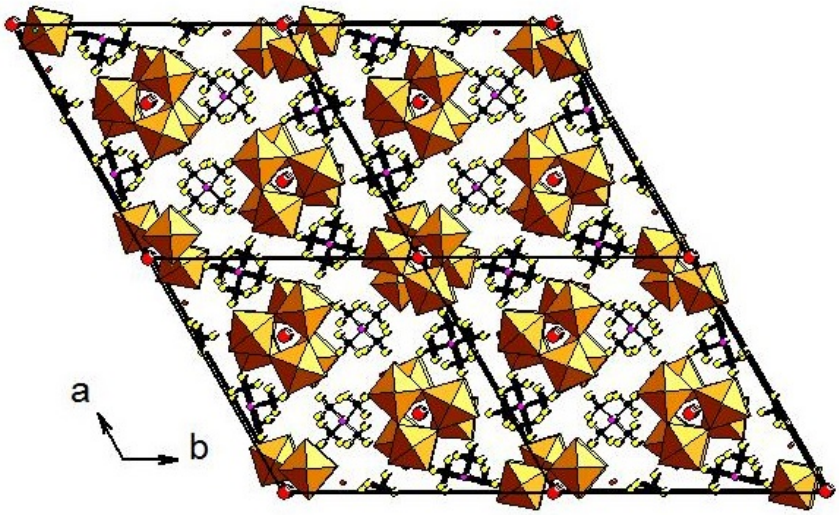

Fig. 1. 14: The extended 2x2 unit cell in $K[C_4H_{12}N][V(V)OF_4]_3$ showing the fully packed structure, highlighting the trimer units surrounded by the organic moieties and K^+ cations.

1.2.1.4 Tetramers

Examples of tetramers include the completely fluorinated $[CH_8N_4][ZrF_6].H_2O$[23] which is comprised of Zr_4F_{24} square planar tetramer building units (Fig. 1. 15), these are surrounded by the protonated aminoguanidinium cations and the water molecules. The tetramer is made up of four ZrF_8 Archimedean antiprisms (Fig. 1. 16), sharing square-faced edges.

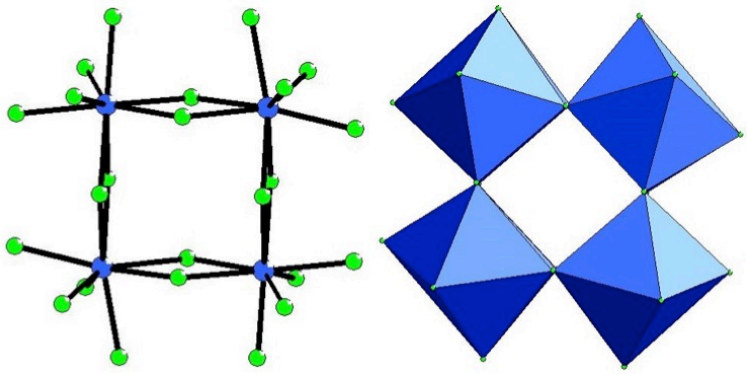

Fig. 1. 15: The Zr_4F_{28} tetrameric building units in $[CH_8N_4][ZrF_6].H_2O$, with a polyhedral representation on the right.

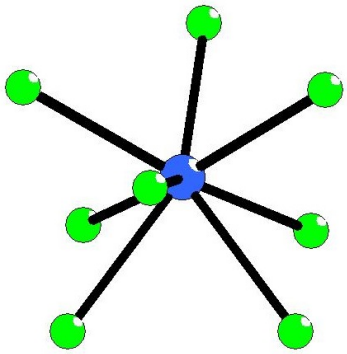

Fig. 1. 16: The ZrF_8 Archimedean antiprism that makes up the tetramers in $[CH_8N_4][ZrF_6].H_2O$

$Os_2O_3F_7$[24] and $Ba_3V_2O_4F_8$[25] are both good examples of oxyfluoride tetramer structures. $Os_2O_3F_7$ is comprised of tetrameric units made up of two osmium (VIII) octahedral units and two osmium (V) octahedral units, $Os(VIII)_2Os(V)_2O_6F_{14}$ (Fig. 1. 17). The tetramers are buckled in such a way that they are distorted from the square planar array seen in $[CH_8N_4][ZrF_6].H_2O$.

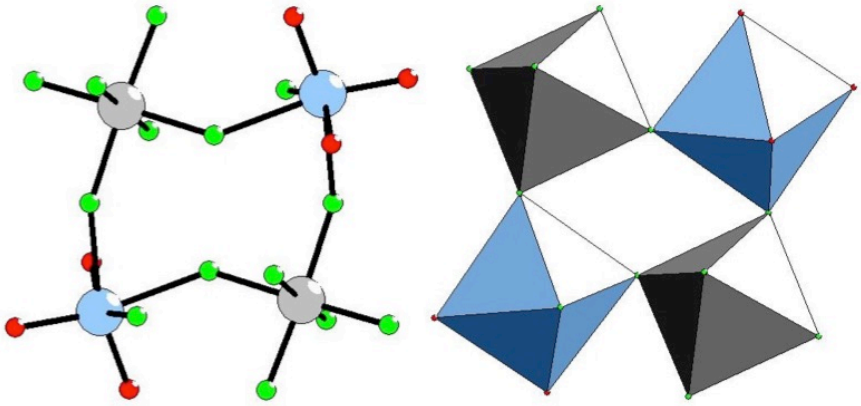

Fig. 1. 17: The buckled tetramer unit, $Os(VIII)_2Os(V)_2O_6F_{14}$, that occurs in $Os_2O_3F_{14}$ showing the Os(VIII) in grey and the Os(V) in pale blue, with a polyhedral representation on the right.

1.2.1.5 Hexamers

$Cs_4Li_2Mo_6O_{18}F_6$ and $Cs_4Na_2Mo_6O_{16}F_6$[26] are interesting materials, as the hexamer building unit that comprises them is relatively uncommon compared to

monomer, dimer and tetramer building units. $Cs_4Li_2Mo_6O_{18}F_6$ is built up of six MoO_4F_2 octahedral units that share edges with two neighbouring units to form a 6-membered inorganic ring (Fig. 1. 18).

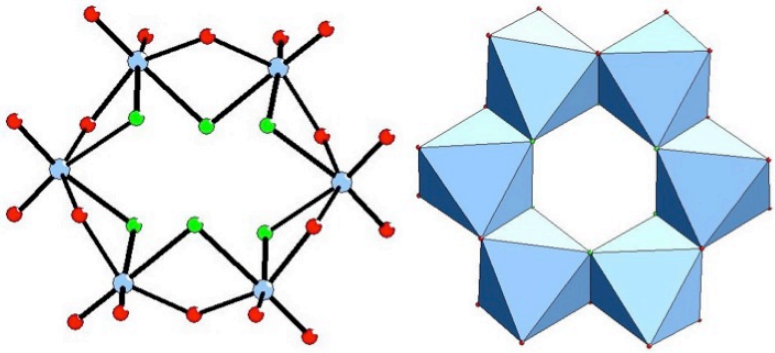

Fig. 1. 18: The $Mo_6O_{18}F_6$ face-sharing hexamer building unit in $Cs_4Li_2Mo_6O_{18}F_6$, with a polyhedral representation on the right.

The Mo^{6+} is d^0 and therefor magnetically inactive, and it is surrounded by the large, 8-coordinate, Cs^+ cations, and the smaller, 4-coordinate, Li^+ cations (Fig. 1. 19).

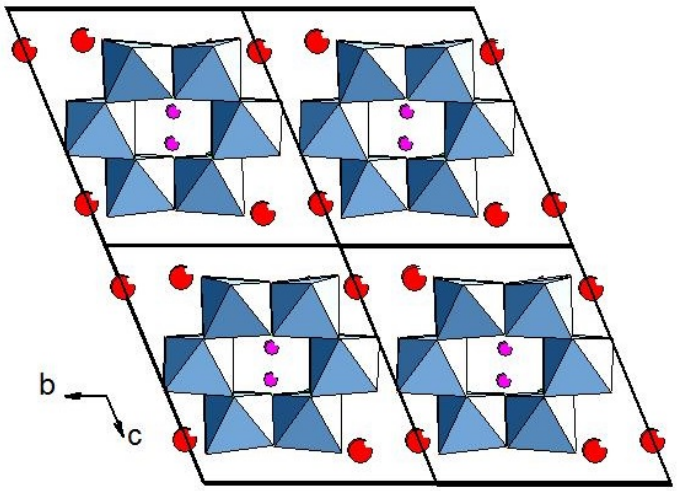

Fig. 1. 19: The extended 2x2 unit cell in $Cs_4Li_2Mo_6O_{18}F_6$ showing the packing of the hexamer units surrounded by the 8-coordinate Cs^+ (red) cations and the 4-coordinate Li^+ (purple) cations occupying the centre of the rings.

1.2.1.6 Octamers

Octamers, also known as "double 4-rings" are common building blocks in zeolites such as in $Na_2Al_2Si_3O_{10}\cdot 2H_2O$, where they tend to be tetrahedral AlO_4 or SiO_4 units.[27] In the case of transition metal fluoride compounds, double 4-rings of octahedral units are more common such as in the materials $K_4Ti_8F_{36}$ and $Rb_4Ti_8F_{36}$.[28]; both compounds consist of TiF_6 octahedral units that share corners with three neighbours to form the octameric unit Ti_8F_{36} (Fig. 1. 20).

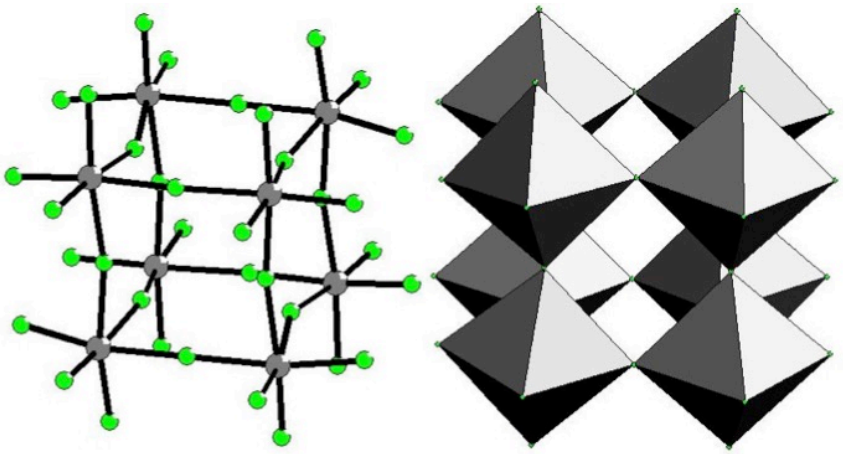

Fig. 1. 20: The $Ti(IV)_8F_{36}$ building unit that makes up $K_4Ti_8F_{36}$ and $Rb_4Ti_8F_{36}$.

1.2.2 1D structures

1.2.2.1 Chains

In 1D structures, single chains of corner or edge-sharing units are one of the most common building blocks. $[NH_4]_2TiOF_4$[29], NH_4TiF_5[30], K_2VOF_4[31], $K_2VO_2F_3$[32], $KCu_2(OH)(PO_3F)_2(H_2O)$[21] and ReO_3F[33] are all examples of corner and edge-sharing 1D chains.

$KCu_2(OH)(PO_3F)_2(H_2O)$ is an example of a near-linear chain, comprised of edge-sharing CuO_6 octahedral units (Fig. 1. 21). The chains are connected to one another through PO_3F tetrahedral units to form layers (Fig. 1. 22).

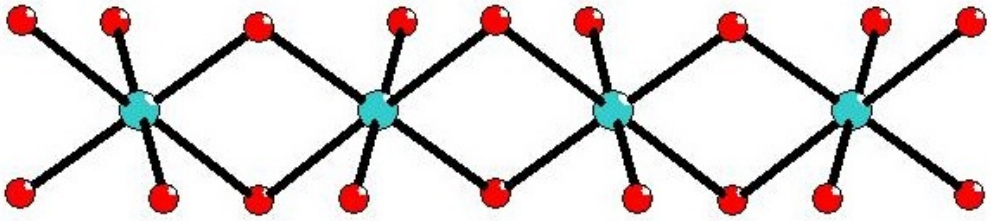

Fig. 1. 21: The face-sharing linear chain of $Cu(II)O_2O_{4/2}$ octahedral units in $KCu_2(OH)(PO_3F)_2(H_2O)$.

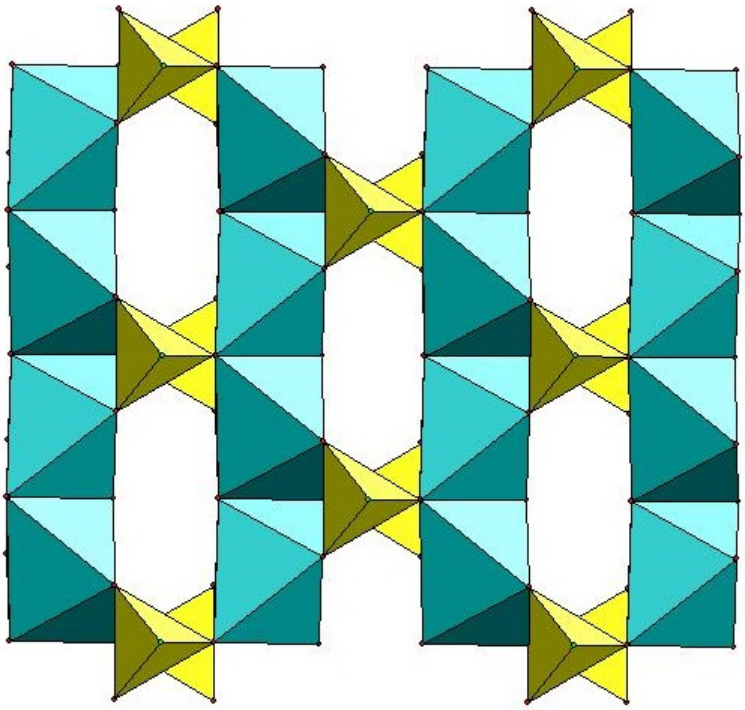

Fig. 1. 22: The 2D layer built up of CuO chains connected to each other vis PO_3F tetrahedral units in $KCu_2(OH)(PO_3F)_2(H_2O)$

Whereas K_2VOF_4 and NH_4TiF_5 both have more zig-zag type corner-sharing chains (Fig. 1. 23). K_2VOF_4 crystallises in the orthorhombic *Pnma* space group, and packs with the chains running parallel with axis *b*, surrounded by the K^+ cations (Fig. 1. 24).

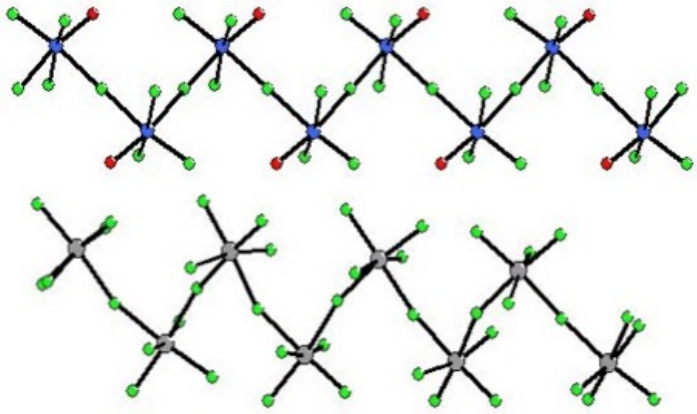

Fig. 1. 23: The zig-zag corner-sharing chains of $V(IV)OF_3F_{2/2}$ (top) in K_2VOF_4 and $TiF_4F_{2/2}$ (bottom) in NH_4TiF_5.

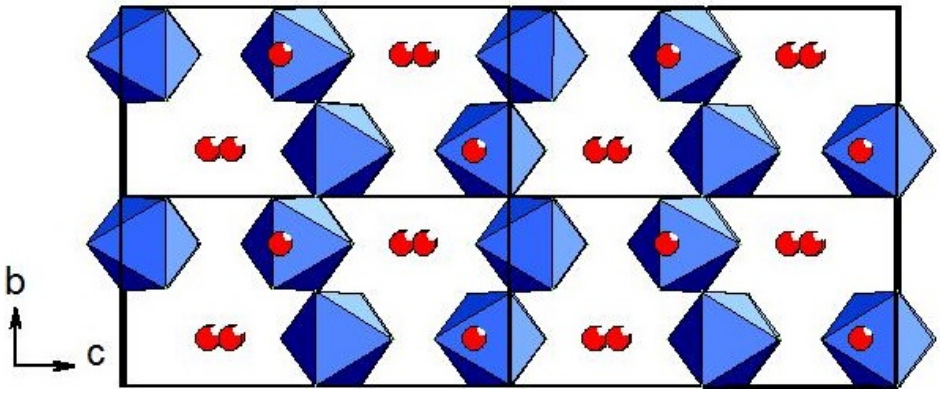

Fig. 1. 24: The extended 2x2 unit cell of K_2VOF_4 showing the packing of the chains, running parallel with axis *b*, surrounded by the K^+ cations.

The compound ReO_3F is another example of a 1D compound that exhibits edge-sharing chains. These chains are not linear like in $KCu_2(OH)(PO_3F)_2(H_2O)$, but have a more zig-zag nature (Fig. 1. 25).

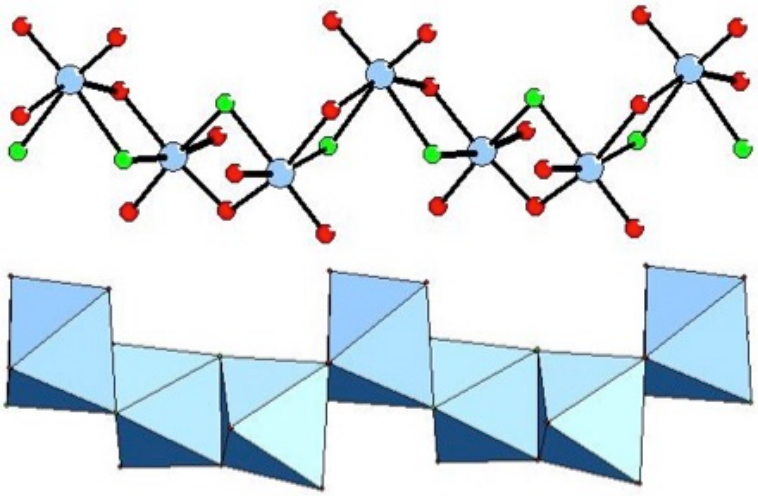

Fig. 1. 25: The zig-zag edge-sharing chains of $ReO_2O_{2/2}F_{2/2}$ octahedral units in the ReO_3F structure.

Chains can also be formed from dimer, trimer, tetramer and octamer units etc. These units tend to share corners with other units and form what are referred to as ladder or tunnel type structures in the case of α-CrF_4[34] (Fig. 1. 26) and β-CrF_4[35] (Fig. 1. 27) respectively.

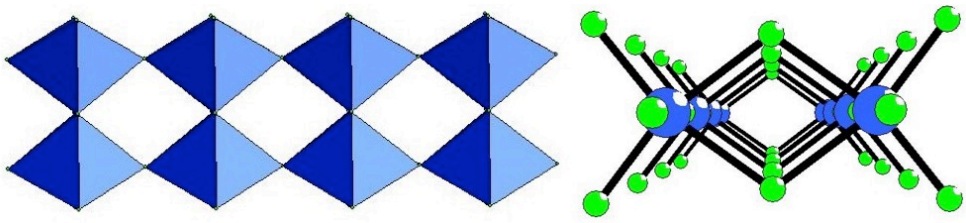

Fig. 1. 26: The corner-sharing ladder-like chain of $Cr(IV)_2F_4F_{4/2}$ edge-sharing dimer units in α-CrF_4.

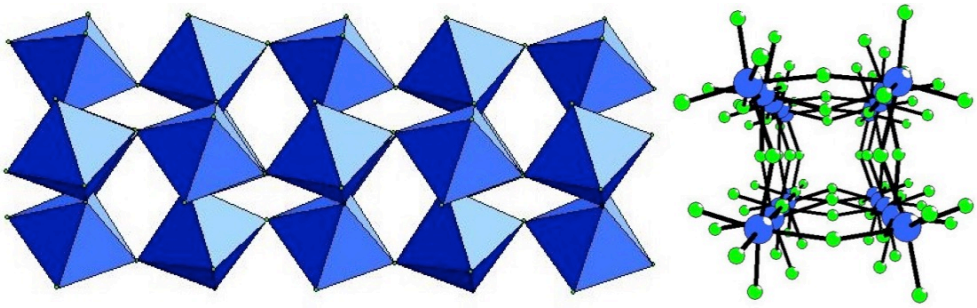

Fig. 1. 27: The corner-sharing tunnel-like chain of $Cr(IV)_4F_8F_{4/2}$ corner-sharing tetramer units in β-CrF_4.

1.2.3 2D structures

$BaMnF_4$[36] is a layered structure based around an octahedral building unit. Four $Mn(II)O_6$ octahedral units share corners to form the tetramer, which share corners with other tetramers to form the layer (Fig. 1. 28). The layers lie perpendicular to the *b* axis, and are separated by large Ba^{2+} cations (Fig. 1. 29). $KTiF_4$[37] is another compound that shows structural similarities to $BaMnF_4$, in that it is a 2D layer built up of tetrameric TiF_6 building units.

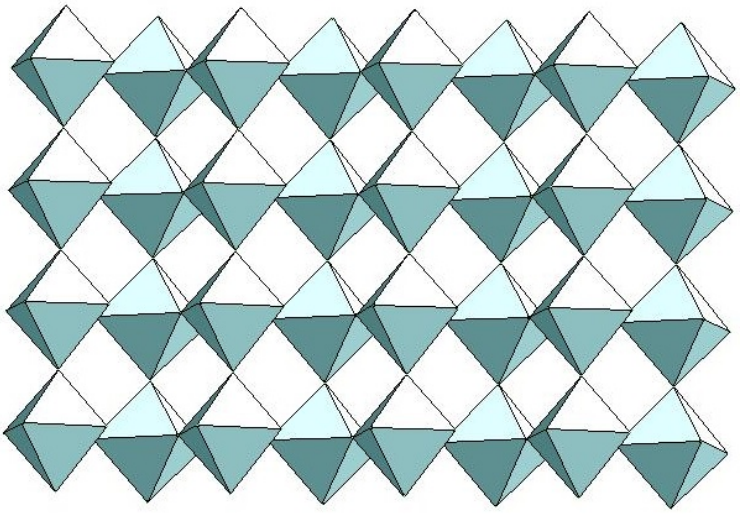

Fig. 1. 28: The $Mn(II)F_6$ octahedral units that corner-share to form the layer in $BaMnF_4$.

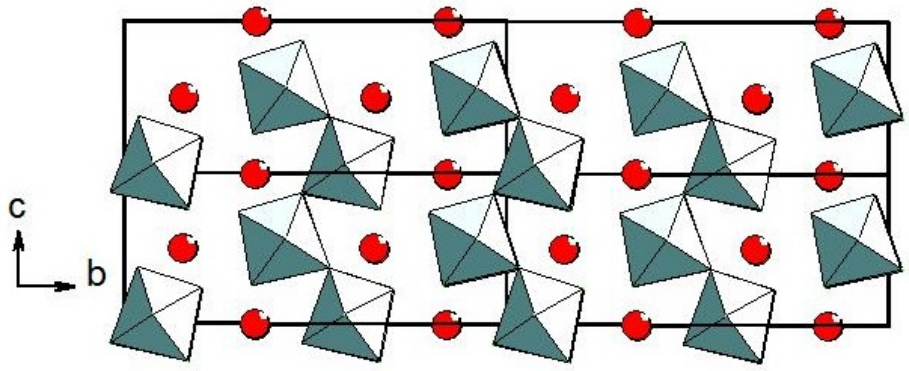

Fig. 1. 29: The packed 2x2 unit cell of $BaMnF_4$ viewed down axis *a*, showing the zig-zag nature of the layers parallel to axis *c*. The layers are separated by the large barium cations along axis *b*.

Layered compounds that are built up of triangular motifs, trimers, are of great interest due to potential magnetic frustration. Compounds such as $ZnCu_3(OH)_6Cl_2$[38] and $Cs_2ZrCu_3F_{12}$[39] and $KFe_3(OH)_6(SO_4)_2$[40] all form structures based on the kagome lattice. These compounds are based on trigonal building blocks that connect to form an infinite layer of hexagons and triangles (Fig. 1. 30).

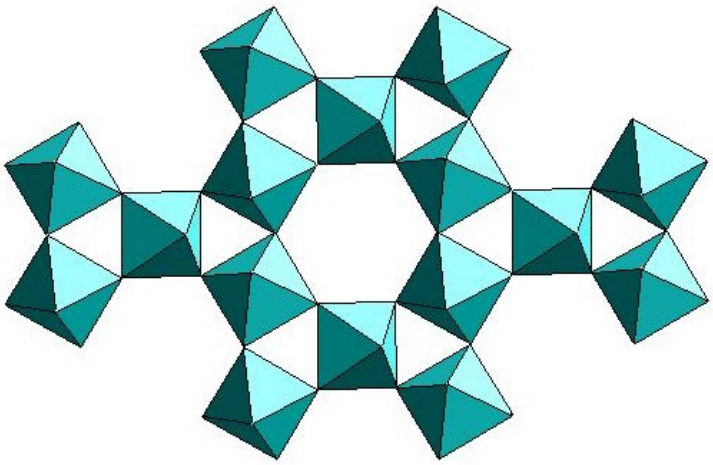

Fig. 1. 30: The kagome layer, built up of trigonal units to form an infinite layer of hexagons and triangles.

In $KFe_3(OH)_6(SO_4)_2$ (jarosite) the trigonal units are mono-capped by the sulphate tetrahedral units (Fig. 1. 31). Jarosite crystallises in the trigonal $R\bar{3}m$ space group with the sulphate-capped kagome layers forming in the *ab* plane, surrounded by the K^+ cations (Fig. 1. 32).

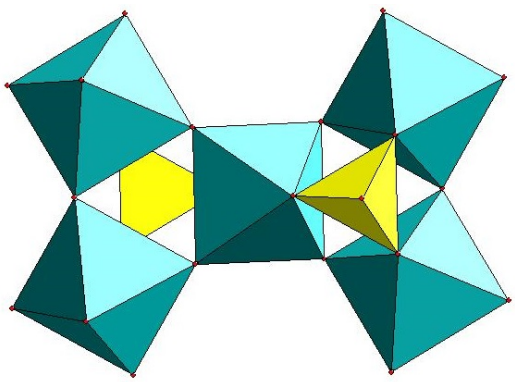

Fig. 1. 31: The sulphate-capped trigonal units as seen in $KFe_3(OH)_6(SO_4)_2$

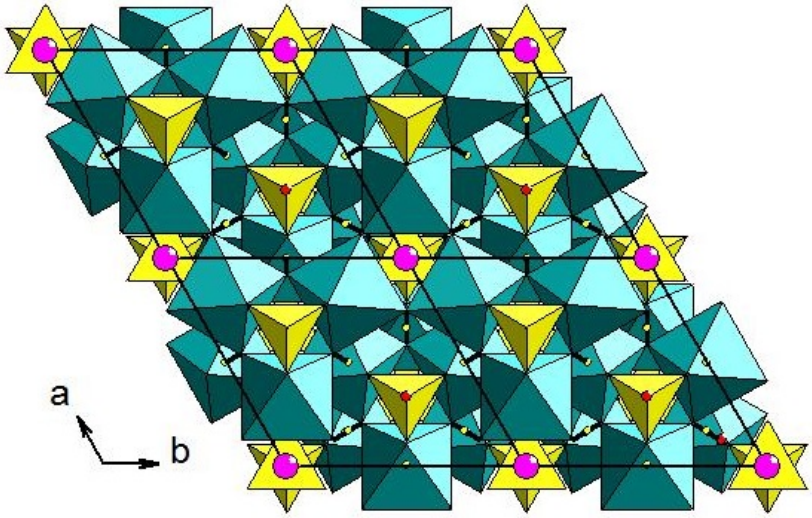

Fig. 1. 32: The extended 2x2 cell of $KFe_3(OH_6)(SO_4)_2$ viewed along axis *c*. The kagome layers lie along the *ab* plane, with the K^+ cations lying in the interstitial sites.

1.2.4 3D structures

FeF_3 is a 3D network of corner-sharing forming the perovskite structure (Fig. 1. 34). This is a very condensed structure, with Fe – Fe distances ranging from 3.733 A to 3.844 Å. The space in the channels is not occupied by any cationic species normally associated with the ABX_3 structure.

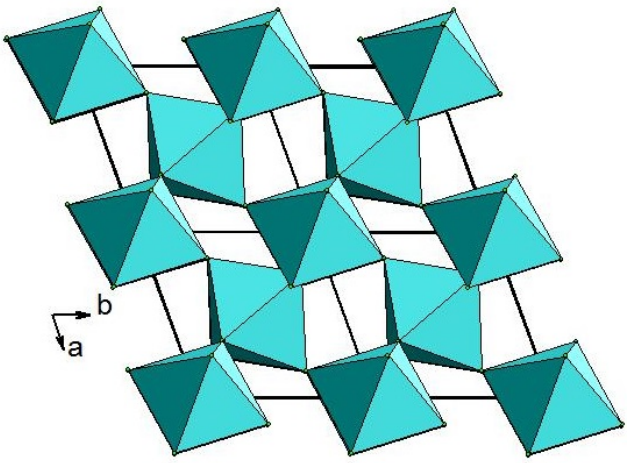

Fig. 1. 33: The 3D structure of FeF_3 viewed down axis *c*.

$CsCoF_3$ is a 3D compound that is based on the face-sharing Co_3F_{12} trimer unit (Fig. 1. 34). These trimers share corners with other units to build the full 3D structure with large Cs^+ cations occupying the spaces in the network (Fig. 1. 35). The Cs – Co distances in the network are 3.714 Å, which is around the same distance as the Fe – Fe distances in FeF_3. The Co – Co distances are interesting in this structure as they are much shorter within the trimer, 2.768 Å, compared to the distance between trimers, 4.098 Å.

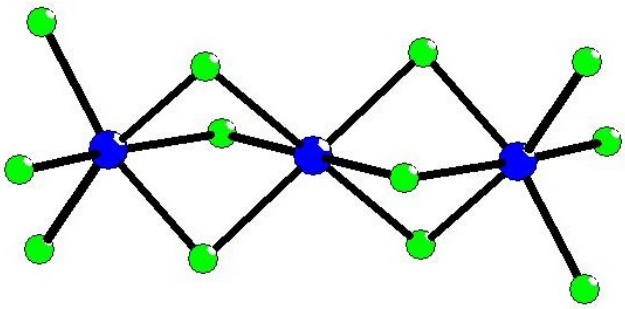

Fig. 1. 34: The face-sharing linear trimer unit Co_3F_{12}.

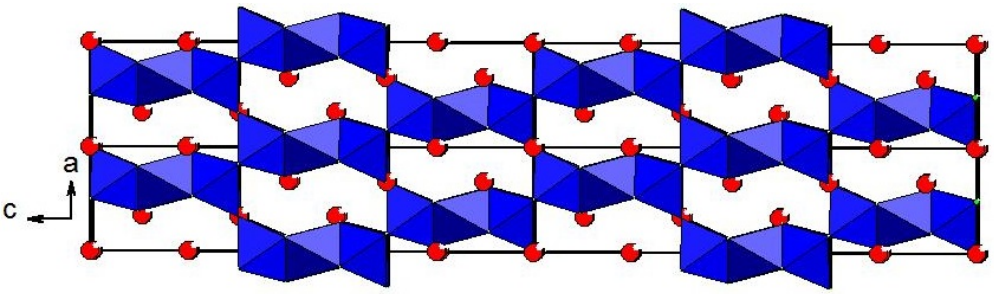

Fig. 1. 35: The packed 2x2 unit cell of $CsCoF_3$ viewed along axis *b*, showing the trimer units corner-sharing with each other and the Cs^+ cations occupying the empty spaces.

These are just a few examples of the vast array of transition metal oxide, fluoride and oxyfluoride compounds that have been reported in the literature. The next section of this chapter will discuss, briefly, the magnetic properties that transition metal compounds can exhibit.

1.3 Physical properties

Transition metal fluoride and oxyfluoride compounds have an abundance of useful physical properties, ranging from use as flame retardants to toothpaste and enamel protection. This project is mainly concerned with the magnetic properties of such materials, which will be briefly discussed in this section.

1.3.1 Magnetism

Magnetic behaviour is a phenomenon that occurs in many inorganic solids. Materials that exhibit magnetic properties are ideal for fundamental study and technological application.

1.3.1.1 Types of magnetism

Magnetism arises from the spin and orbital motions of electrons. At higher temperatures, materials can be divided into two distinct classes; diamagnetic substances and paramagnetic substances. Diamagnetism is a property of any substance in which all electrons are paired. These substances are slightly repelled by magnetic fields. Paramagnetic substances have unpaired electrons, which are randomly aligned at higher temperatures, and undergo attraction in a magnetic field.

In solid materials, where there are ordered lattices, the unpaired electrons of individual metal centres can interact with each other, giving specific electron alignments. Most transition metals have partially filled d-orbitals, which often have unpaired electrons. At higher temperatures, these unpaired electrons tend to be randomly aligned, giving rise to paramagnetic behaviour (Fig. 1. 36). At lower temperatures, the ordering of magnetic moments can occur in three ways;

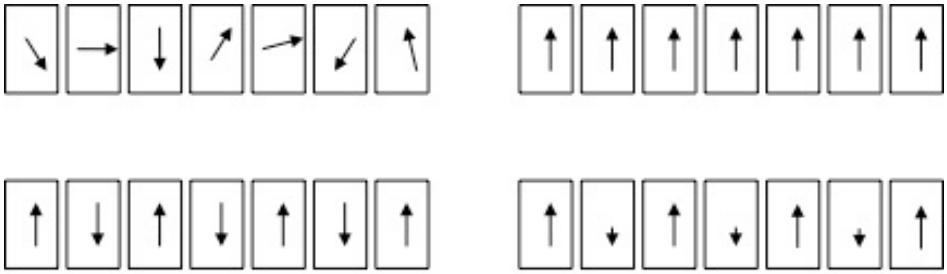

Fig. 1. 36: Basic types of magnetic ordering: (top left) randomly aligned spins of a paramagnet, (top right) parallel spins of a ferromagnet, (bottom left) antiparallel spins of an antiferromagnet and, (bottom right) the unequal antiparallel spins of a ferrimagnet.

ferromagnetic, antiferromagnetic and ferrimagnetic (Fig. 1. 36) depending on how the electron spins align. In ferromagnetic materials, the electron spins interact so that they align parallel with each other, resulting in an overall magnetic moment, while in antiferromagnetic materials the spins align antiparallel, resulting in a zero magnetic moment. If the spins align antiparallel, but are unequal in the two orientations, an overall magnetic moment occurs, but the behaviour is ferrimagnetic.[41]

1.3.1.2 Materials in a magnetic field

If diamagnetic or paramagnetic materials are placed in a magnetic field, *H*, they will each show different types of magnetic induction, *B*. In the diamagnetic sample the magnetic flux lines are repelled from the sample (*B* is negative) and in a paramagnetic sample the magnetic flux lines are attracted to the sample (*B* is positive).

If we know the magnetic moment per unit volume of the sample, *I*, then *B* can be calculated using Eqn. 1. 1.

$$B = H + 4\pi I$$

Eqn. 1. 1

The magnetic susceptibility, κ, can be calculated from Eqn. 1. 2.

$$\kappa = \frac{I}{H}$$

Eqn. 1. 2

The molar susceptibility, χ, can then be calculated using Eqn. 1. 3, where *F* is the formula weight and *d* is the materials density.[1]

$$\chi = \kappa \frac{F}{d}$$

Eqn. 1. 3

1.3.1.3 Temperature dependence of magnetic properties

Diamagnetic materials are not subject to thermal disorder, so there is no variation of χ with temperature. Paramagnetic materials however, do show a variation in χ with *T* as its positive interaction is due the alignment of unpaired electron spins with *H*. As temperature increases, ordering of the electron spins becomes less significant due to thermal disorder. Paramagnetic materials tend to follow the Curie law with changing temperature, Eqn. 1. 4, where *C* is the Curie constant of the material and *T* is temperature.

$$\chi = \frac{C}{T}$$

Eqn. 1. 4

However, the Curie-Weiss law provides a better fit for the magnetic data, as this takes into account the Weiss constant, θ, shown by Eqn. 1. 5.

$$\chi = \frac{C}{(T + \theta)}$$

Eqn. 1. 5

A plot of χ vs. *T*, shows the temperature dependence for paramagnetic, ferromagnetic and antiferromagnetic materials (Fig. 1. 37). These can also be shown as plots of χ^{-1} vs. *T* (Fig. 1. 38). The relationship between χ and μ is shown by Eqn. 1. 6.

$$\chi = N\,\beta^2\,\frac{\mu^2}{3\,k\,T}$$

Eqn. 1. 6

Where *N* is Avogadro's number, β is the Bohr magneton and *k* is the Boltzmann constant. This can be simplified and expressed in terms of the magnetic moment, μ, which is directly related to the number of unpaired electrons present in a material, Eqn. 1. 7.[1]

$$\mu = 2.83\,\sqrt{\chi\,T}$$

Eqn. 1. 7

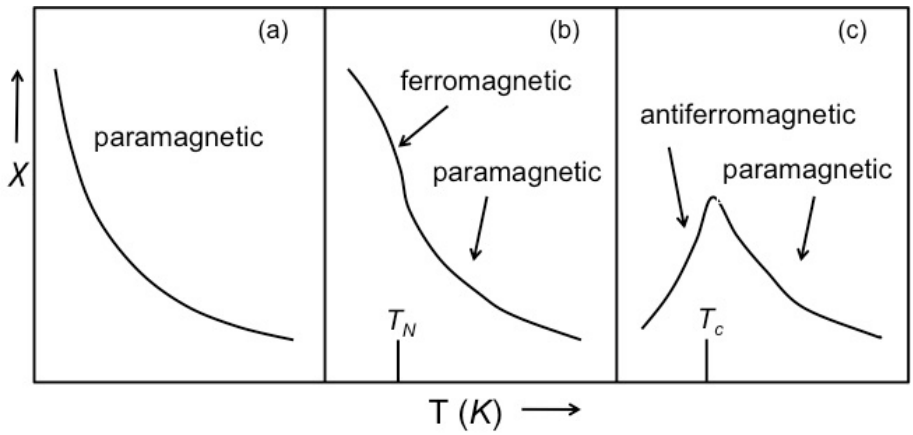

Fig. 1. 37: Plots of temperature dependence of χ for (a) paramagnetic (b) ferromagnetic and (c) antiferromagnetic materials.[1]

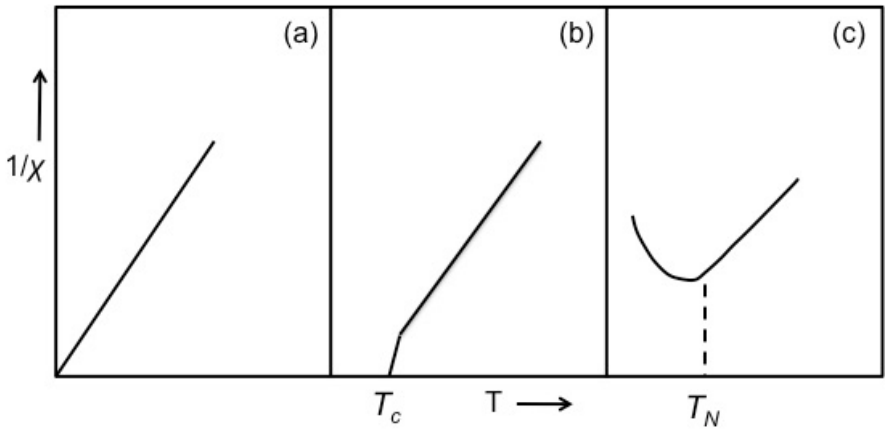

Fig. 1. 38: Plots of temperature dependence of χ^{-1} for (a) paramagnetic (b) ferromagnetic and (c) antiferromagnetic materials. Paramagnetic materials show Curie behaviour, and (anti-)ferromagnetic materials show Curie-Weiss behaviour above their Curie/Neel points.[1]

1.3.1.4 Magnetic frustration

Magnetic frustration occurs when the localized magnetic moments of an array of atoms, which interact through competing exchange interactions, cannot be simultaneously satisfied. This concept is well described by the Ising model of geometric frustration, where the antiferromagnetic interactions, which require neighbouring spins to point up or down on the vertices of an equilateral triangle cannot be simultaneously satisfied (Fig. 1. 39). A large degeneracy of the ground state can be caused by this frustration. When these triangles connect to form a lattice, there are different effects on the degeneracy depending on how they connect. If they connect along the edges to form a triangular lattice, the ground state degeneracy scales in proportion to the number of sites in the lattice. If they connect on the vertices to form a kagome lattice, the degeneracy will be large, regardless of the number of sites in the lattice and degrees of freedom of the magnetic moments. This degeneracy can lead to liquid-like magnetic states of matter; spin liquids, which show no sign of long-range magnetic order, even at zero K.[42] Frustrated magnetic materials include the anhydrous alums, spinels, jarosites, pyrochlores and garnets, among other structure types. However, the two-dimensional $S = ½$ kagome systems are highly sought, as these lattices

exhibit a high degree of magnetic frustration and are, therefore, ideal candidates for the formation of quantum spin-liquid ($S = ½$) states.[43]

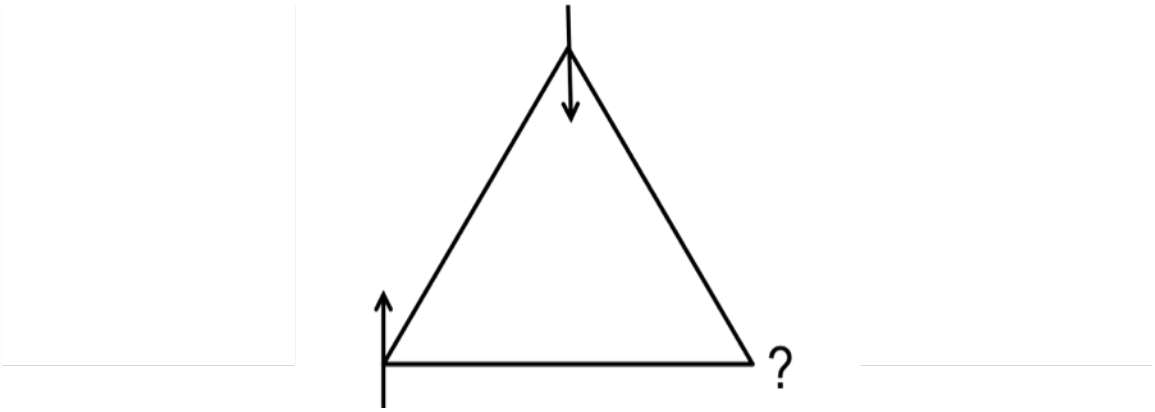

Fig. 1. 39: Triangular lattice showing one up-spin and one down-spin, leaving the third 'frustrated' as it is unable to align with the other two.[43]

1.4 References

1. A. R. West, *Basic Solid State Chemistry*, John Wiley & Sons, Chichester, 1991.
2. A. R. West, *Solid State Chemistry and its Applications*, John Wiley & Sons, Singapore, 2005.
3. G. Ferey, *J. Solid State Chem.*, 2000, **152**, 37.
4. P. S. Halaysamani and K. R. Poeppelmeier, *Chem. Mater.*, 1998, **10**, 2753.
5. M. Demartin Maeder, D. Damjanovic and N. Setter, *J. Electroceramics*, 2004, **13**, 385-392.
6. M. Leblanc, V. Maisonneuve and A. Tressaud, *Chem. Rev.*, 2015, **115**, 1191-1254.
7. C. Sabelli, *Neues Jahrbuch fuer Mineralogie.*, 1987, **10**, 481-487.
8. H. N. Bordallo, X. Wang, K. M. Hanif, G. F. Strouse, R. J. M. da Fonseca, L. P. Sosman and A. j. Dias Tavares, *J. Phys.: Condensed Matter*, 2002, **14**, 12383-12389.
9. P. Koehl, U. Mueller and D. Reinen, *Z. Anorg. Allg. Chem.*, 1972, **392**, 124-136.
10. A. A. Udovenko, N. M. Laptash and I. G. Maslenikova, *J. Fluorine Chem.*, 2003, **124**, 5-15.
11. A. K. Tyagi, R. Poettgen and J. Koehler, *Z. Anorg. Allg. Chem.*, 1996, **622**, 1329-1334.
12. G. F. Schaefer, *Z. Kristallogr., Kristallgeom., Kristallphys., Kristallchem.*, 1986, **144**.
13. K. M. Ok, E. O. Chi and P. S. Halasyamani, *Chem. Soc. Rev.*, 2006, **35**, 710.
14. M. Gerken, D. A. Dixon and G. J. D. Schrobilgen, *Inorg. Chem.*, 2000, **39**, 4244 4255.
15. L. Q. Tang, M. S. Dadachov and X. D. Zou, *Z. Krystallogr. NCS.*, 2001, **216**, 259.
16. P. A. Maggard, T. S. Nault, C. L. Stern and K. R. Poeppelmeier, *J. Solid State Chem.*, 2003, **175**, 27.
17. R. M. Herak, S. S. Malcic and L. M. Manojlovic, *Acta Cryst.*, 1965, **18**, 520

18. M. HIlbers, M. Leimkuhler and R. Mattes, *Z. Natur.., B: Chem. Sci.*, 1989, **44**, 383-388.
19. C. Peiyun, L. Tsaiwei, D. Jianhung, C. Borchen and L. Kwanghwa, *Inorg. Chem.*, 2007, **46**, 3619 3622.
20. M. A. Hitchman, Y. V. Yablokov, V. E. Petrashen, M. A. Augustyniak-Jublokov, H. Stratemeier and M. J. Riley, *Inorg. Chem.*, 2002 **41**, 229 238.
21. F. Moewius, B. Ziemer, G. Reck, M. Meisel and H. Grunze, *Z. Anorg. Allg. Chem.*, 1987, **82**, 547.
22. M. Jinxiao, W. Chengxin, C. Ning, L. Rong and P. Yuanming, *J. Solid State Chem.*, 2010, **183**, 2763 2769
23. C. R. Ross, B. L. Paulsen, R. M. Nielson and S. C. Abrahams, *Acta. Cryst.*, 1998, **B54**, 417.
24. H. Shorafa and K. Seppelt, *Inorg. Chem.*, 2006, **45**, 7929.
25. M. P. Crosnier-Lopez, H. Duroy and J. L. Fourquet, *Z. Anorg. Allg. Chem.*, 1993, **619**, 1597-1602.
26. A. Michailovski, A. Rueegg, D. Sheptyakov and G. R. Patzke, *Inorg. Chem. Comm.*, 2006, **45**, 5641-5652.
27. A. Alberti and G. Vezzalini, *Acta Cryst. B*, 1981, **37**, 781-788.
28. I. M. Shlyapnikov, E. A. Goreshnik and Z. Mazej, *Chem. Comm.*, 2013, **49**, 2703-2705.
29. J. Patarin, F. Marcuccilli-Hofner and H. Kessler, *Eur. J. Solid State Chem.*, 1994, **31**, 501.
30. V. Y. Kavun, B. V. Bukvetskii, N. M. Laptash, I. G. Maslenikova and S. S. Sergienko, *Z. Strukt. Khimii*, 2001, **42**, 921-927.
31. D. W. Aldous and P. Lightfoot, *Solid State Sci.*, 2009, **11**, 315-319.
32. R. Stromberg, *Acta. Chem. Scand. Ser A* 1986, **40**, 325.
33. J. Supel, R. Marx and K. Seppelt, *Z. Anorg. Allg. Chem.*, 2005, **631**, 2979-2986.
34. O. Kraemer and B. G. Mueller, *Z. Anorg. Allg. Chem.*, 1995, **621**, 1969 1972.
35. P. Benkic, Z. Mazej and B. Zemva, *Ange. Chem. International Ed.*, 2002, **41**, 1398 1399.

36. K. S. Woo, C. H. Young and P. S. Halasyamani, *J. Am. Chem. Soc.*, 2010, **132**, 17684-17685.
37. P. R. Sabatier, G. Charroin, D. Avignant and J. C. Cousseins, *Acta. Cryst.*, 1979, **B35**, 1333.
38. M. P. Shores, E. A. Nytko, B. M. Bartlett and D. G. Nocera, *J. Am. Chem. Soc.*, 2005, **127**, 13462-13463.
39. S. A. Reisinger, C. C. Tang, S. P. Thompson, F. D. Morrison and P. Lightfoot, *Chem. Mater.*, 2011, **23**, 4234-4240.
40. S. Menchetti and C. Sabelli, *Neues Jahr. Mineral. Monat.*, 1976, **406**, 417.
41. P. W. Atkins, *Physical Chemistry*, 9th Edition edn., Oxford University Press, Oxford, 2009.
42. L. Balents, *Nature*, 2010, **464**, 199 - 208.
43. A. Harrison, *J. Phys.: Condens. Matter*, 2004, **16**, 553-572.

2.0 Techniques

2.1 Synthetic methods

The hydrothermal method was developed as a way of imitating natural mineral formation processes on a much shorter timescale.[1] It was used in 1892 in a commercial process of obtaining pure aluminium hydroxide by using sodium hydroxide to leach bauxite.[2] It was used before this, in 1845, by Schafthaul to synthesise quartz, a process which is currently used to produce quartz for electronics. But it was not until much later in 1948 that Barrer used the process to produce synthetic analogues of zeolites, which threw the doors wide open on a new method of materials synthesis which has proved very popular among materials scientists.[3]

A hydrothermal reaction could best be described as a "reaction occurring under conditions of high temperature and pressure in the presence of an aqueous solvent in a closed system".[1] A solvothermal reaction is effectively the same with the exception that the solvent is not always aqueous. Ionothermal synthesis has a similar definition except that molten salts (ionic liquids) are used in place of conventional solvents. All reactions carried out during the course of this work at temperatures above 100 ^{o}C were done in a Teflon lined steel autoclave and meet the definition of hydrothermal, solvothermal or ionothermal (depending on the solvent used). Reactions carried out below 100 ^{o}C were done in a polypropylene bottle and would be better described as an aqueous reaction.

2.1.1 Ionic liquids in synthesis

Ionic liquids (ILs) have received much attention[4-6] over recent years due to their potential of replacing traditional organic solvents in homogenous catalysis. ILs can be described as "any material in the liquid state that consists predominantly of ionic species".[4] They have been utilised as electrolytes in batteries and fuel cells and electrodeposition solvents as well as in the synthesis of zeolites and metal MOFs.[7]

In the synthesis of MOFs and zeolites the ILs act as an inert solvent but, in some cases, can also act as the structure directing agent. It is also possible, with some care, to recycle and reuse the ionic liquid once the reaction has been completed and the product is filtered. These properties make ionic liquids highly desirable and very useful reagents in ionothermal synthesis.

Ionothermal synthesis offers several advantages over conventional hydrothermal/solvothermal synthesis. In some cases it gives more control over the oxidation state of the product, making it an ideal choice for experiments where a specific oxidation state is required that can't be easily achieved using conventional solvents.[8] This is exceptionally useful when the desired outcome also must have a high dimensionality, which generally requires higher temperatures to achieve. Under normal hydrothermal or solvothermal conditions, the products will condense into higher dimensionality structures, but will often undergo over-reduction of the oxidation state. Ionic liquids have been shown to give better control over the oxidation state while increasing the dimensionality of the structures at higher reaction temperatures when compared to traditional solvents.[8]

2. 2 Diffraction Methods

X-rays are generated when electrons, accelerated by a high voltage, collide with a metal target and are decelerated. Through several collisions their energy is released as a continuous X-ray spectrum known as white radiation (Fig. 2. 1).[9, 10] If an electron has sufficient energy it will ionise the target by ejecting an electron from an inner shell, an electron from a higher shell will then be transferred to fill the vacancy. This process causes the emission of X-ray radiation with a characteristic wavelength of the energy gap between the two shells. Depending on the adjacency of the shell that the electron is transferred from to fill the vacancy, different wavelengths can be obtained. If the shell of the transferred electron is adjacent to the shell being filled ($2p$ to $1s$) then the wavelength is known as K_α, if it is non-adjacent ($3p$ to $1s$) then it is K_β which is shorter in wavelength and less common.[11] The K_α emission lines are really split into a doublet, $K_{\alpha 1}$ and $K_{\alpha 2}$, due to the spin states of the $2p$ electrons and the wavelength, in the absence of a monochromator, used is an average of the doublet. Different metal targets can be used to generate different X-ray wavelengths, and the doublets can be separated by passing the beam through a monochromator.[9] Both sealed tube and rotating anode X-ray generators are used in laboratory instruments. Rotating anode chambers can produce X-rays of much greater intensity as the metal source does not need to be cooled as it is rotated through the electron beam. When using a sealed tube X-ray source, the intensity of the beam generated is dependent on the cooling rate of the source. Typically X-rays for a copper source from a rotating anode are 3-5 times more intense than those from a sealed tube.

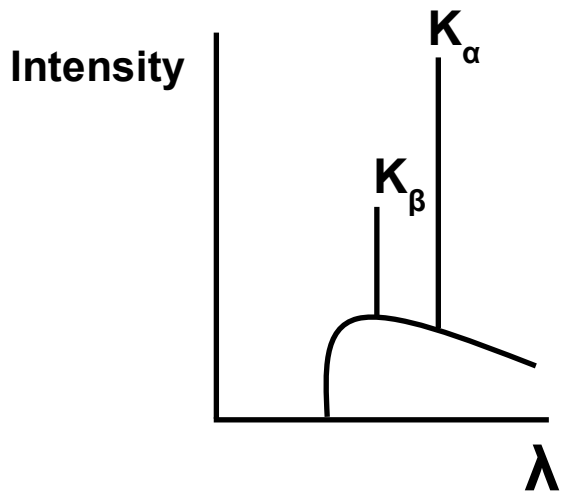

Fig. 2. 1: A typical X-ray emission spectrum of a metal.

In 1912 Max von Laue noticed that the distances between atoms were similar to the wavelengths of X-rays, and therefore X-rays should be diffracted by crystalline structures. The long-range ordering present in crystalline materials means that when X-rays are diffracted they should appear as a regular pattern, and as a result of constructive interference this patterns appears as an array of spots. Crystals can be thought of as being built up of layers or planes which act as semi-transparent mirrors. Some X-rays will be reflected off a plane with an angle of reflection equal to the angle of incidence; the rest will pass through and be reflected by subsequent layers (Fig. 2. 2). Beams 1 and 2 are reflected by adjacent planes, A and B respectively, and when the reflected beams 1' and 2' are in phase then constructive interference occurs. For both beams to be in phase, beam 2-2' has to travel an extra distance *xyz* which must be equal to an integer number of wavelengths. The distance between A and B, known as the *d*-spacing, is related to the angle of incidence, θ (the Bragg angle), and the distance *xy* by Bragg's law (Eqn. 2. 1).

$$xy = yz = d\sin\theta$$

$$xyz = 2d\ sin\ \theta$$

$$xyz = n\lambda$$

$$n\lambda = 2d\ sin\ \theta$$

Eqn. 2. 1

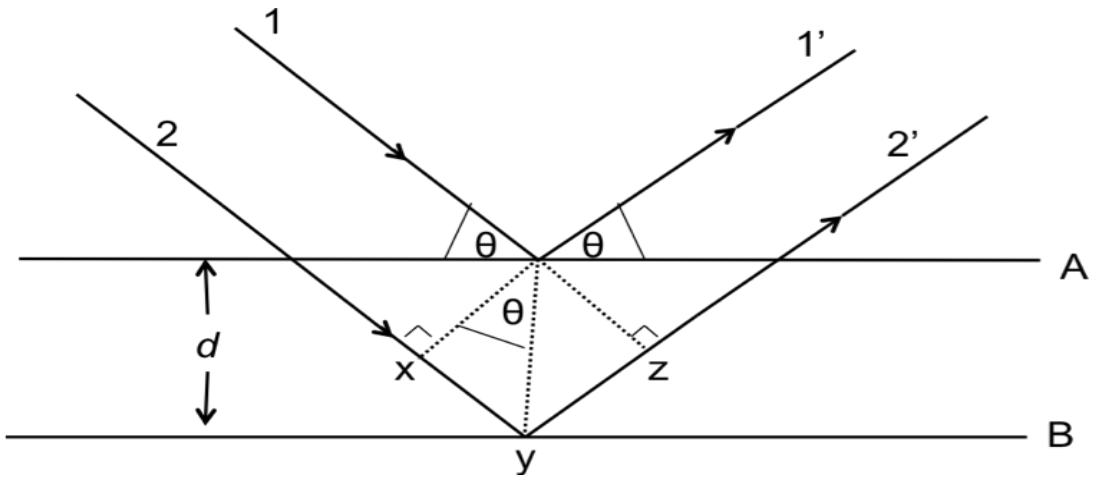

Fig. 2. 2: Incident X-ray beams 1 and 2 reflected by adjacent planes A and B.

The distance between planes, *d*, can be written as d_{hkl}, and, for a known value of *hkl*, sin θ can be calculated. This is seen most simply in a cubic crystal system where all unit cell axes are of equal length (Eqn 2. 2).

$$\sin\theta = (h^2 + k^2 + l^2)^{1/2}\frac{\lambda}{2a}$$

Eqn. 2. 2

Where *h*, *k*, and *l* are indices that equate to planes, Miller planes, throughout the crystal structures that have a given orientation orthogonal to *a*, *b*, or *c*. For example the Miller plane 100 will have an orientation orthogonal to *a* while 010 will have a direction orthogonal to *b*. When a crystal diffracts a beam of X-rays they are scattered by the electrons of the atoms contained therein. The degree of scattering is dependent on the atomic number (*Z*) of the atom, greater atomic number gives greater scattering power, this is known as the scattering factor or the form factor, which is dependent on the incident angle of radiation, θ. The higher the incident angle the weaker the intensity of diffracted X-rays. Therefore a diffraction pattern is a pattern of electron density within a crystal as well as a pattern of atomic geometry. These patterns can be obtained from the structure factor, *F*, which is a mathematical description of how a material scatters incident

radiation. This map of electron density, along with the Bragg equation is what allows the determination of the structure of crystalline materials through the method of single crystal X-ray diffraction.

2.2.1 Single crystal diffraction

Single crystal diffraction experiments provide unique intensities, I_{hkl} which correspond accordingly to scattering from each Miller plane in the structure. These intensities are proportionally related to the modulus of the structure factor, F_{hkl}, squared (Eqn. 2. 3).

$$I_{hkl} \propto |F_{hkl}|^2$$

Eqn. 2. 3

A Rigaku SCX mini desktop diffractometer and a Rigaku Mercury CCD diffractometer, both in house facilities, were used to collect data for this work. Both of these machines are equipped with graphite monochromated Mo K_α radiation, and area detectors to speed up data collection times through collection of multiple diffraction intensities in a single image scan. The mini diffractometer collects all images twice to help minimise any spurious reflections, improving data quality. Initially, six image frames are collected to screen the crystal and check its diffraction quality and intensity and calculate approximate unit cell parameters. This is done to ensure the crystal is correctly oriented in the beam, and that the scan time is adequate to produce intense spots before the full data collection process begins. Once a full set of data has been collected it is integrated into a 3D model of related spots. Once the related spots are integrated they can be described as reflections, with *hkl* values assigned to each set of relatedcspots in the pattern. Systematic absences can be determined from these values and a space group can be assigned to the crystal structure. A 3D map of electron density (atom type and position) can be obtained from the diffraction data through a series of complex calculations which overcome the loss of phase information that occurs during

the physical measurement process, known as the phase problem. The structure factor, F_{hkl}, can then be used to Fourier synthesise a map of electron density, ρ_{xyz} (Eqn. 2. 4).

$$\rho_{xyz} = \frac{1}{V} \sum_{hkl} F_{hkl} \; e^{-2\pi i(hx+ky+lz)}$$

Eqn. 2. 4

2.2.1.1 Structure solution

Most modern structure solution software programs, such as WinGX[12], make use of direct methods in order to determine the crystal structure from the structure factors. This method works well for structures with like atoms, but if some heavy atoms are present then Patterson synthesis is often a better option. Patterson synthesis uses the amplitude of the square of the structure factor taken from the diffraction data to create a map of vectors between atoms in the unit cell (Eqn. 2. 5).

$$P_{uvw} = \frac{1}{V} \sum_{hkl} |F_{hkl}|^2 \; exp^{-2\pi i(hx+ky+lz)}$$

Eqn. 2. 5

2.2.1.2 Structure refinement

Once an initial map of electron density has been generated then the structure may be refined. The most commonly used method of structure refinement is least-squares. This method compares observed and calculated intensities, giving a difference value. An *R*, reliability, factor is used to measure the progress of the refinement, relative to the structure factor and the square of the structure factor, with values below 0.05 indicating a successful refinement. The SHELXL-97[13] structure refinement program gives the weighting scheme as;

$$w = \frac{1}{\delta^2 (F_o^2) + (aP)^2 + bP'}$$

Eqn. 2. 6

Where P is a summation used to reduce bias, and a and b are adjustable parameters, employed to keep the goodness of fit close to 1.0, provided that the model used is adequate.

The R-factor for F^2 is given by;

$$wR_2 = \left(\frac{\sum[w(F_o^2 - F_c^2)]^2}{\sum w[F_o^2]^2}\right)^{\frac{1}{2}}$$

Eqn. 2. 7

And the R-factor for F is given by;

$$wR_1 = \frac{\sum[w(|F_o| - |F_c|)]^2}{\sum w|F_o|^2}$$

Eqn. 2. 8

The goodness of fit is based on F^2 and is shown as;

$$GOF = S = \left\{\frac{\sum[w(F_o^2 - F_c^2)]^2}{n - p}\right\}^{\frac{1}{2}}$$

Eqn. 2. 9

Where n is the number of reflections and p is the number of refined parameters. Values of wR_2 are typically between two and three times the values of wR_1, if the values deviate from this then it indicates there may be a problem with the refinement. Common errors can be space group choice during the refinement process, or non-standard settings. However, selecting the incorrect crystal system during the integration process usually causes the wR_2 values to deviate, and thus

the data must be re-integrated. When the correct weighting schemes are used then this can significantly improve the refinement by scaling all reflections appropriately and thus lowering the wR_1 and wR_2 values.

2.2.2 Powder X-ray diffraction

Powder diffraction, unlike single crystal diffraction, does not routinely allow for the determination, solution and refinement of a structure. This is because all symmetry equivalent reflections, and many non-equivalent ones, may have the same *d*-spacing, due to the compression of 3D data to 1D data, so individual reflections can't be measured. Powder diffraction was carried out to determine sample purity by comparison with simulated patterns from single crystal data. Patterns were also compared to known materials to determine if they were new, and to minimize submission of identical samples for single crystal X-ray diffraction. PXRD patterns were collected on a Panalytical XPert powder diffractometer using a copper anode which produced monochromated K_{a1} X-rays at 1.5406 Å.

2.2.3 Neutron diffraction

Neutron diffraction experiments were carried out at the ISIS neutron facility, Rutherford Appleton Laboratories in Harwell. This facility provides a pulsed spallation source of neutrons by accelerating protons into a heavy metal target. Neutrons provide a different source of radiation than X-rays that can be used to analyse different properties of materials, such as magnetism. The scattering power of neutrons is dependent on the atomic nuclei rather than on the electrons, as in X-ray scattering.[14] As such, light atoms can be observed more precisely in the presence of heavy atoms. Neutrons also have a non-zero spin ($S = ½$) so will be scattered by unpaired electrons as well as atomic nuclei, so magnetic structures can be explored using this technique. One drawback is that much larger samples are required for neutron experiments when compared with X-rays, due to

neutron sources having a relatively low intensity.

The detector is set at a fixed scattering angle 2θ and the time taken for the neutrons to reach the detector can be measured by the time-of-flight method (Fig. 2. 3). The scattered intensity is measured as a function of wavelength or d-spacing.

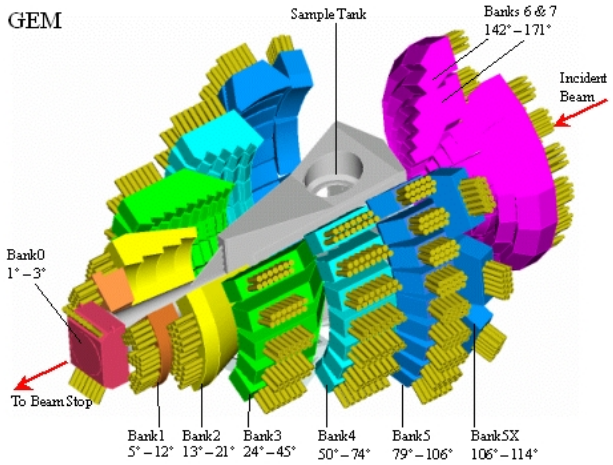

Fig. 2. 3: Schematic diagram of the GEM instrument detectors at the ISIS neutron facility.[15]

The wavelength of neutrons can be determined from the de Broglie equation (Eqn 2. 10);

$$\lambda = \frac{h}{mv}$$

Eqn. 2. 10

And the kinetic energy is given as (Eqn. 2. 11);

$$\frac{1}{2}mv^2 = \frac{3}{2}kT$$

Eqn. 2. 11

where m is the mass of the neutron. All wavelengths are used in a *TOF* experiment with a diffraction pattern collected for every pulse of neutrons. The flight path of a neutron, L, and the TOF, t, is related to the d-spacing by De Broglie's equation

substituting wavelength from Bragg's law (Eqn 2. 12 & Eqn 2. 13)

$$V = \frac{L}{t}$$

Eqn. 2. 12

$$t_{hkl} = \left(\frac{2mL\ sin\theta}{h}\right) d_{hkl}$$

Eqn. 2. 13

The time taken for a neutron to reach the detector, *t*, is proportional to the d-spacing of diffraction planes. Larger values of 2θ and longer path lengths, *L*, can increase the resolution of the diffraction pattern collected.

2.4 Magnetic measurements

Neutron diffraction can be used to determine the magnetic properties of a sample *via* the evolution of magnetic Bragg peaks with decreasing temperature. While magnetometers are the best choice for measuring a samples magnetic behaviour, neutron diffraction can be used to complement this technique and both data sets can be used to provide a very detailed magnetic description of a structure.[10] Magnetic measurements for this project were carried out in two different institutes, The University of Edinburgh and Moscow State University. Measurements carried out in Edinburgh were performed on a Quantum Design MPMS SQUID magnetometer, while measurements carried out in Moscow were done on a Vibrating Sample Magnetometer (VSM).

2.4.1 Superconducting quantum interference device (SQUID)

When a sample is moved through a coil of wire a flow of electrons is induced. It is this principle that is used to measure magnetisation in a SQUID device. A magnetic field is applied parallel to the sample which is moved in small increments through the field.[10, 11] The coil of wire, Josephson junction, surrounding the sample (Fig. 2. 4) has a current flow that changes as the sample passes through. The SQUID detects the change in current flow, and the samples magnetisation can be calculated.

A VSM does not utilise a Josephson junction, but instead rapidly vibrates the sample through a uniform magnetic field in a direction orthogonal to pickup coils. These coils detect changes in the magnetic field as the sample is rapidly vibrated.

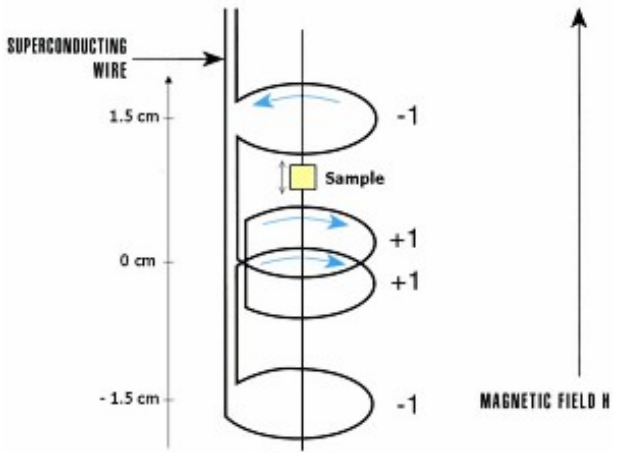

Fig. 2. 4: Schematic diagram of a SQUID magnetometer

2.5 The Rietveld method

The Rietveld method was developed by Hugo M. Rietveld in 1969 to aid crystallographers in the extraction of information from powder diffraction patterns. Single crystal diffraction will always yield the most information on a structure when compared to powder diffraction and as such will always be preferential to powder methods.[16] However it is not always possible to grow a single crystal of sufficient quality to perform a single crystal diffraction experiment, so powder diffraction must be utilised. The Rietveld method[16] utilises structure refinement similar to that of a single crystal refinement, except that intensities are used instead of structure factor, to fit the intensity of a known structure to the intensity of an estimated structure. The cell parameters, atomic coordinates, thermal parameters and several other variables can all be modelled and refined using software such as GSAS[17] and EXPGUI.[18]

2.5.1 Representational analysis

Modelling magnetic structures obtained from neutron diffraction data is often carried out in a systematic 'trial and error' manner, which can be incredibly time consuming, particularly if the structure has multiple magnetic atoms with different alignments. Representational analysis uses matrix calculations to provide symmetry-allowed model magnetic structures that can be integrated with programs like GSAS and refined against diffraction data.[19] The simulated annealing representational analysis, SARA*h,* program by Andrews Wills was used in conjunction with GSAS to fit a magnetic model to neutron diffraction data. The program requires a space group, which is non-magnetic, and a propagation, *k*, vector to supply the user with a number of trial structures that can be fitted to the diffraction data.[20] This process saves a lot of time, as without knowledge of the exact exchange interactions occurring within the magnetic structure it is very difficult to choose the correct moments to refine.

2.6 Bond valence sum calculations

Bond valence sum calculations were carried out once a single crystal structure refinement was complete. This helped determine if the final structure obtained was correct by determining the formal oxidation state, and also showed if there was any atomic disorder present. The bond valence, *S*, of each bond surrounding a metal centre are summed together with the total being close to the hypothesised valence state of the metal atom. The calculation for an individual bond valence is based on Eqn. 2. 14;

$$S = \exp\left(\frac{(R_o - R\,)}{B}\right)$$

Eqn. 2. 14

Where S is the bond valence, R is the bond length and R_o and B are bond valence parameters that depend on the two atoms forming the bond.[21] Bond valence sums were carried out using the VaList[22] program by Andrew Wills.

2.7 CHN microanalysis

CHN analysis was performed using a Carlo Flash 2000 Elemental Analyser and was collected by Stephen Boyer at the London Metropolitan University. Obtained values were compared to theoretical values and used as a measure of sample purity.

2.8 Experimental procedures

During the course of this work 1443 experiments were carried out using hydrothermal or ionothermal techniques, solid-state synthesis techniques were also carried out in two experiments. Hydrothermal experiments were undertaken in either Teflon-lined steel autoclaves or polypropylene bottles depending on reaction temperature. Once the vessel had cooled to room temperature the contents were filtered, washed with water and dried at 60 ^{o}C in air. Ionothermal experiments were done solely in autoclaves as temperatures were always above 100 ^{o}C. A general reaction scheme is as follows; a metal source along with a template (organic or inorganic) is added to a polypropylene bottle or autoclave, this mixture is then dissolved in HF along with a solvent (generally water and ethylene glycol or ionic liquid). The vessels were sealed and heated at an appropriate temperature (less than 100 ^{o}C for polypropylene bottles and between 100 ^{o}C and 220 ^{o}C for autoclaves) for up to a maximum of seven days.
HF is used as a fluorine source as well as acting as the mineralising agent.
Water and ethylene glycol were used as solvents as they are both cheap and readily accessible. Other solvents were tried for varying reasons such as DMSO in an attempt to increase sulphur content in the products or methanol and ethanol. In most cases, the same product was formed regardless of solvent choice.

Different metal sources were used in this work, all of which were able to adopt a d^1 or d^9 S = ½ configuration; titanium, vanadium, molybdenum, and copper.

Various templates were used, both organic and inorganic. Inorganic species used were alkali metals from Li^+ to Cs^+. These were chosen as counter cations and to view the size effect each one had on the resulting crystal structures. The organic templates are listed in (Fig. 2. 5). They were chosen to act as structure directing agents through their geometry (where the alkali metals act as structure directing agents through their atomic radii) as well as counter cations once they have been protonated.

Once metal sources, templates, solvents and temperatures are all combined a wide range of variables are generated. Initially reactions were carried out at 160 ^{o}C with varying solvent volumes, these were then characterised and the reaction was repeated at a different temperature. Through this method a plethora of reactions can be carried out and compared, indicating the effect of temperature and solvent concentration on the experimental outcome.

Solid-state reactions were carried out in evacuated quartz tubes and heated in either a box furnace or tube furnace. Since some of the reagents used in this work were air sensitive the initial procedure of weighing the starting materials was carried out in a glove box. Stoichiometric ratios of reactants were mixed in a mortar and pestle until homogenous. This mixture was left as loose powder and was then loaded into a quartz tube, which was then evacuated and subsequently sealed with a hot flame. These were then heated to temperatures above 300 ^{o}C for up to 14 days.

The ionic liquid, 1-ethyl-2-methylimidazolioum trifluoromethylsulfonyl imide (Fig. 2. 6), used in the synthesis was prepared via a two step process. 1-Methylimidazole is mixed with ethyl bromide in a round bottom flask under argon, placed on ice to keep the reaction cool as it is very exothermic. Once the heat has dissipated from the initial mixing the reaction is heated to 40 ^{o}C for 2-3 hours before being allowed to cool. The white crystalline substance, 1-ethyl-2-methylimidazolium bromide is recrystallised in water and resealed under argon. This is then ion exchanged to the desired final product by mixing it with Li^{+} bis-trifluoromethylsulfonyl imide. This is done by mixing both solids in water with the Li^{+} reagent in 10% excess and leaving to stir overnight. The oily hydrophobic liquid is separated and washed several times with water to remove any traces of bromide ions.

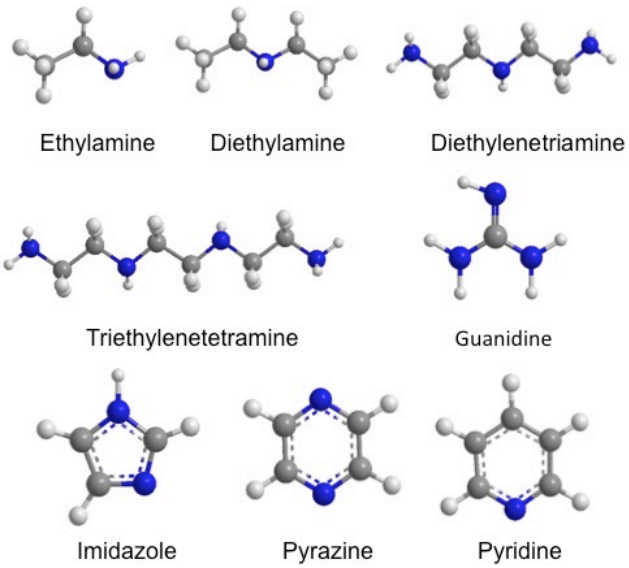

Fig. 2. 5: Organic templates used in the syntheses in this work.

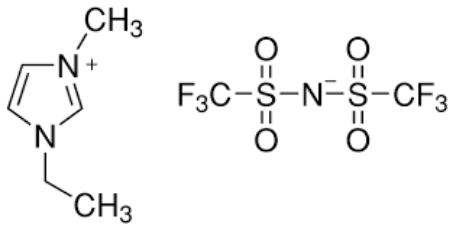

Fig. 2. 6: 1-ethyl-2-methylimidazolioum trifluoromethylsulfonyl imide

2.9 References

1. U. Schubert, *Synthesis of Inorganic Materials*, Wiley-VCH, U.S.A., 2002.
2. K. Bryappa and M. Yoshimura, *Handbook of Hydrothermal Technology*, Andrew Publishing, U.S.A., 2001.
3. R. A. Laudise, *Chemical and Engineering News*, 1987, **30**.
4. R. E. Morris, *Chem. Comm.*, 2009, 2990-2998.
5. D. Cole-Hamilton, *Science*, 2003, **299**, 1702-1706.
6. E. R. Parnham, E. A. Drylie, P. S. Wheatley, A. M. Z. Slawin and R. E. Morris, *Angew. Chem. Int. Ed.*, 2006, **45**, 4962-4966.
7. E. R. Cooper, C. D. Andrews, P. S. Wheatley, P. B. Webb, P. Wormald and R. E. Morris, *Nature*, 2004, **430**, 1012-1016.
8. F. H. Aidoudi, D. W. Aldous, R. J. Goff, A. M. Z. Slawin, J. P. Attfield, R. E. Morris and P. Lightfoot, *Nature Chem.*, 2011, **3**, 801-806.
9. A. R. West, *Basic Solid State Chemistry*, John Wiley & Sons, Chichester, 1991.
10. A. R. West, *Solid State Chemistry and its Applications*, John Wiley & Sons, Singapore, 2005.
11. P. W. Atkins, *Physical Chemistry*, Oxford University Press, Oxford, 9th Edition edn., 2009.
12. L. J. Farrugia, *J. Appl. Cryst.*, 2012, **45**, 849-854.
13. G. M. Sheldrick, *Acta. Cryst.*, 2008, **64**, 112-122.
14. T. Chatterji, *Neutron scattering from magnetic materials*, Elsevier Science, 2005.
15. http://www.isis.rl.ac.uk/Disordered/GEM/GEM_Home.htm).
16. R. A. Young and H. M. Rietveld, *The Rietveld Method*, Oxford University Press, U.S.A., 1993.
17. A. C. Larson and R. B. Von Dreele, *Los Almos National Laboratory Report*, 2000, 86-748.
18. B. H. Toby, *J. Appl. Cryst.*, 2001, **34**, 210-213.
19. A. S. Wills, *Physica B*, 2000, **276**, 680-681.
20. A. S. Wills, *Z Kristallogr Suppl*, 2009, **30**, 39-44.

21. N. E. Brese and M. O'Keeffe, *Acta. Cryst.*, 1991, **B47**, 192-197.
22. A. S. Wills, 2011.

3.0 Vanadium Oxyfluoride Chain and Ladder Materials

The crystal structures of six vanadium oxyfluoride and three vanadium fluorides will be discussed along with their hydrothermal chemistry and magnetic behaviour. These structures have been given the identifiers V-1 - V-9, numbered in the chronological order in which they were synthesised. V-3, V-5, V-6 and V-8 have been previously synthesised, but are included here for discussion and comparison with the new compounds.[1, 2] All compounds are magnetically active, with the ladders adopting a d^1 $S = ½$ configuration and the chains adopting a d^2 $S = 1$ configuration. The crystallographic information for these compounds is presented in Table 3. 1 , Table 3. 2 and Table 3. 3. Atomic coordinates are given in appendix A, and bond angles are contained in the appropriate CIF.

Single crystals were analysed using a Rigaku SCX-mini desktop diffractometer equipped with graphite monochromated Mo K_α ($\lambda = 0.71075$ Å) radiation. Intensity data were collected via the 'multi-scan' method to help improve data quality. Data were collected at 173 K. All structures were solved by direct methods and refined by full-matrix least-squares cycles in SHELXL-97.[3] All non-hydrogen atoms were modelled using anisotropic thermal parameters, unless circumstance dictated otherwise. Hydrogen atoms were, where possible, located using Fourier techniques and refined isotropically. Generally they were located at geometrically calculated positions and fixed to the atom in question to 'ride' with the refinement.

Powder diffraction experiments were carried out on a PANalytical Empyrean powder diffractometer equipped with monochromated Cu $K_{\alpha 1}$ ($\lambda = 1.5418$ Å) X-rays. The diffractometers were operated in reflection mode with data collected at room temperature.

Magnetic data were collected on an MPMS Quantum Design SQUID magnetometer (University of Edinburgh) or a Vibrating Sample Magnetometer (Moscow State University).

Of the nine crystal compounds presented in this chapter, four are previously known, $RbVOF_3$-*α*, $CsVOF_3$, NH_4VOF_3 and $[NH_4]_2VF_5$.[1, 2] These are compared both structurally and magnetically to the five new compounds synthesised.

Table 3. 1: Crystallographic information for V-1 through V-3

Compound	V-1	V-2	V-3
Formula	$KVOF_3$-α	$KVOF_3$-β	$RbVOF_3$-α
Space group	*C*2/*m*	*Pnma*	*Pbam*
a/Å	13.564(6)	7.176(7)	8.5656(10)
b/Å	7.595(3)	7.540(7)	11.5330(13)
c/Å	7.207(3)	13.1060(13)	3.865(4)
α/°	90	90	90
β/°	104.102(11)	90	90
γ/°	90	90	90
V/ Å^3	742.46(4)	709.13(6)	381.81(9)
Z	4	4	4
GFM	163.04	163.04	209.41
ρ_{calc} / g cm^{-3}	1.504	1.527	3.643
μ / mm^{-1}	1.909	1.939	15.177
Crystal size (mm)	0.25x0.18x0.07	0.34x0.03x0.03	0.41x0.38x0.27
F(000)	308	308	380
Reflections Collected	3666	5918	2160
Independent Reflections	881	700	406
R_{int}	0.0665	0.0449	0.0982
Data/Restraints/Parameters	811/0/61	659/0/61	368/0/37
GOF on F^2	1.281	1.067	1.201
R_1, wR_2 [$I > 2\theta(I)$]	0.0964, 0.2315	0.0266, 0.0805	0.0656, 0.1583
R_1, wR_2 (all data)	0.1038, 0.2366	0.0332, 0.1116	0.0712, 0.1651

Table 3. 2: Crystallographic information for V-4 through V-6

Compound	V-4	V-5	V-6
Formula	$RbVOF_3$-β	$CsVOF_3$	NH_4VOF_3
Space group	*Pbam*	*Pbam*	*Pbam*
a/Å	6.760(2)	8.944(5)	8.550(6)
b/Å	14.800(5)	11.323(3)	11.670(9)
c/Å	3.884(3)	3.873(9)	3.836(3)
α/°	90	90	90
β/°	90	90	90
γ/°	90	90	90
V/ Å^3	388.59(3)	393.68(6)	382.75(6)
Z	4	4	4
GFM	209.41	257.14	141.98
ρ_{calc} / g cm^{-3}	3.579	4.128	2.464
μ / mm^{-1}	14.913	18.675	2.518
Crystal size	0.22x0.20x0.13	0.16x0.15x0.12	0.18x0.03x0.03
F(000)	380	452	276
Reflections Collected	3482	2369	2204
Independent Reflections	416	465	407
R_{int}	0.1105	0.0748	0.0748
Data/Restraints/Parameters	367/0/37	390/0/37	390/0/37
GOF on F^2	1.075	1.183	1.128
R_1, wR_2 [$I > 2\theta(I)$]	0.0508, 0.1267	0.0375, 0.1152	0.0552, 0.1508
R_1, wR_2 (all data)	0.0592, 0.1342	0.0412, 0.1211	0.0566, 0.1526

Table 3. 3: Crystallographic information for V-7 through V-9

Compound	V-7	V-8	V-9
Formula	$[NH_4]_2VF_5$-β	$[NH_4]_2VF_5$-α	K_2VF_5
Space group	*Pmnb*	*Pnma*	*Pnma*
a/Å	7.523(7)	6.348(2)	7.371(3)
b/Å	5.717(5)	7.632(3)	5.664(2)
c/Å	12.143(1)	11.051(4)	11.540(3)
α/°	90	90	90
β/°	90	90	90
γ/°	90	90	90
V/ Å^3	522.26(4)	535.40(3)	481.79(2)
Z	4	4	4
GFM	177.99	177.99	224.14
ρ_{calc} / g cm^{-3}	2.315	2.258	3.090
μ / mm^{-1}	1.916	1.869	3.784
Crystal size	0.11x0.08x0.08	0.12x0.02x0.01	0.15x0.13x0.08
F(000)	360	360	424
Reflections Collected	638	4362	3961
Independent Reflections	286	527	490
R_{int}	0.0336	0.0904	0.1197
Data/Restraints/Parameters	267/0/46	478/0/43	402/0/46
GOF on F^2	1.073	1.362	1.058
R_1, wR_2 [$I > 2\theta(I)$]	0.0943, 0.2785	0.0883, 0.1811	0.0401, 0.1042
R_1, wR_2 (all data)	0.0991, 0.2850	0.0981, 0.1866	0.0529, 0.1132

3.1 Vanadium (IV) Oxyfluoride $S = ½$ Ladder Structures

This section will discuss the synthesis and characterisation of the structural and physical properties of three new vanadium (IV) oxyfluoride ladder structures, with comparisons to analogous compounds.

The aim was to synthesise new, magnetically active vanadium compounds with high dimensionality, using inorganic and organic cationic species to direct the structures.

3.1.1 Introduction

Vanadium compounds have a variety of scientifically interesting and technologically useful properties, particularly redox behaviour, which can lead to applications in Li^+ batteries and oxidation catalysis technologies, amongst other things.[4] This has led to a great deal of exploratory hydrothermal and solvothermal synthesis of vanadium containing systems, particularly vanadium oxides[5] and vanadium phosphates.[6] However, despite the large number of reported vanadium fluoride (VF) and oxyfluoride (VOF) compounds, the hydrothermal and solvothermal chemistry of these systems is still relatively unexplored, poorly understood and systematised. One of the main drives in this field is increasing the number of known VOF materials, using organic and inorganic cations as structure directing agents. This will aid in the understanding the parameters that control VOF formation, and eventually lead to the rational synthesis of functional VOFs, for example, for magnetic or optical purposes.[4] Examples of recently synthesised vanadium oxyfluoride compounds are presented in Table 3. 4 with their structural building unit and oxidation state.

Recently, attempts have been made to ionothermally synthesise VOF materials[7] due to evidence[8-11] that the ionic liquids can help promote the formation of higher dimensionality structures while simultaneously giving greater control over the oxidation state at higher temperatures, allowing the formation of more condensed structures with oxidation states giving $S = ½$ ground states. This idea,

combined with organic templates with three-fold symmetry have led to the discovery and characterisation of a new VOF kagome structure[7, 12] $[NH_4]_2[C_7H_{14}N][V_7O_6F_{18}]$ (DQ-VOF) (Fig. 3. 1 and Fig. 3. 2). The structure consists of a double layer V(IV) kagome bridged by V(III) through V – F – V bonds and disordered quinuclidine moieties spacing the layers (Fig. 3. 3). The V(IV) sites are comprised of VOF_5 octahedral units with short V – O vanadyl bonds exo to the layer, while the V(III) sites are entirely fluorinated. The V(IV) kagome layers are stacked in such a manner that they are offset by 60 ^{o} from each other (Fig. 3. 2).

Table 3. 4: Previously synthesised vanadium oxyfluoride compounds, their structural units and oxidation states.

Chemical formula	Structural unit	Oxidation state
Na_3VOF_5[13]	Monomer	IV
$[C_4N_3H_{16}][VOF_5].H_2O$[4]	Monomer	IV
$[C_6N_4H_{22}][VOF_4(H_2O)]_2.H_2O$[4]	Monomer	IV
Na_2VOF_5[14]	Monomer	V
$Cs_2VOF_4(H_2O)$[15]	*trans*-Monomer	IV
$[NH_4]_2[VO_2F_4]$[16]	*cis*-Monomer	V
$[C_{10}N_2H_{10}][V_2O_2F_6(H_2O)_2]$[4]	Dimer	IV
$[C_6N_2H_{14}][V_2O_2F_6(H_2O)_2]$[4]	Dimer	IV
$[C_6N_4H_{22}][V_2O_2F_8]$[4]	Dimer	IV
$Cs_3V_2O_2F_7$[17]	Face-shared dimer	IV
$[NH_4]_3[V_2O_4F_5]$[18]	Face-shared dimer	V
$[NMe_4]_2[V_2O_2F_6(H_2O)_2]$[19]	Edge-shared dimer	IV
$[NMe_4]Cs[V_2O_2F_8(H_2O)]$[20]	Corner-shared dimer	V
$K_2[NMe_4][V_2O_2F_9]$[20]	Corner-shared dimer	V
$Na[NMe_4]_2[V_3O_3F_{12}]$[20]	Corner-shared trimer	V
$Ba_3V_2O_4F_8$[21]	Corner-shared tetramer	V
$[C_6N_4H_{21}]_2[V_4O_4F_{14}].3H_2O$[4]	Tetramer	III/IV
$[C_6N_3H_{20}]_2[V_4O_4F_{14}].{}_2H_2O$[4]	Tetramer	III/IV
$Na_6[H_6V_{12}O_{30}F_2].22H_2O$[22]	Polyanionic	IV/V
$[C_6N_2H_{18}][V_{14}O_{36}F_4].4H_2O$[23]	Polyanionic	IV/V

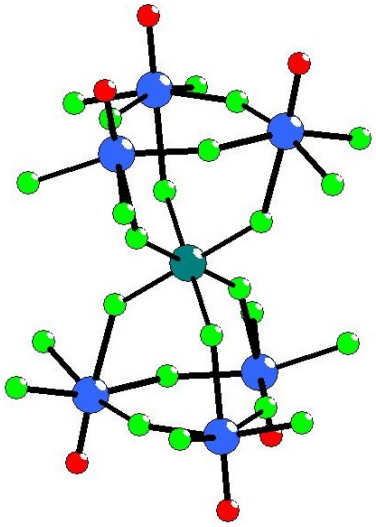

Fig. 3. 1: Building unit in DQ-VOF: double V(IV) (blue) kagome layers bridged by V(III) (dark green).

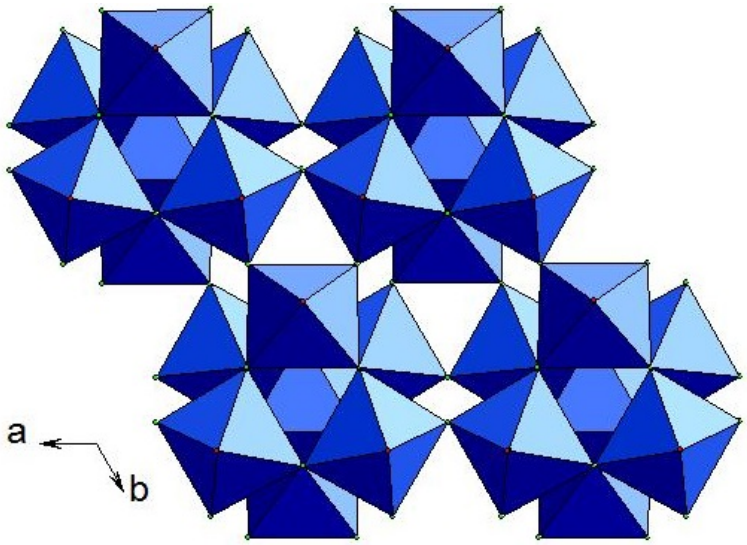

Fig. 3. 2: Polyhedral representation of the DQ-VOF kagome lattice, showing the 60 ° offset in the double layer when viewed along axis *c*.

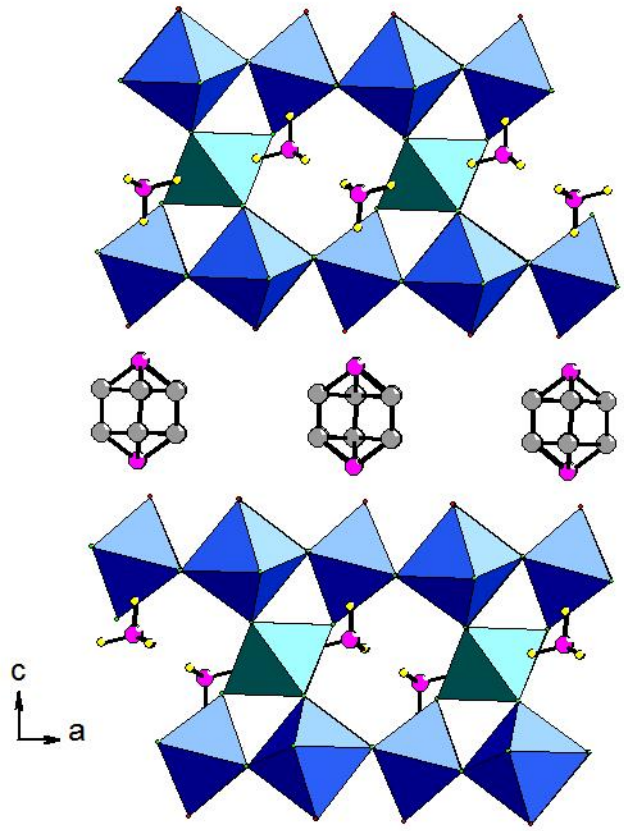

Fig. 3. 3: Full kagome bilayer with the inclusion of NH_4 groups and the disordered quinuclidine spacing the layers. The V (IV) units are blue, V (III) units are green, nitrogen is purple, carbon is grey and hydrogen is yellow.

3.1.2 Synthesis

Two distinct crystallographic phases of $KVOF_3$: α (V-1) & β (V-2) and $RbVOF_3$: α (V-3) & β (V-4) have been prepared solvothermally, along with $CsVOF_3$ (V-5) and NH_4VOF_3 (V-6). Attempts to synthesise polymorphs of the latter compounds were unsuccessful. These compounds display 1D arrays of ladders built from corner and edge-sharing vanadium oxyfluoride octahedral units (Fig. 3. 4 & Fig. 3. 5), charge balanced by the alkali metal and NH_4^+ cations.

Compounds V-1 through V-5 were prepared solvothermally, V-6 was prepared ionothermally. All reactions were in 40 mL Teflon lined steel autoclaves.

V-1, $KVOF_3$-α: V_2O_5 (1 mmol, 0.182 g) and K_2CO_3 (1 mmol, 0.136 g) were dissolved in 48% HF (31 mmol, 0.5 mL). A 7:1 ratio of water (1.75 mmol, 3.5 mL) and ethylene glycol (8 mmol, 0.5 mL) was added to the resultant mixture and allowed to settle before being sealed and heated for 72 hours at 100 ^oC. The resultant product consisted of blue block-like crystals indicating V(IV).

V-2, $KVOF_3$-β: V_2O_5 (1 mmol, 0.182 g) and K_2CO_3 (1.3 mmol, 0.180 g) were dissolved in 48% HF (31 mmol, 0.5 mL). A 7:1 ratio of water (1.75 mmol, 3.5 mL) and ethylene gylcol (8 mmol, 0.5 mL) was added to the solution which was sealed and heated at 160 ^oC for 24 hours. The resultant product consisted of blue needle-like crystals indicating V(IV).

V-3, $RbVOF_3$-α: $VOSO_4$ (dried) (3 mmol, 0.489 g) and RbF (2 mmol, 0.2089 g) were dissolved in 48% HF (31 mmol, 0.5 mL). A 1:1 ratio of water (1 mmol, 2 mL) and ethylene glycol (32 mmol, 2 mL) was added then sealed and heated at 100 ^oC for 72 hours. The resultant product consisted of blue block-like crystals indicating V(IV).

V-4, $RbVOF_3$-β: V_2O_5 (1 mmol, 0.182 g) and RbF (2 mmol, 0.2089 g) were dissolved in 48% HF (31 mmol, 0.5 mL). A 5:3 ratio of water (1.25 mmol, 2.5 mL) and ethylene glycol (24 mmol, 1.5 mL) was added, sealed, and heated at 160 ^oC for 24 hours. The resultant product consisted of blue block-like crystals indicating V(IV).

V-5, $CsVOF_3$: V_2O_5 (1 mmol, 0.182 g) and Cs_2CO_3 (0.51 mmol, 0.163 g) were dissolved in 48% HF (31 mmol, 0.5 mL). A 5:3 ratio of water (1.25 mmol, 2.5 mL) and ethylene glycol (24 mmol, 1.5 mL) was added, sealed, and heated at 160 ^oC for 24 hours. The resultant product consisted of blue block-like crystals indicating V(IV).

V-6, NH_4VOF_3: VOF_3 (1 mmol, 0.124 g) and guanidine carbonate (1 mmol, 0.091 g) were dissolved in 48% HF (6.2 mmol, 0.1 mL) and mixed in 1-ethyl-2-methylimidazolium trifluoromethylsulfonylimide (~3mmol, 1.5 g) before being sealed and heated for 48 hours at 160 ^oC. The resultant product consisted of blue needle-like crystals indicating V(IV).

V-1 to V-5 were filtered and washed in water, V-6 was washed with methanol to remove the ionic liquid from the sample. All crystals were of a green/blue colour indicating vanadium (IV), with block and needle-like morphologies. Samples were assessed for purity, initially, by eye, as it was obvious that the samples were not phase pure if there was the presence of black powder along with the blue-coloured crystals. Samples were separated using an optical microscope for diffraction experiments.

3.1.3 Structural characterisation

V-1 to V-6 are ladder-like structures formed from the same VOF_5 building unit (Fig. 3. 4). The ladder structure its self is comprised of corner and edge-sharing $[VOF_1F_{4/2}]$ octahedra linked through fluorine (Fig. 3. 5). The ladders are packed and 'surrounded' by the K^+ cations to form the complete 3D structure of $KVOF_3$ *β*, as viewed along the *b* axis (Fig. 3. 6).

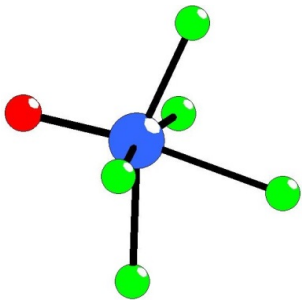

Fig. 3. 4: VOF_5 building unit.

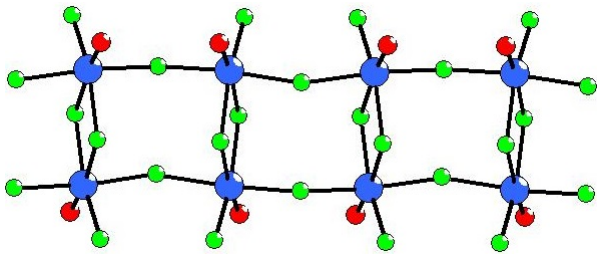

Fig. 3. 5: $VOF_1F_{4/2}$ ladder connected via fluorine

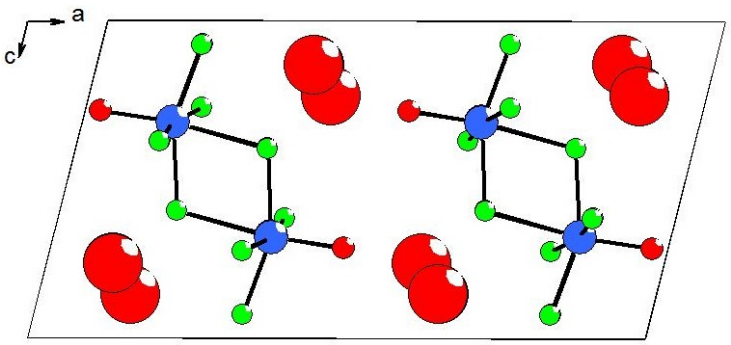

Fig. 3. 6: Packed ladders and counter cations forming the full 3D unit cell of $KVOF_3$-*α* viewed along the *b* axis.

The $KVOF_3$-α (V-1) system (synthesised at 100 °C) crystallises in the monoclinic $C2/m$ space group and displays near parallel packing of the vanadium oxyfluoride ladders (Fig. 3. 7). This is a marked difference from the $KVOF_3$-β (V-2) system (synthesised at 160 °C) which crystallises in the orthorhombic *Pnma* space group. This structure displays near perpendicular packing of the vanadium oxyfluoride ladders (Fig. 3. 8). Selected V – O and V – F bond lengths, along with bond valence sums for V-1 and V-2 are shown in Table 3. 5 and Table 3. 6 respectively.

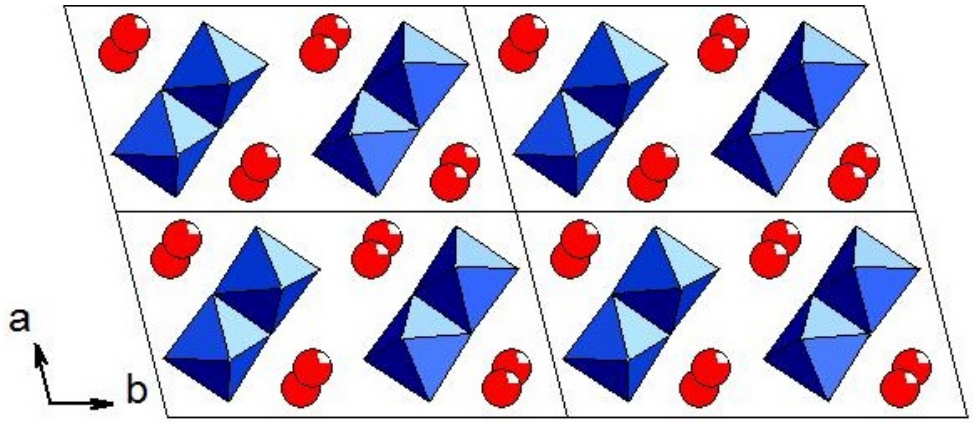

Fig. 3. 7: Extended packing of the structure showing 2x2 unit cells of $KVOF_3$-α displaying parallel packing of the ladder units viewed down the *b* axis. Ladders are shown in polyhedral representation.

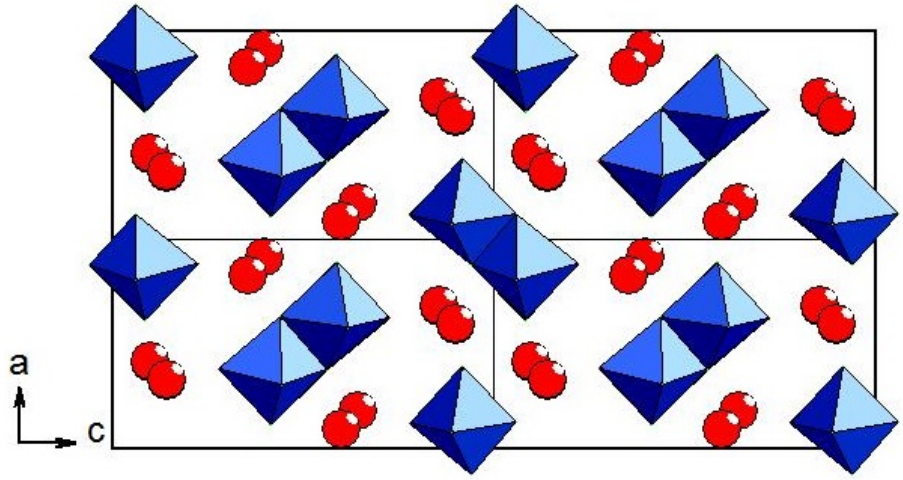

Fig. 3. 8: Extended packing of the structure showing the 2x2 unit cell of $KVOF_3$-β displaying near perpendicular packing of the ladder units viewed down the *b* axis

Table 3. 5 Selected bond lengths and bond valence sums for $KVOF_3$-α

Bond	Bond length (Å)	S_{ij}
V – O1	1.635(7)	1.496
V – F4	1.866(6)	0.638
V – F2	1.984(5)	0.464
V – F3	1.996(3)	0.449
V – F1	1.997(3)	0.448
V – F2	2.174(5)	0.278
		ΣV=3.773

Table 3. 6 selected bond lengths and bond valence sums for $KVOF_3$-β

Bond	Bond length ($\AA$)	S_{ij}
V – O1	1.606(3)	1.618
V – F3	1.871(3)	0.630
V – F4	1.970(3)	0.482
V – F1	1.973(2)	0.478
V – F2	1.991(2)	0.455
V – F4	2.172(3)	0.279
		ΣV=3.942

The packing angles of the ladders in V-1 and V-2 are near perpendicular and parallel respectively. This difference can be attributed to the temperatures at which each compound was synthesised. Various researchers, generally noting that higher temperatures tend to produce more condensed 3D structures and lower temperatures having lower dimensionality, have studied temperature effects on hydrothermal reactions.[24] While this is true for V-1, V = 742.46(4) $\AA^3$, and V-2, V = 709.13(6) $\AA^3$, the effect is limited to the condensation of the unit cell only, and

not to added dimensionality of the structure. The 8-coordinate K^+ cations in both structures remain unaffected by these changes in ladder packing. It is also interesting to note the completely different crystallographic space groups of V-1 and V-2. While the larger R_1 of V-1 may suggest that a different space group may indeed be required, a C centred monoclinic unit cell was the only symmetry allowed option for this compound based on its systematic absences. Several attempts at recollecting and reprocessing the data yielded the same space group, also evidenced by PXRD (Fig. 3. 9).

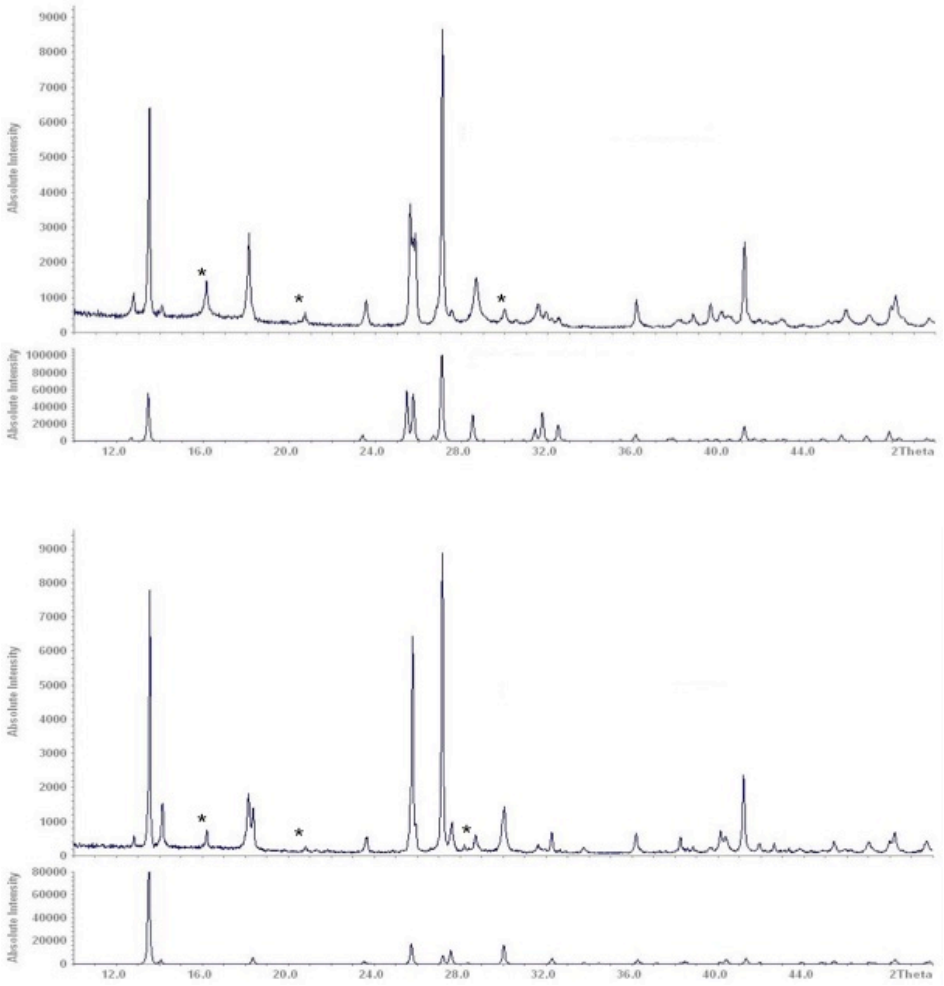

Fig. 3. 9: The PXRD patterns of $KVOF_3$-α (top) ($C2/m$) and $KVOF_3$-β (bottom) ($Pnma$). Experimental patterns are on top and calculated patterns from single crystal data are on the bottom of each. Teflon peaks are marked with an asterisk.

The $RbVOF_3$-α (V-3) (Fig. 3. 10) and $RbVOF_3$-β (V-4) (Fig. 3. 11) systems were synthesised at 100 ^oC and 160 ^oC respectively and display different polymorphic packing modes, similar to the packing differences in V-1 and V-2. Selected V – O and V – F bond lengths along with bond valence sums for V-3 and V-4 are shown in Table 3. 7 and Table 3. 8 respectively.

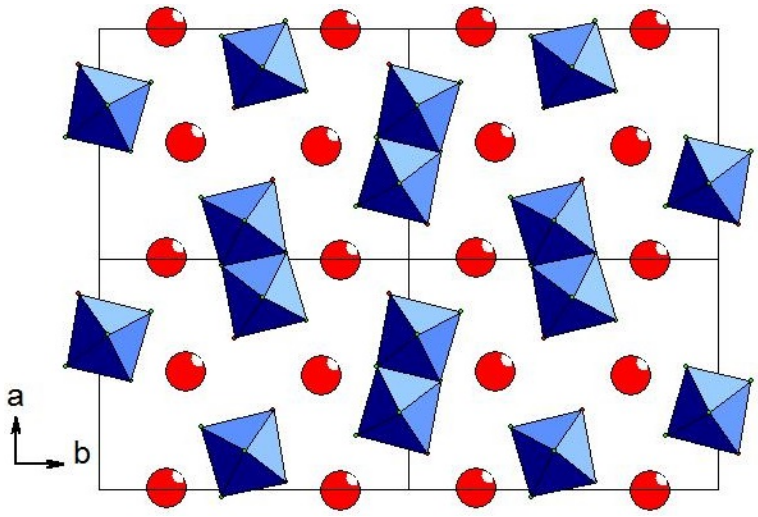

Fig. 3. 10: Extended packing of the structure depicting the 2x2 unit cell of $RbVOF_3$-α, showing a distortion of the parallel ladder packing that is seen in $KVOF_3$-α due to the size effect of Rb^+. The cell is viewed down axis *c*.

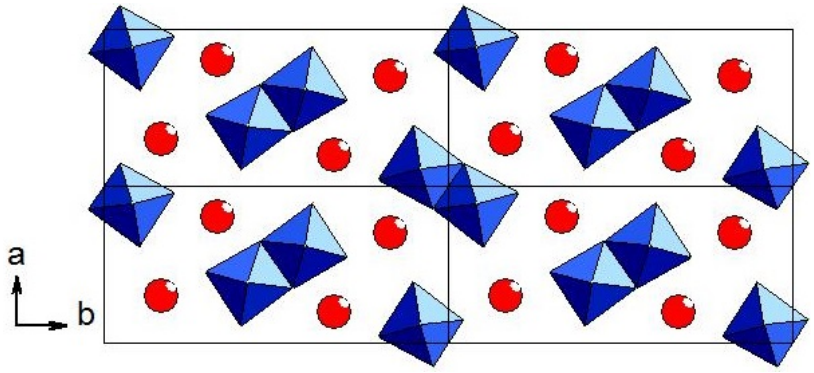

Fig. 3. 11: Extended packing of the structure depicting the 2x2 unit cell of $RbVOF_3$-β, showing a distortion of the near perpendicular ladder packing of the $KVOF_3$-β system due to the size effect of the Rb^+ cation. The cell is viewed along axis *a*. There is an elongation of axis *c* and compression of axis *b* compared with V-3.

Table 3. 7 selected bond lengths and bond valence sums for $RbVOF_3$-α.

Bond	Bond length (Å)	S_{ij}
V – O1	1.591(8)	1.685
V – F2	1.876(6)	0.621
V – F3 x2	1.947(2)	0.513 x2
V – F1	1.953(6)	0.505
V – F1	2.164(7)	0.285
		ΣV=4.122

Table 3. 8 selected bond lengths and bond valence sums for $RbVOF_3$-β.

Bond	Bond length (Å)	S_{ij}
V – O1	1.588(10)	1.520
V – F2	1.903(9)	0.581
V – F1	1.957(9)	0.502
V – F3 x2	1.961(7)	0.497 x2
V – F1	2.180(9)	0.275
		ΣV=3.873

The packing angles between the vanadium oxyfluoride ladders in V-3 and V-4 are skewed further from near perpendicular and parallel when compared to V-1 and V-2. The different packing arrays can be attributed to the different synthetic temperatures, with size effect of the Rb^+ cation also being a cause of the packing distortion. Interestingly, the change in cell size for V-3 and V-4 do not correspond with the change in cell volume seen in V-1 and V-2. V-3 is V = 381.81(9) $Å^3$ while V-4 increases in size with temperature to V = 388.59(3) $Å^3$. Both compounds crystallise in orthorhombic space group *Pbam*, but are not isostructural. There are larger variations in cell lengths between V-3 and V-4 compared with V-1 and V-2. V-4 shows an elongation of axis *c* and a compression of axis *b* compared to V-3, with similar axis a lengths. A – O and A – F bond lengths for V-1 to V-5 are presented in Table 3. 9, illustrating the differences in A^+-cation environment between each compound.

Table 3. 9: The A – O and A – F distances in V-1 to V-5.

Compound	A – O bond length (Å)	A – F bond length (Å)
V – 1 $KVOF_3$-α	K1 – O2 x2 2.839(3)	K1 – F2 x2 2.652(4)
		K1 – F1 x2 2.826(4)
		K1 – F3 2.847(1)
		K1 – F4 2.886(8)
	K2 – O1 x2 2.806(3)	K2 – F1 x2 2.654(3)
		K2 – F2 x2 2.735(3)
		K2 – F3 2.886(5)
V – 2 $KVOF_3$-β	K1 – O1 x2 2.802(5)	K1 – F4 x2 2.657(6)
		K1 – F3 x2 2.713(1)
		K1 – F2 2.843(3)
	K2 – O1 x2 2.851(2)	K2 – F3 x2 2.656(1)
		K2 – F4 x2 2.812(1)
		K2 – F2 2.813(3)
		K2 – F1 2.875(8)
V – 3 $RbVOF_3$-α	Rb – O1 x2 2.935(8)	Rb – F1 x2 2.822(9)
		Rb – F2 x2 2.874(5)
		Rb – F3 3.204(5)
V – 4 $RbVOF_3$-β	Rb – O1 x2 3.016(3)	Rb – F1 x2 2.852(2)
		Rb – F2 x2 2.888(6)
		Rb – F3 3.087(5)
V – 5 $CsVOF_3$	Cs – O1 x2 3.183(6)	Cs – F1 x2 3.023(7)
		Cs – F3 x2 3.076(7)
		Cs – F3 x2 3.157(2)
		Cs – F2 3.277(7)

The NH_4VOF_3 (V-6) system, synthesised at 160 ^oC, displays unit cell and ladder packing similarities with the $RbVOF_3$-α (V-3) system (Fig. 3. 12). $CsVOF_3$ (V-5) has ladder packing somewhere in between that displayed in V-3 and V-4 (Fig. 3. 13.) V-3, V-5 and V-6 are isostructural, with ladder packing arrangements all essentially

the same, with subtle differences discussed above. Several attempts were made to synthesise a polymorph of V-5 at temperatures at and above 160 ^{o}C, but were unsuccessful. Regardless of the temperature used the same structure always crystallised. This could be due to the nature of the heavy of Cs^{+} cation, which doesn't allow any alternate arrangement of the vanadium oxyfluoride ladders. Selected V – O and V – F bond lengths along with bond valence sums for V-6 and V-5 are shown in Table 3. 10 and Table 3. 11 respectively.

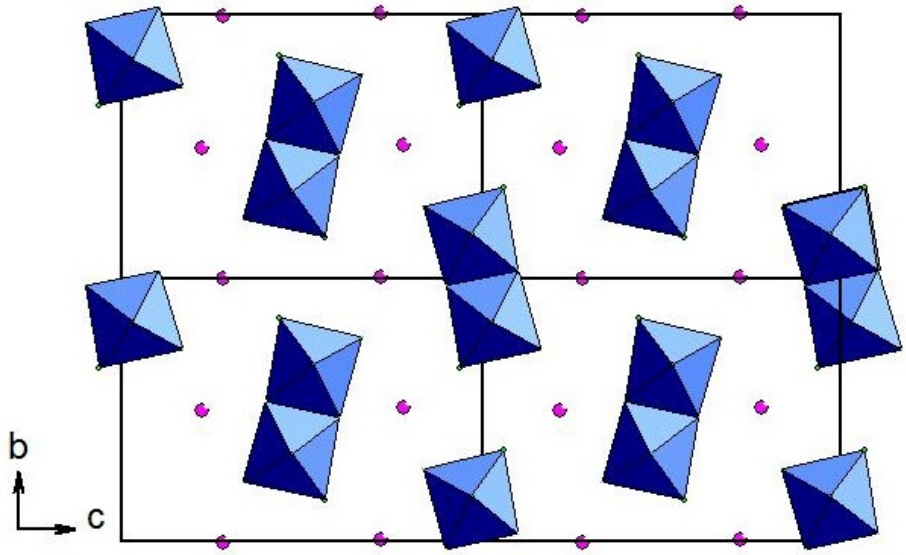

Fig. 3. 12: Extended packing of the structure depicting the 2x2 unit cell of NH_4VOF_3 showing ladder packing similarities with $RbVOF_3$-*α*. The cell is viewed down axis *a*.

Table 3. 10 selected bond lengths and bond valence sums for NH_4VOF_3.

Bond	Bond length (Å)	S_{ij}
V – O1	1.587(5)	1.703
V – F3	1.894(4)	0.592
V – F2 x2	1.935(2)	0.530 x2
V – F1	1.958(4)	0.498
V – F1	2.154(4)	0.293
		ΣV=4.146

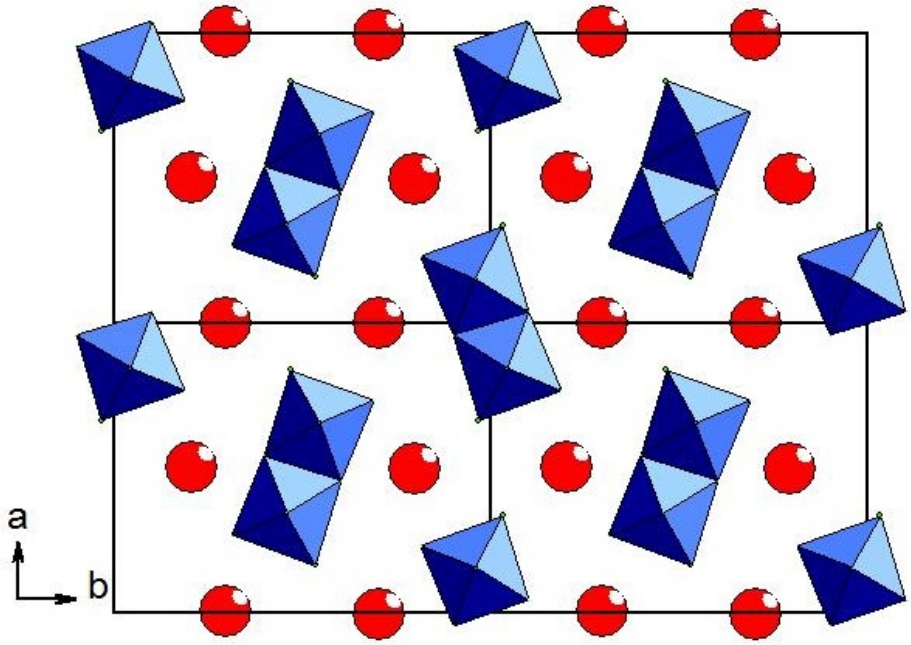

Fig. 3. 13: Extended packing if the structure depicting the 2x2 unit cell of $CsVOF_3$ showing the distortion of the packed vanadium oxyfluoride ladders. The cell is viewed along the *c* axis.

Table 3. 11 selected bond lengths and bond valence sums for $CsVOF_3$ (V-6).

Bond	Bond length (Å)	S_{ij}
V – O1	1.600(8)	1.627
V – F3	1.898(6)	0.586
V – F2 x2	1.972(1)	0.479 x2
V – F1	1.965(6)	0.501
V – F1	2.168(6)	0.282
		ΣV=3.954

Another difference between the compounds is the 'type' of chains which they exhibit. The K^+ systems exhibit symmetry-lowering effects in the form of chain 'doubling' (zig-zag) (Fig. 3. 14), whereas in the Rb^+, Cs^+ and NH_4^+ systems the ladders are trans (Fig. 3. 15). Despite this difference in symmetry, the V – V intra-ladder distances remain in fairly similar ranges for all compounds; these are listed in Table 3. 12. When the $KVOF_3$-α ladders are superimposed it can be seen that the zig-zag formation alternates (Fig. 3. 16) in order to create space for the K^+ cations.

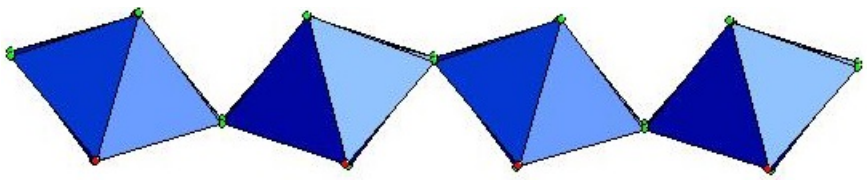

Fig. 3. 14: The zig-zag ladder conformation of the $KVOF_3$-α & β compounds.

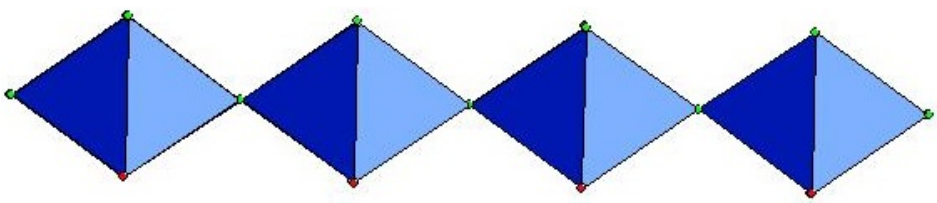

Fig. 3. 15: The trans ladder conformation of the Rb^+, Cs^+ and NH_4^+ compounds. V – V distances range from 3.31-3.34 $\AA$ between 'rungs' and 3.79-3.91 $\AA$ between 'legs'.

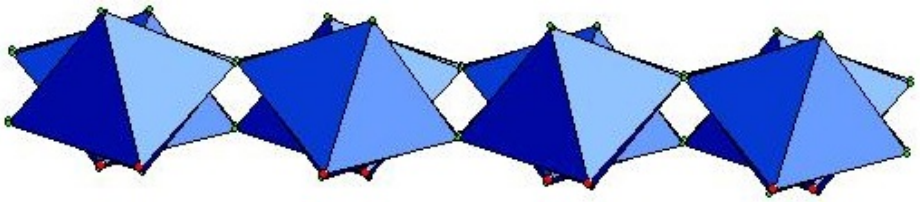

Fig. 3. 16: The superimposition of two nearest-neighbour ladders showing the alternate zig-zag conformation of the $KVOF_3$ structure.

Table 3. 12 V – V intra-ladder distances.

Compound	'Rung' V – V distance (Å)	'Leg' V – V bond length (Å)
$KVOF_3$-α	3.34(2)	3.86(3)
$KVOF_3$-β	3.34(2)	3.71(4)
$RbVOF_3$-α	3.32(1)	3.87(2)
$RbVOF_3$-β	3.33(2)	3.88(5)
$CsVOF_3$	3.31(1)	3.91(3)
NH_4VOF_3	3.32(1)	3.84(3)
$(VO)_2P_2O_7$	3.18(3)	3.87(4)

The vanadium oxyfluoride ladder system present in all six compounds bears a resemblance to the ladder system of vanadyl phosphate, $(VO)_2P_2O_7$ (Fig. 3. 17). This compound has been widely studied due to its magnetic and catalytic properties.[25, 26] The magnetic properties are dependent on the V – O bonding and the inter-ladder interactions. The main difference between the vanadyl phosphate ladders and the vanadium oxyfluoride ladders is the bridging anion between vanadium centres, oxygen in the former and fluorine in the latter.

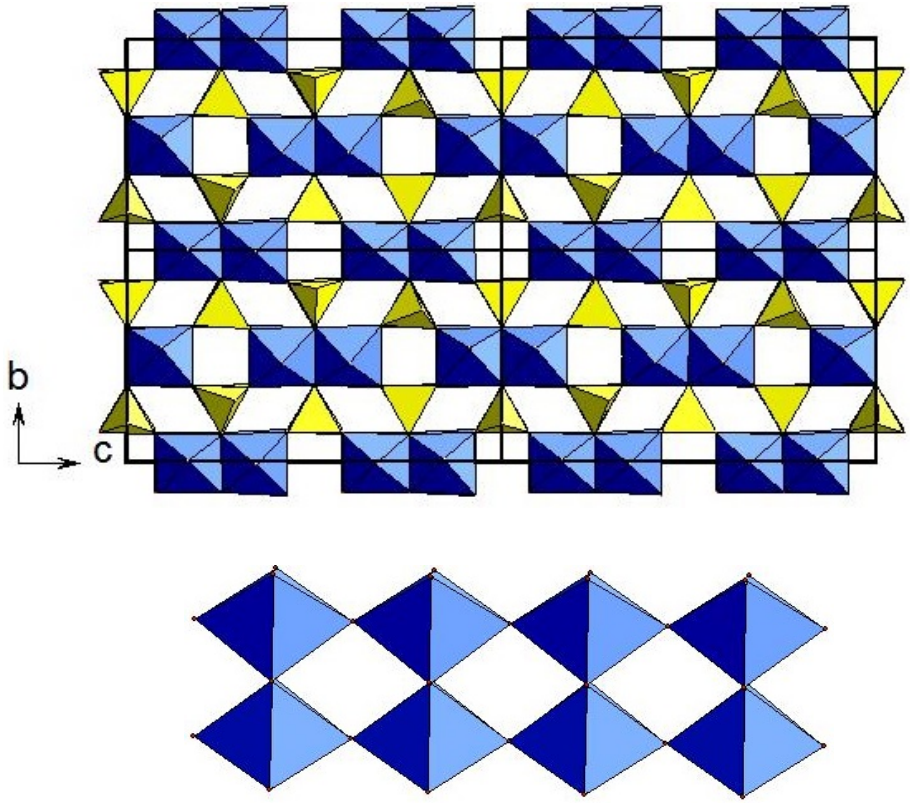

Fig. 3. 17: (Top) Extended structure depicting the 2x2 unit cell of $(VO)_2P_2O_7$ showing parallel packing of the vanadium oxide ladders, connected through phosphate tetrahedral units. There is a striking similarity between the packing in $(VO)_2P_2O_7$ and $KVOF_3$-α. The cell is viewed down axis a. (Bottom) The linear vanadium oxide ladders that comprise the vanadyl phosphate structure.

The octahedral units of each compound display distortions characteristic of vanadium (IV). That is, there is a short V – O, vanadyl, bond approximately 1.6 Å in length along with an elongated trans V – F bond, approximately 2.2 Å, to compensate. This is another difference, as the vanadyl bond in $(VO)_2P_2O_7$ bridges the intra-ladder vanadium centres where as in the $AVOF_3$ structures the vanadyl bond is terminal and the intra-ladder vanadium atoms are bridged by fluorine. These differences in structure and bonding will lead to a change in magnetic properties between the materials.

The inter-ladder interactions vary a great deal among all the structure types. Adjacent ladders in vanadyl phosphate are connected by strong covalent bonds

through tetrahedral phosphate groups (Fig. 3. 18). This leads to medium-range V – V interactions of around 5.01 Å. The corresponding interactions in the vanadium oxyfluoride compounds are mediated by the alkali metal counter-cations K^+ (Fig. 3. 19), Rb^+ (Fig. 3. 20) and Cs^+, or hydrogen bonding through NH_4^+ in the case of V-6 (Fig. 3. 21). These compounds exhibit much longer V – V interactions, in the region of 5.91 Å. All inter-ladder V – V, O – O and F – F distances are given in Table 3. 13 and Table 3. 14 respectively.

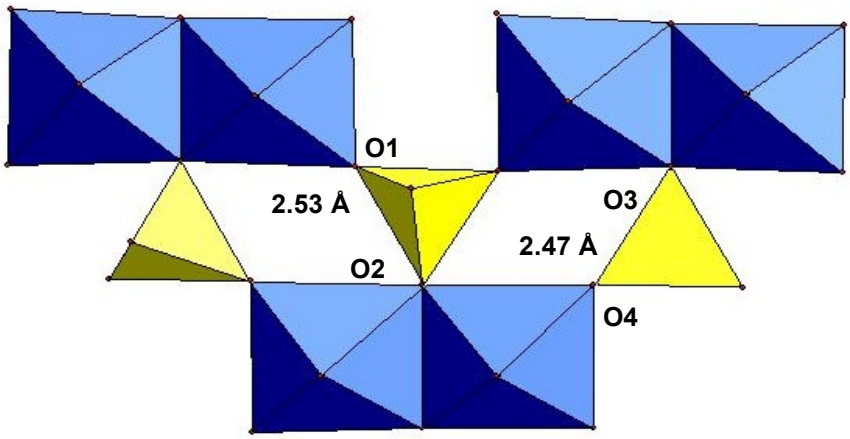

Fig. 3. 18: Inter-chain interactions in $(VO)_2P_2O_7$ showing the O – O distances between adjacent ladders.

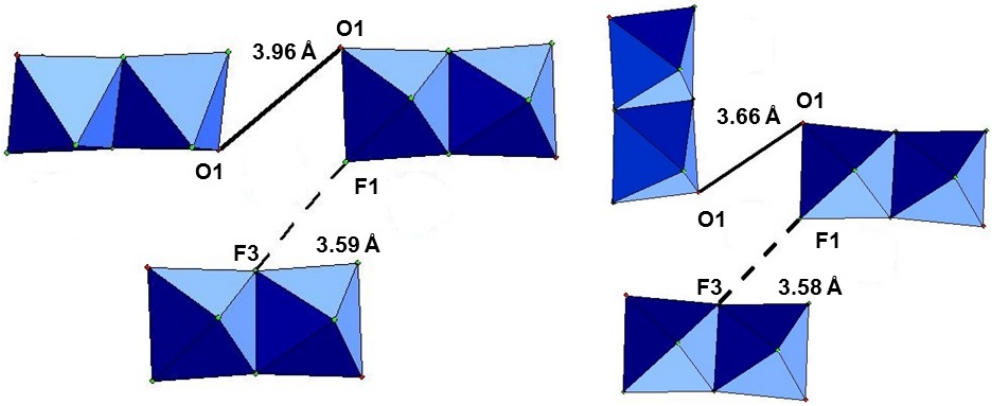

Fig. 3. 19: Inter-chain distances in $KVOF_3$-α (left) and $KVOF_3$-β (right), illustrating the effect that the packing orientation has on the O – O and F – F distances between ladders.

Table 3. 13 V – V Inter-ladder distances.

Compound	V – V distance (Å)
$KVOF_3$-α	5.93(3)
$KVOF_3$-β	5.88(4)
$RbVOF_3$-α	5.85(3)
$RbVOF_3$-β	5.91(3)
$CsVOF_3$	5.99(5)
NH_4VOF_3	5.92(3)
$(VO)_2P_2O_7$	4.88(4)

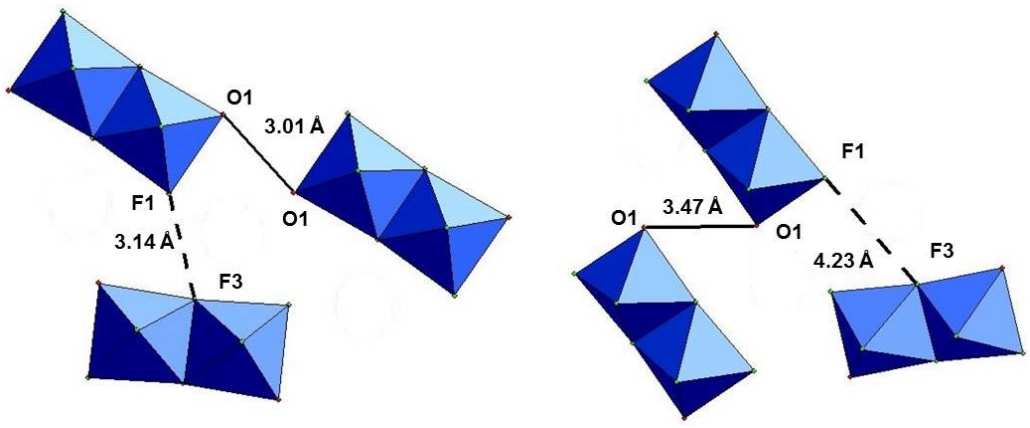

Fig. 3. 20: Inter-chain interactions in $RbVOF_3$-α (left) and $RbVOF_3$-β (right), illustrating the effect that the packing orientation has on the O – O and F – F distances between ladders.

The large differences in the V – V distances caused by the ladder packing leads to some interesting variations in O – O and F – F bond lengths in the $AVOF_3$ compounds. The ladders or V-2 are rotated 90 ^{o} along the ladder leg and then rotated 180 ^{o} along the rung relative to V-1. This leads to an O – O bond length difference of 0.3 Å between the two compounds while the F – F distances remain similar.

Table 3. 14 O – O and F – F inter-ladder distances.

Compound	O – O distance (Å)	F – F distance (Å)
$KVOF_3$-α	3.96(3)	3.59(5)
$KVOF_3$-β	3.66(4)	3.58(5)
$RbVOF_3$-α	3.01(1)	3.14(3)
$RbVOF_3$-β	3.47(3)	4.23(3)
$CsVOF_3$	3.05(3)	3.19(4)
NH_4VOF_3	4.23(2)	3.17(2)
$(VO)_2P_2O_7$	2.53(3) & 2.47(4)	n/a

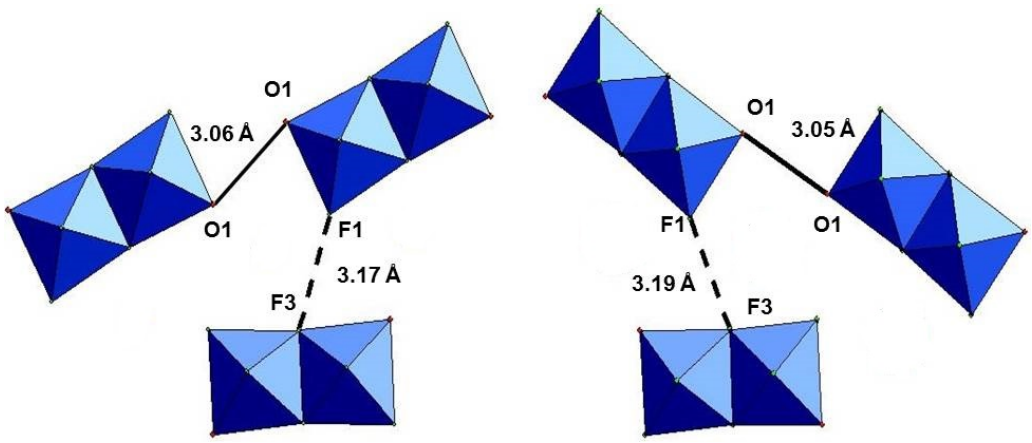

Fig. 3. 21: Inter-chain interactions in NH_4VOF_3-α (left) and $CsVOF_3$-β (right), illustrating the effect that the packing orientation has on the O – O and F – F distances between ladders.

The O – O and F – F bond lengths vary a great deal more between V-3 and V-4. The rearrangement of the ladder packing is more pronounced, as the ladders are not simply rotated but also translated through space, leading to an elongation of the F – F and O – O distances by 1.09 Å and 0.46 Å, respectively. The longer distances in V-3 and V-4 compared to V-1 and V-2 are due to the mediation of the Rb^+ and K^+ counter-cations, and their relative atomic radii.

V-3 compares well to V-5 and 6 in terms of O – O and F – F distances due to the similarities in symmetry and ladder packing. V-4 is more comparable with V-2 in terms of O – O distances, but shows no similarity with their F – F distances. This highlights the effects that simple symmetry changes can have on the structure of analogous compounds. The effect of the counter-cation species used along with variations in temperature also has an effect on the structural properties of the compounds. The following section will discuss the effects that these structural differences have on the magnetic properties of the compounds.

3.1.4 Magnetic measurements

DC magnetic susceptibilities for V-1 to V-3 were measured in an applied field of 1 T from 2 K to 300 K. This was done in a zero field cooled (ZFC) and field cooled (FC) cycle. The magnetic properties of $RbVOF_3$-α, $CsVOF_3$ and NH_4VOF_3 have been previously reported.[1] The magnetic properties of the three new polymorphs have been investigated for comparison to the original two structures. At high temperatures, above 150 K, the samples follow Curie-Weiss behaviour (Fig. 3. 22) described by Eqn. 3. 1

$$\chi^{-1} = \left(\frac{C}{T - \theta}\right)$$

Eqn. 3. 1

The data were fitted between 150 K and 300 K yielding Weiss temperatures, θ, Curie constants, C, and effective magnetic moments, μ_{eff}, for V-1,2 and 3 were extracted and are presented in Table 3. 15. The effective magnetic moments for each sample show a reasonable correlation to $S = ½$, having approximately 1.73 μB. The Curie-Weiss fits are comparable to the analogous existing structures (Fig. 3. 22) between 150 and 300 K.

Table 3. 15 Weiss temperatures, Curie constants and effective magnetic moments for V-1, 2 and 3.

Compound	Weiss temperature, θ (K)	Curie constant, C, K emu mol^{-1}	μ_{eff}, μB
V-1 $KVOF_3$-α	-67.1(1)	0.489(2)	1.99
V-2 $KVOF_3$-β	-17.9(2)	0.297(4)	1.54
V-3 $RbVOF_3$-β	-157.2(2)	0.536(9)	2.07
$RbVOF_3$-α[1]	-122.9(3)	0.242(4)	1.39
$CsVOF_3$[1]	-92.2(5)	0.401(4)	1.79
NH_4VOF_3	-66.1(3)	0.304(5)	1.91
$[C_{12}H_{12}N_2]½VOF_3$[1]	-27.4(7)	0.456(4)	1.56

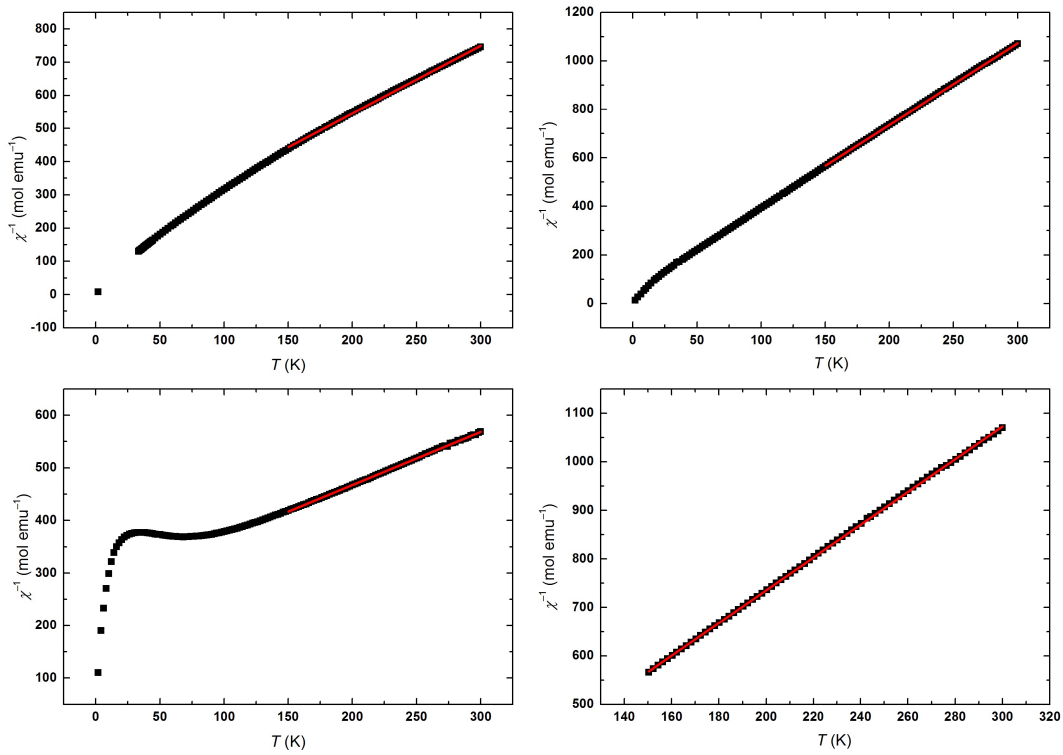

Fig. 3. 22: Inverse susceptibility plots of $KVOF_3$-α (top left), $KVOF_3$-β (bottom left), $RbVOF_3$-α (top right) and $[C_{12}H_{12}N_2]½VOF_3$[1] (bottom right) with the red line indicating the Curie-Weiss fit between 150 K and 300 K.

The derived effective magnetic moments vary between samples from 1.39 μB to 2.07 μB. Interestingly there are some rather large differences in μ_{eff} between V-1 and V-2. However, it is worth noting that these μ_{eff} values are derived from the fits and may be due to differences in sample size and centering during the measurement process. Since the rungs of the ladder are all bridged via fluorine this leaves the vanadyl bonds free for inter-ladder interactions. A similar effect is displayed by V-3 and V-4, which have a greater degree of difference in O – O distances compared with V-1 and V-2, and hence a larger difference between $\mu_{eff.}$ $CsVOF_3$ displays a μ_{eff} that most closely resembles that of a $S = ½$ system (1.79 μB) when a Curie-Weiss fit is applied between 150 K and 300 K. Below 150 K, data are plotted as graphs of χ vs. T and fitted with different mathematical functions depending on their behaviour.

$KVOF_3$-α and β were fitted using Bleaney-Bowers dimer models and 1D Heisenberg chain models (Fig. 3. 23). Both samples show a sharp upturn of χ vs T At temperatures below 25 K, which seems to indicate the presence of paramagnetic impurites based on the data from previously analysed compounds.[1] Each fit was then given an added Curie-Weiss term to account for any paramagnetic impurity contributions.

The 1D Heisenberg chain gives a better overall fit to the data than the Bleaney-Bowers dimer model. The Heisenberg model allows the spins of each metal atom in the chain to adopt any orientation, so the magnetic interactions occur along the 'leg' of the ladder. The Bleaney-Bowers model is a spin 1 dimer, with ferromagnetic or anitferromagnetic spins, so the magnetic interactions occur across the 'rung' of the ladder.

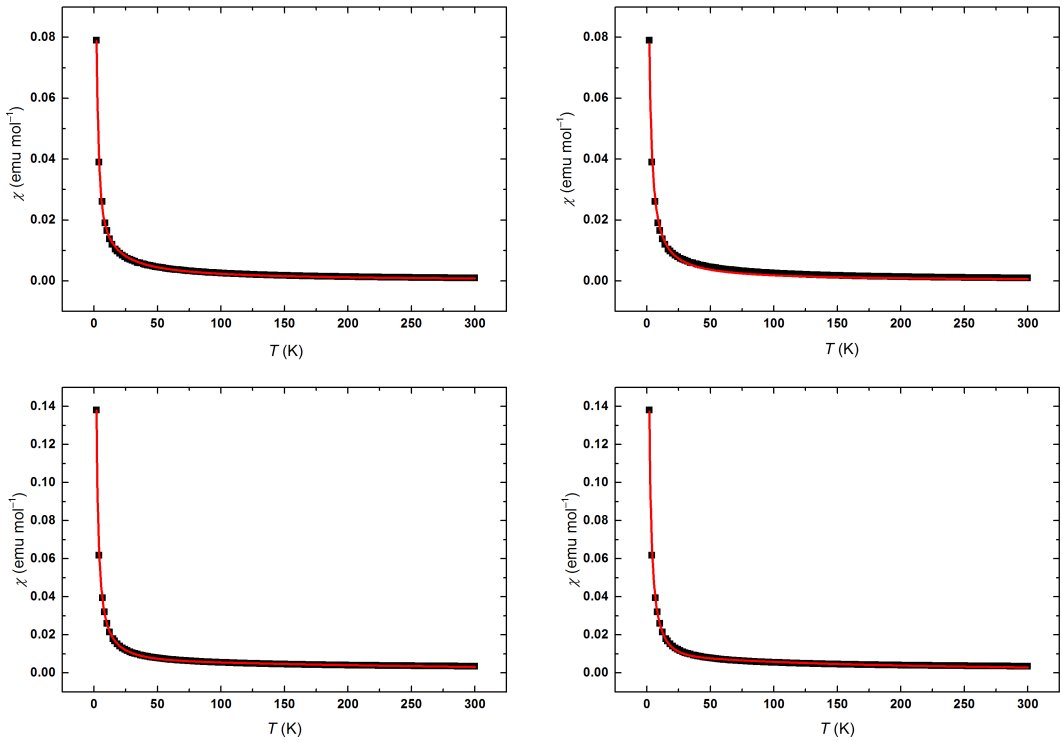

Fig. 3. 23: The 1D Heisenberg chain models (left) and Bleaney-Bowers dimer models (right) fit to $KVOF_3$-α (top) and $KVOF_3$-β (bottom). The black dots are the measured samples and the red lines are the fitted models.

It is not possible to obtain reliable values of μ_{eff} from the Heisenberg chain fits due to the paramagnetic impurities in each sample. Both samples are antiferromagnetic in nature, with values of μ_{eff} based on the inverse susceptibility plots for V-1 and V-2 are somewhat different from the ideal spin-only value for a spin ½ magnetic moment (1.73 μB). This could be explained by the octahedral distortions present caused by the short vanadyl bonds, displacing vanadium from its central position in the octahedral unit (Fig. 3. 24). This, however, does not explain the disparity between each sample, as both display similar octahedral distortions and V – V distances 5.93 Å (V-1) and 5.88 $\AA$ (V-2) respectively). Since the vanadyl bonds lie exo to the ladder, the interaction pathways are via V – F – V bonds along the ladder legs. Therefor the main magnetic interactions of V-1 and V-2 occur along the legs of the ladder and not across the rungs, leaving Heisenberg fit as the more favourable option. V-1 has longer V – V distances in the ladder leg due

to the zig-zag nature of the ladders being more pronounced in V-2. Values of *J* have been extracted from the Heisenberg fits, again with large differences between V-1 (19.6(8) K) and V-2 (5.4(3) K). Values of *J* have also been extracted from the Bleaney Bowers fits, (15.8(3) K and 3.8(1) K). The more pronounced zig-zag V – F – V bonds in V-2 weakens the magnetic interactions.

This may also go some way to explaining the large calculated difference in μ_{eff} and extraced *J* values between the two compounds. Since the extracted Heisenberg *J* are greater than the extracted Bleaney Bowers values, it implies that the magnetic interactions are occurring along the 'legs' of the ladders and not across the 'rungs'.

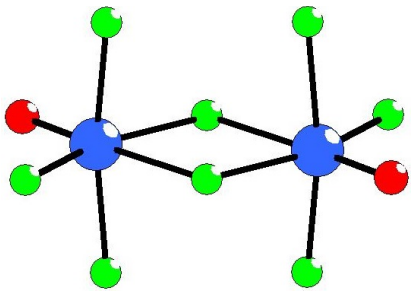

Fig. 3. 24: The vanadium displacement in the octahedral units, showing the short vanadyl bond and elongated V – F bond to compensate. This causes the deviation of μ_{eff} from its ideal value in sample V-1 and V-2.

$RbVOF_3$-β was fitted using 1D Heisenberg chain and Bleaney-Bowers dimer models with an added Curie-Weiss term to compensate for the paramagnetic impurities (evidenced by the sharp upturn of χ vs T at low temperature). The Heisenberg fit is described by Eqn. 3. 2;

$$\chi(\mathrm{T}) = \chi_{1D}(T) + \chi_{LT}(T)$$

With;

$$\chi_{1D}(T) = \left(\frac{N_A \mu_{eff}^2}{3k_B T}\right)\left[\frac{(1 + 0.08516x + 0.23351x^2)}{(1 + 0.73382x + 0.13696x^2 + 0.53568x^3)}\right]$$

Where;

$$x = \frac{|J|}{K_b T} \text{ And } \chi_{LT} = \frac{C}{(T-\theta)}$$

Eqn. 3. 2

Once again the 1D Heisenberg model gives a better overall fit to the data, particularly around the low temperature region compared to the Bleaney-Bowers model (Fig. 3. 25), however neither provides an ideal fit. The samples display antiferromagnetic behaviour, with the broad maxima indicating low dimensional magnetic interactions. Once again the extracted Heisenberg *J* are greater than the extracted Bleaney Bowers values, implying that the magnetic interactions are occurring along the 'leg' of the ladder and not across the 'rungs'.

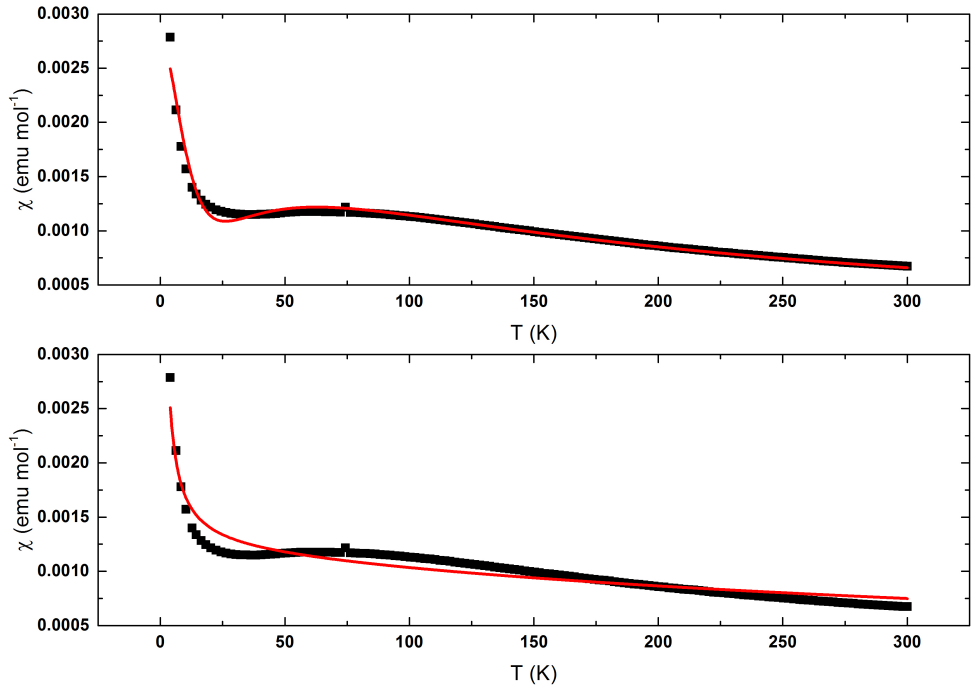

Fig. 3. 25: The 1D Heisenberg chain model (top) and the Bleaney-Bowers dimer model (bottom), fit to $RbVOF_3$-β (V-4). Black dots are the measured sample and the red lines represent the fitted models.

The μ_{eff} of $RbVOF_3$-β (2.07 μB), calculated from the inverse susceptibility between 150 K and 300 K dos not coincide well with the spin only μ_{eff} for a $S = ½$ material (1.73 μB). This is due to the octahedral distortions caused by the short vanadyl bonds, displacing the vanadium away from the centre of each octahedral unit. The sample displays an unusually large μ_{eff} compared to the previously reported sample $RbVOF_3$-α (1.39 μB) which was calculated from the inverse susceptibility between 250 K and 300 K. The *J* values obtained from the 1D Heisenberg models

also differ greatly between compounds. A list of *J* values obtained from the Heisenberg and Bleaney-Bowers models for V-1 through V-3 are given in Table 3. 16, along with *J* values for previously measured analogous structures. V-1 has a parallel packed arrangement of zig-zag ladder units, which matches closely to the structure of $[C_{12}H_{12}N_2]_{½}VOF_3$ which has the same packing arrangement of zig-zag ladders. Both have closely correlating *J* (K) values 19.6 and 20.1 respectively. $RbVOF_3$-*α*, $CsVOF_3$ and NH_4VOF_3 each have similar packing arrangements consisting of linear ladder units, with all three samples exhibiting similar *J* (K) values, 67.0(4), 65.8(2) and 60.3 respectively. $KVOF_3$-*β* adopts similar zig-zag style ladder units as $KVOF_3$-*α*, but the packing of the ladders in each of these systems is markedly different. $KVOF_3$-*β* shows an almost 180 ° shift in one layer of ladders leading to a near perpendicular array.

Table 3. 16: The extracted *J* (K) values for V-1 to V-3 and their analogous structures.

Compound	*J* (K) obtained from 1D Heisenberg chain	*J* (K) obtained from Bleaney-Bowers dimer
V-1 $KVOF_3$-*α*	19.6(8)	15.8(3)
V-2 $KVOF_3$-*β*	5.4(3)	3.8(1)
V-3 $RbVOF_3$-*β*	25.7(6)	20.4(6)
$RbVOF_3$-*α*[1]	67.0(4)	54.2(4)
$CsVOF_3$[1]	65.8(2)	62.6(2)
NH_4VOF_3	60.3(3)	50.8(4)
$[C_{12}H_{12}N_2]_{½}VOF_3$[1]	20.1(2)	n/a

$RbVOF_3$-*β* displays a similarly low values of *J* compared to $RbVOF_3$-*α*. The ladder units of both samples are linear, but the difference is in the packing of the ladders, with $RbVOF_3$-*β* adopting a more perpendicular array compared to $RbVOF_3$-*α*, leading to a shortening of the V – V inter-ladder interactions and weakening any

inter-ladder magnetic interactions that may be occurring. The full packing arrays, viewed along the ladders, of each compound are shown together for clarity (Fig. 3. 26).

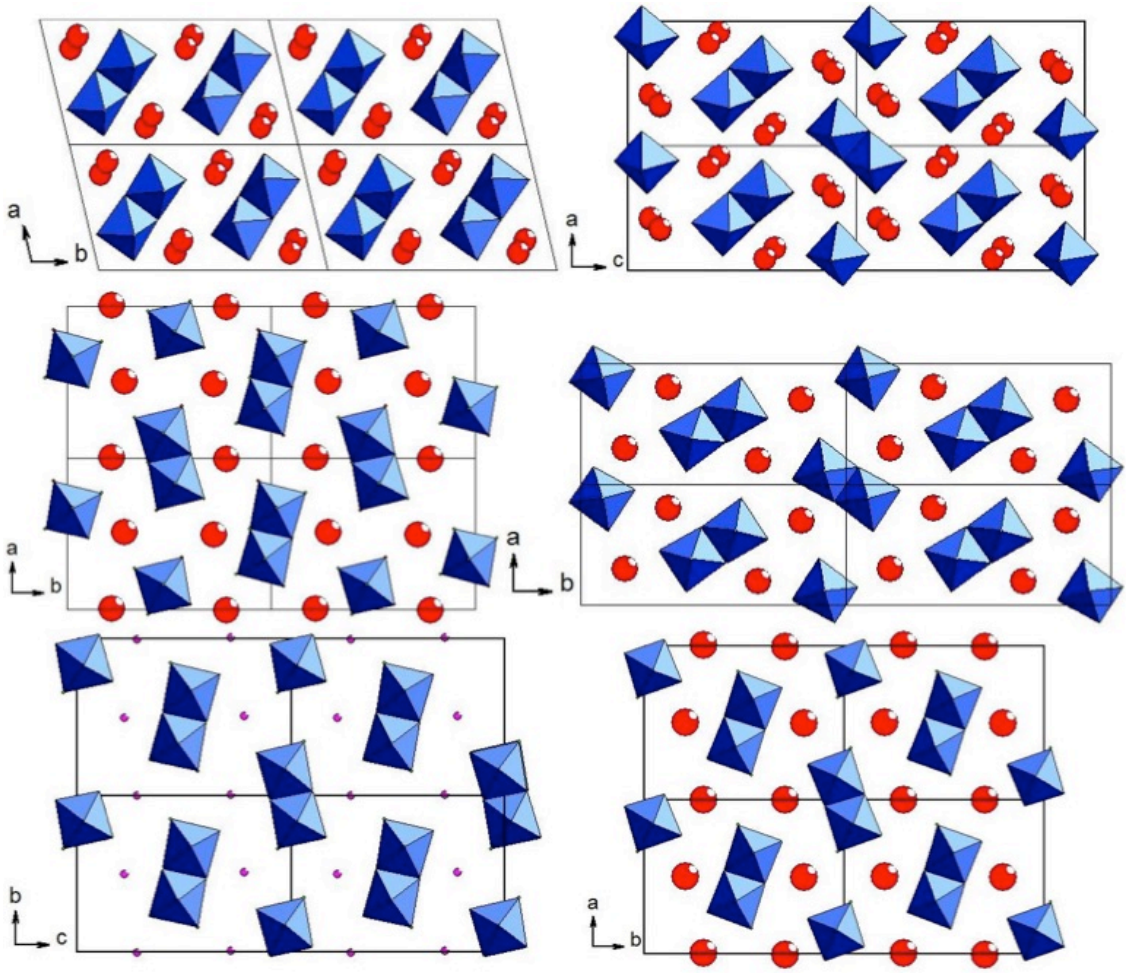

Fig. 3. 26: Ladder packing arrays of the $AVOF_3$ compounds viewed along the ladders. $KVOF_3$-α (top left), $KVOF_3$-β (top right), $RbVOF_3$-α (middle left), $RbVOF_3$-β (middle right), NH_4VOF_3 (bottom left) and $CsVOF_3$ (bottom right). Note the shift from near parallel to near perpendicular (top and middle left compared to top and middle right) as well as the size effects on the ladder arrays as the cations increase in atomic radii.

Magnetic measurements for V-3 and V-5 have been previously carried out (Fig. 3. 27).[1] The analogous structure; $[C_{12}H_{12}N_2]_{1/2}VOF_3$ has also had its magnetic properties measured. V-3 and V-5 both had Bleaney-Bowers dimers and 1D

Heisenberg chains fitted while $[C_{12}H_{12}N_2]_{1/2}VOF_3$ was only fitted with a Heisenberg model. These samples all display similar magnetic interactions with V-1, V-2 and V-4. The samples are antiferromagnetic in nature, and once again the broad maxima indicate low dimensional interactions.

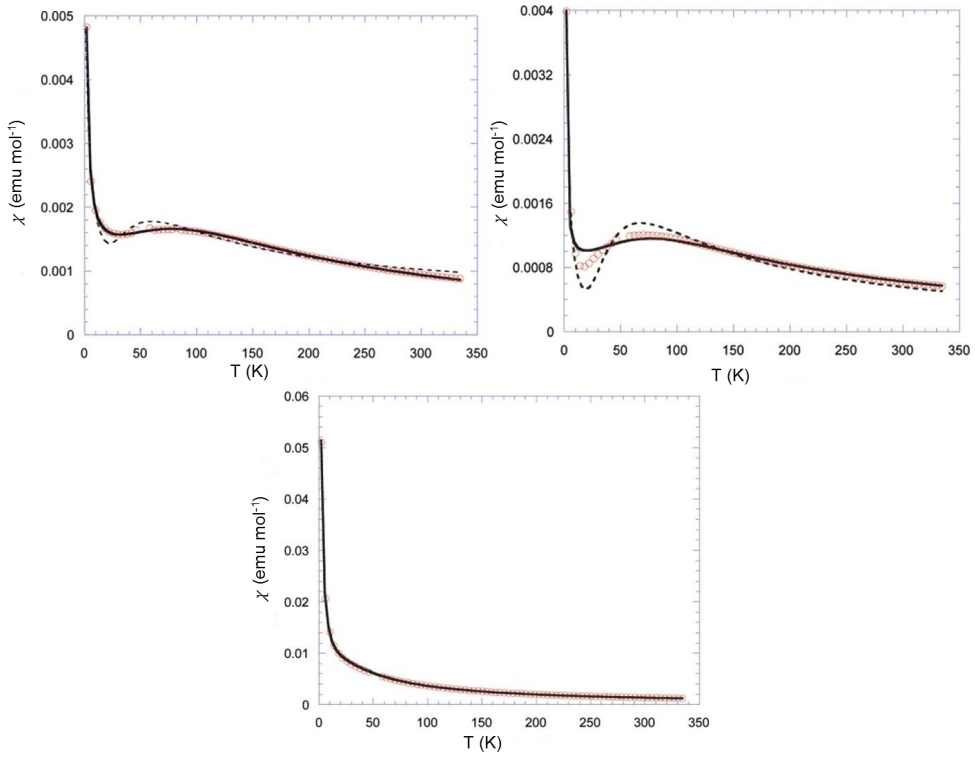

Fig. 3. 27: 1D Heisenberg chain (solid line) and Bleaney-Bowers (dashed line) fits to $CsVOF_3$ (top left), $RbVOF_3$-α (top right) and Heisenberg fit to $[C_{12}H_{12}N_2]_{1/2}VOF_3$ (middle bottom) represented by the red circles. The plots are similar in nature to the plots above, with the Heisenberg models providing a better fit to the data.

All samples display greater extracted *J* values from the 1D Heisenberg models than the Bleaney-Bowers dimers. This implies that in all $AVOF_3$ compounds the magnetic interactions are occurring along the 'legs' of each ladder. This is in stark contrast with $(VO)_2P_2O_7$, which shows a better fit to the Bleaney-Bowers dimer model, and thus the magnetic interactions occur across the 'rungs' of each ladder unit.

3.2 Vanadium (III) Fluoride $S = 1$ Chain Structures

3.2.1 Introduction

This section will discuss the synthesis and characterisation of structural and physical properties of three vanadium (III) fluoride $S = 1$ chains, with comparisons to existing analogous structures.

The combination of HF and an organic template in hydrothermal synthesis is common, with many phosphates and phosphonates being synthesised by this method.[27, 28] Fluorides are often incorporated into these phosphate structures, but there are still relatively few examples of completely fluorinated materials.[29] Vanadium, V^{4+}, tends to be comprised of mixed fluorine and oxygen atoms as ligands.[24] When vanadium is further reduced to its V^{3+} oxidation state it more commonly produces materials where fluorine is the only ligand. $[NH_4]_2NaVF_6$, and Na_3VF_6 are examples of compounds containing isolated $[VF_6]^{3-}$ octahedra that are listed in the Inorganic Crystal Structure Database.[30] Four new reduced V^{3+} chain structures; $[NH_4]_2VF_5$; $[C_2N_2H_{10}]VF_5$; $[C_4N_2H_{12}]VF_5.H_2O$ and; $[C_{10}N_2H_8]VF_3$, were also recently synthesised using the hydrothermal method.[2] Several other vanadium fluoride materials exist that have interesting chain topologies, such as $SrVF_5$ and $BaVF_5$ (Fig. 3. 28).[31, 32]

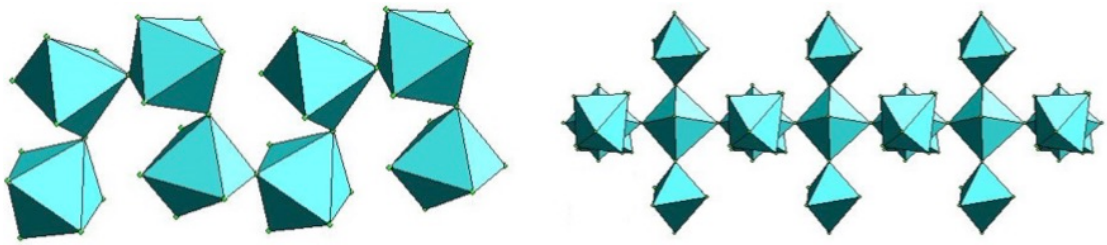

Fig. 3. 28: The corner-sharing vanadium fluoride chains in $SrVF_5$ (left) and $BaVF_5$ (right) bridged through fluorine.

3.2.2 Synthesis

Two distinct crystallographic phases of $[NH_4]_2V_2F_5$: α (V-8) and β (V-7) have been prepared solvothermally along with an analogous structure K_2VF_5 (V-9). These compounds display 1D corner-sharing chains of vanadium (III) fluoride octahedral units, charge balanced by NH_4^+ and K^+ cations, respectively.

Compounds V-7 through V-9 were prepared solvothermally in 40 mL Teflon-lined steel autoclaves.

V-7, $[NH_4]_2VF_5$-β: V_2O_5 (1 mmol, 0.182 g) and NH_4F (3 mmol, 0.111 g) were dissolved in 48% HF (31 mmol, 0.5 mL). A 1:1 ratio of water (1 mmol, 2 mL) and ethylene glycol (32 mmol, 2 mL) was added then sealed and heated at 160 ^oC for 72 hours. The product was comprised of green block-like crystals, implying V(III).

V-8, $[NH_4]_2VF_5$-α: V_2O_5 (1 mmol, 0.182 g) and hexamethylenetetramine (0.5 mmol, 0.071 g) were dissolved in 48% HF (6.2 mmol, 0.1 mL). A 1:1 ratio of water (0.05 mmol, 0.1 mL) and ethylene glycol (1.6 mmol, 0.1 mL) was added then sealed and heated for 24 hours at 130 ^oC. The product was comprised of green needle-like crystals, implying V(III).

V-9, K_2VF_5: K_3VF_6 (1 mmol, 0.282 g), K_2SO_4 (1 mmol, 0.174 g) and KHF_2 (1 mmol, 0.078 g) were dissolved in 48% HF (62 mmol, 1 mL) and water (0.5 mmol, 1 mL). this mixture was sealed and heated at 200 ^oC for 24 hours. The product was comprised of green block-like crystals, implying V(III)

The K_3VF_6 was prepared via solid state synthesis by mixing V_2O_3 and KHF_2 in stoichiometric ratios and heating them at 300 ^oC in a copper boat. The aparatus was set up in a sealed tube furnace with an argon flow at one end and a calcium carbonate receptor at the other (to capture and neutralise any HF gas evolved during the reaction).

V-7 through V-9 were filtered and washed with water, all crystals were of a green colour indicating vanadium (III) and had block-like morphologies. V-8 has been previously synthesised and characterised, but is included in this section for comparison.[2] Samples were assessed for purity, initially, by eye, as it was obvious that the samples were not phase pure if there was the presence of black powder along with the blue-coloured crystals. If a mixed phase was present, the desired samples were separated using an optical microscope for diffraction experiments.

3.2.3 Structural characterisation

V-7 through V-9 exhibit 1D chains comprised of VF_6 building units (Fig. 3. 29). The chain structure is comprised of corner-sharing $[VF_4F_{1/2}]$ octahedral units forming either zig-zag (Fig. 3. 30) or trans chains (Fig. 3 .31). The chains are packed and 'surrounded' by the counter-cations to form the 3D unit cell viewed along the a axis (Fig. 3. 32).

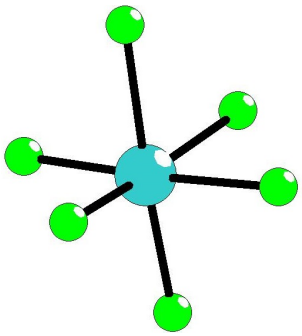

Fig. 3. 29: The VF_6 building unit in V-7 – V-9.

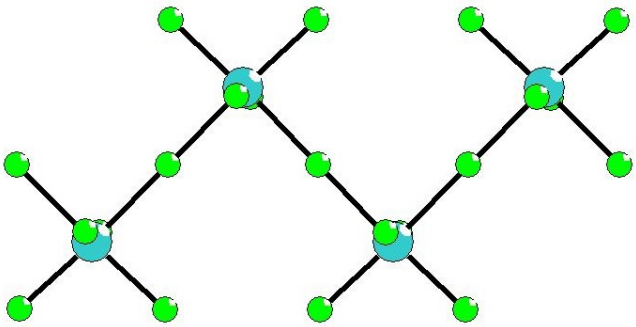

Fig. 3. 30: The zig-zag chain of $[VF_4F_{1/2}]$ corner-sharing octahedral units.

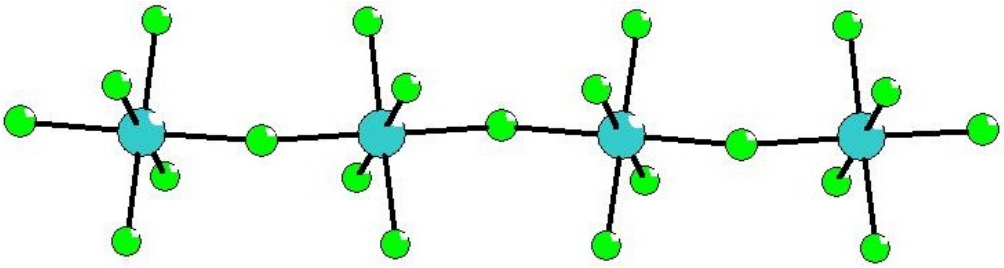

Fig. 3. 31: The trans chain of $[VF_4F_{1/2}]$ corner-sharing octahedral units.

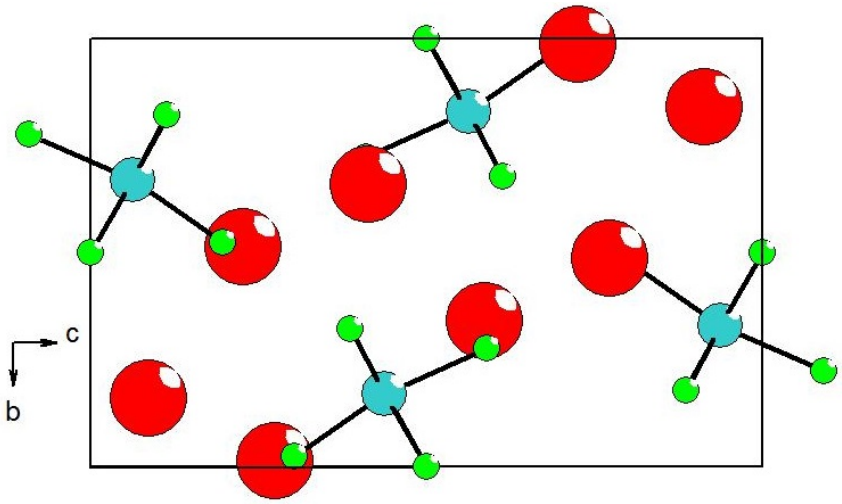

Fig. 3. 32: Packed chains and counter-cations in the A_2VF_5 unit cell, where A = NH_4^+ or K^+.

The $[NH_4]_2VF_5$-β (V-7) system (synthesised at 160 ^oC) crystallises in the orthorhombic space group P*nma* and displays 'zig-zag' vanadium fluoride ladders, seen when viewed along the *b* axis (Fig. 3. 33). $[NH_4]_2VF_5$-α (V-8) system (synthesised at 130 ^oC) crystallised in the orthorhombic space group *Pnma*, and adopts trans vanadium fluoride chains, seen when viewed along axis a (Fig. 3. 34). Selected V – F bond lengths along with bond valence sums for V-7 and V-8 are shown in Table 3. 17 and Table 3. 18 respectively.

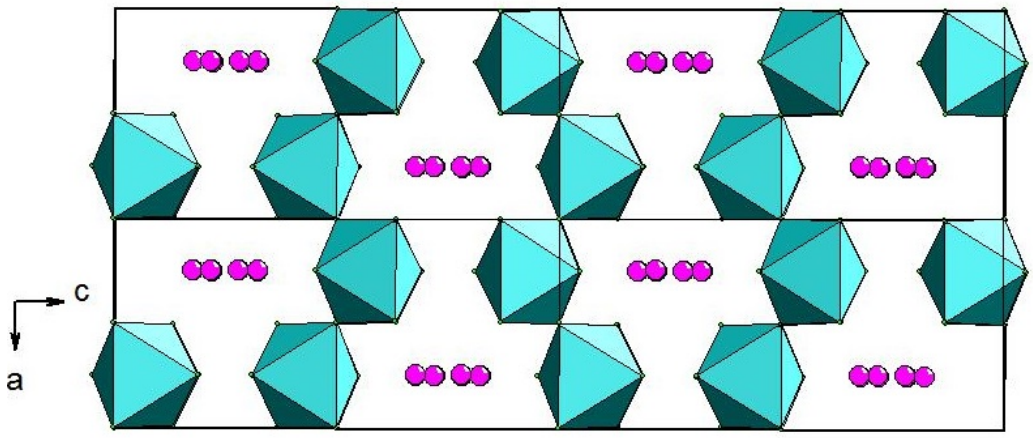

Fig. 3. 33: The extended 2x2 unit cell of $[NH_4]_2VF_5$-β displaying the 'zig-zag' type corner-sharing vanadium fluoride chains. The cell is viewed along the *b* axis.

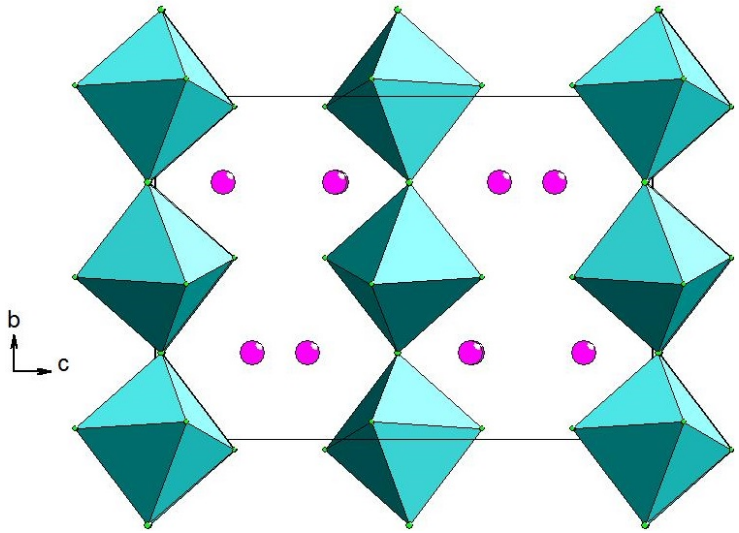

Fig. 3. 34: The extended 2x2 unit cell of $[NH_4]_2VF_4$-α displaying the trans type corner-sharing vanadium fluoride chains, viewed along axis *a*.

Table 3. 17 selected bond lengths and bond valence sums for $[NH_4]_2VF_5$-β.

Bond	Bond length (Å)	S_{ij}
V – F4 x2	1.779(1)	0.812 x2
V – F3	1.944(2)	0.520
V – F4	1.946(3)	0.517
V – F1 x2	2.085(3)	0.355 x2
		ΣV=3.371

K_2VF_5 exhibits the same kind of zig-zag chain structure as $[NH_4]_2VF_5$-β (Fig. 3. 35). Selected V – F bond lengths along with BVS calculations for V-9 are given in Table 3. 19.

Table 3. 18 selected bond lengths and bond valence sums for $[NH_4]_2VF_5$-α.

Bond	Bond length (Å)	S_{ij}
V – F3 x2	1.901(5)	0.584 x2
V – F2 x2	1.907(5)	0.575 x2
V – F1 x2	1.989(2)	0.460 x2
		ΣV=3.238

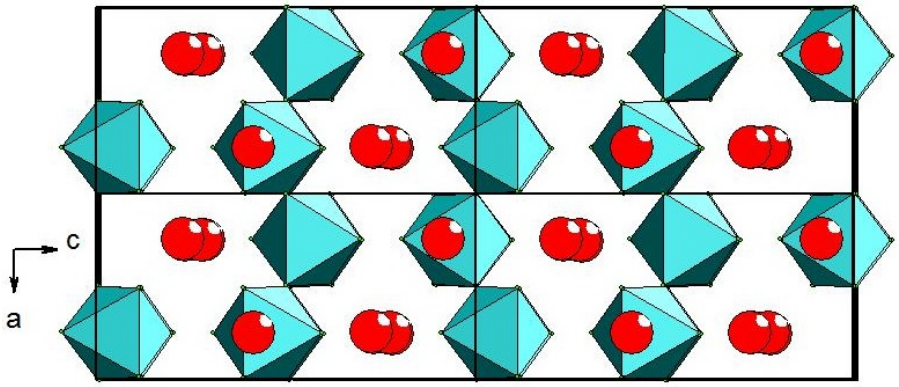

Fig. 3. 35 The extended 2x2 unit cell of K_2VF_5 displaying the 'zig-zag' type corner-sharing vanadium fluoride chains seen in NH_4VF_5-α. The cell is viewed along axis *b*.

Table 3. 19 selected bond lengths and bond valence sums for K_2VF_5.

Bond	Bond length (Å)	S_{ij}
V – F2 x2	1.860(3)	0.652 x2
V – F3	1.885(5)	0.610
V – F4	1.927(4)	0.544
V – F1 x2	2.030(1)	0.412 x2
		ΣV=3.282

Temperature effects have once again been shown to have a large impact on the outcome of structural properties of these materials. The two coumpounds synthesised at higher temperatures both exhibit the zig-zag style of vanadium fluoride chain, effectively condensing the *b* axis. The lower temperature compound exhibits a more linear trans-type chain, with a longer *a* axis but shorter *c* axis. The magnetic properties of V-7 and V-9 have been measured and will be compared to the behaviour of V-8 which has been previously reported.

3.2.4 Magnetic measurements

DC magnetic susceptibilities for V-7 and V-9 were measured in an applied field of 1 T from 2 K to 300 K. This was done in a zero field cooled (ZFC) and field cooled (FC) cycle. At temperatures above 150 K, K_2VF_5 (V-9) follows Curie-Weiss behaviour (Fig. 3. 36) with a good fit and providing a μ_{eff} close to the expected value for a $S = 1$ compound. The data for $[NH_4]_2VF_5$-β shows a reasonable correspondence to Curie-Weiss between 150 K and 300 K, but they were also split into two separate fits from 150 K to 225 K and 225 K to 300 K (Fig. 3. 36). The μ_{eff} for all fits for samples along with extracted Curie constants, C, and Weiss temperatures, θ, are given in Table 3. 20

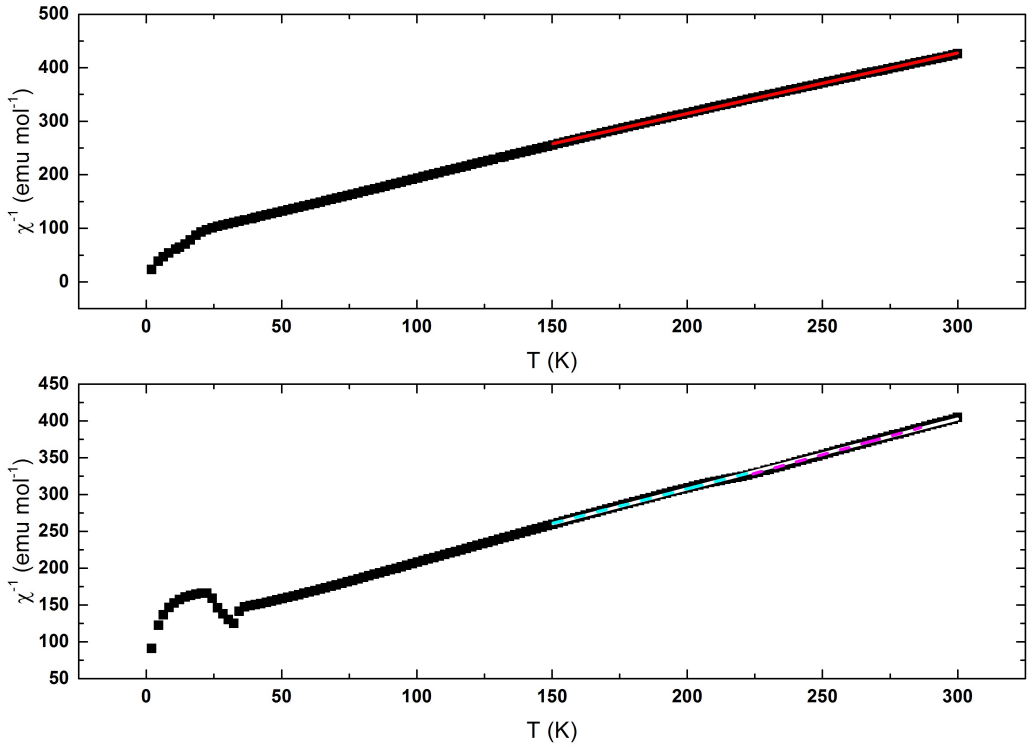

Fig. 3. 36: Inverse susceptibility plot of K_2VF_5 (top) the red line for K_2VF_5 indicates the Curie-Weiss fit between 150 K and 300 K. Inverse susceptibility plot of $[NH_4]_2VF_5$ (bottom) the white line indicates the Curie-Weiss fit between 150 K and 300 K, the dashed blue line indicates the fit between 150 K and 225 K and the dashed pink line indicates the fit between 225 K and 300 K.

Table 3. 20 The extracted Weiss temperatures, Curie constants and effective magnetic moments for V-7 and V-9. V-7 has been split into the three component lines.

Compound	Weiss temperature, θ, K	Curie constant, C, emu mol^{-1}	μ_{eff}, μB
K_2VF_5 (V-9)	-77.9(3)	0.89(1)	2.66
$[NH_4]_2VF_5$-β (V-7)	-100.5(4)	0.99(1)	2.81
	-127.8(4)	1.07(3)	2.92
	-123.7(2)	1.05(2)	2.90

The μ_{eff} for K_2VF_5 shows a greater deviation from the spin only value for a V(III) structure (2.83 μB), while all three values extracted for $[NH_4]_2VF_5$ show very good correlation with the spin only effective magnetic moment. It is unclear whether the dip in the Curie-Weiss fit for V-7 is a genuine structural phase transition, as single crystal data have been collected at LT (173 K) and RT (289 K) for this sample and shows no change in structure or symmetry.

The negative θ values for each sample indicate the presence of significant antiferromagnetic interactions.

A sharp maximum can be seen around the T_N point for V-7 in a plot of susceptibility vs temperature (Fig. 3. 37). This contrasts markedly with its analogue V-9 in which no maxima can be seen, possibly due to the inclusion of a small amount of paramagnetic impurity, evidenced by the sharp upturn at low temperature (Fig. 3. 37). The previously analysed sample of $[NH_4]_2VF_5$-β shows a broad maximum at T_N which compares well to the current sample, no model has been fit to these susceptibility data though, but the two current samples can be modelled fairly well with a Hiesenberg 1D antiferromagnet chain fit (Fig. 3. 37). It is interesting that two analogous samples; $[NH_4]_2VF_5$-β and K_2VF_5, behave very differently magnetically. Each compound displays corner-sharing zig-zag chains

of VF_6 octahedral units. The main difference between the samples is the counter-cation, K^+ in V-9 and NH_4^+ in V-7. The mediation effects of the cations may have something to do with the differences in the magnetic behaviours of each sample, but it is also likely to do with sample impurities.

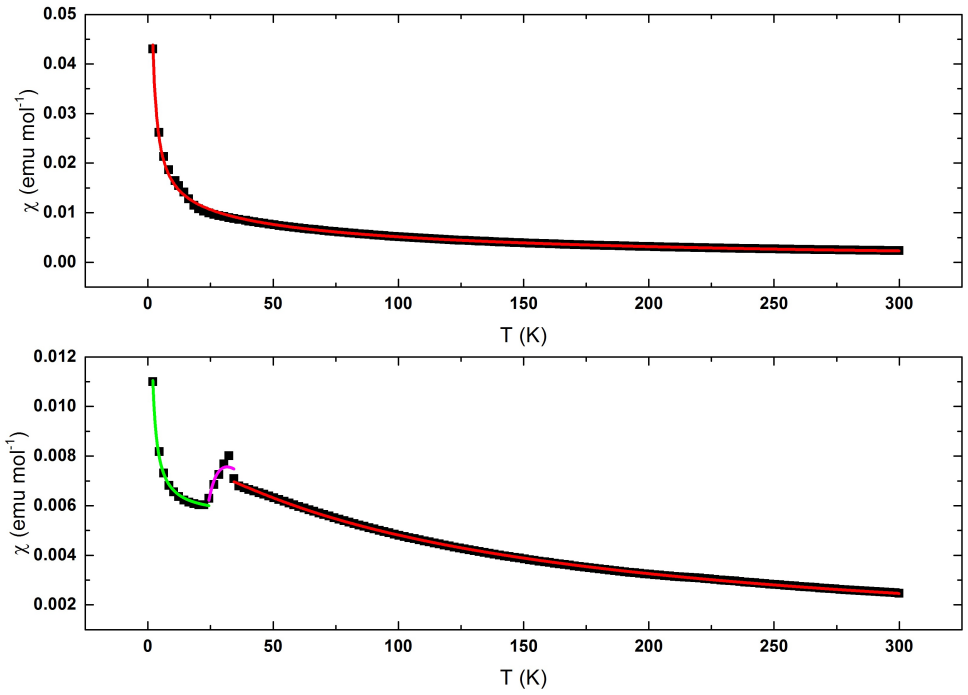

Fig. 3. 37: Susceptibility vs Temperature plots for K_2VF_5 (V-9) (top) and $[NH_4]_2VF_5$-β (V-7) (bottom). K_2VF_5 was fitted with a Bleaney-Bowers antiferromagnet chain model with an added Curie-Weiss term to account for the paramagnetic impurities. $[NH_4]_2VF_5$-β was fitted with a Bleaney-Bowers antiferromagnet model without a Curie-Weiss term since the sample has a definite transition. V-7 (bottom) has been split into three separate sections to highlight the sharp maxima at T_N (purple line).

In K_2VF_5, where K^+ is the counter-cation, the inter-chain V – V distances are slightly shorter than the V – V inter-chain distances in $[NH_4]_2VF_5$-β, where NH_4^+ is the counter-cation (Fig. 3. 38). This is due to the hydrogen bonding present in $[NH_4]_2VF_5$-β which elongates the inter-chain V – V distances by 0.13 Å. All N – F and K – F distances are given in Table 3. 21 for comparison. The magnetic exchange pathways in each sample are via V – F – V bonds, with the $[NH_4]_2VF_5$-β

sample having slightly longer V – F – V distances. A full list of V – V distances is given in Table 3. 22. The difference between the shorter inter-chain and intra-chain V – V distances in V-7 is 1.71 Å.

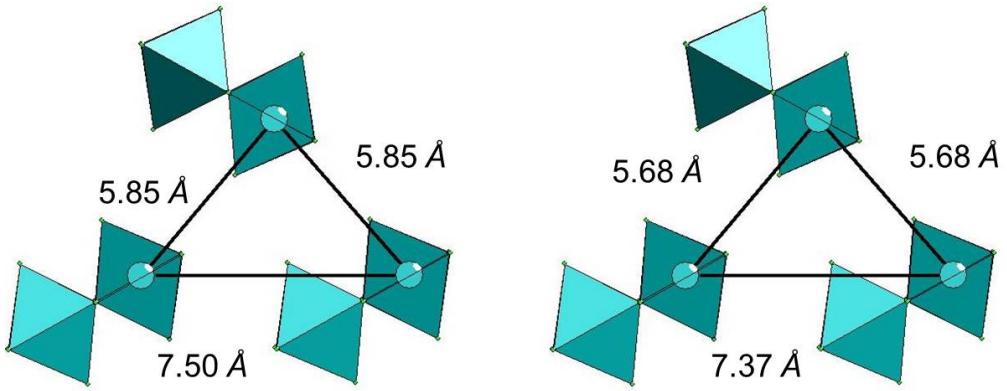

Fig. 3. 38: The inter-chain V – V distances in $[NH_4]_2VF_5$-β (V-7) (left) and K_2VF_5 (V-9) (right).

Table 3. 21: Inter-chain and intra-chain V – V distances for V-7 and V-9.

Compound	Inter-chain V – V distance (Å)	Intra-chain V – V distance (Å)
$[NH_4]_2VF_5$-β (V-7)	5.85(3)	4.14(2)
	7.50(2)	
K_2VF_5 (V-9)	5.68(3)	4.06(2)
	7.32(5)	

It can be seen that the N – F bonds are generally longer than the K – F bonds, which explains why the V – V distances between the chains are longer in V-7 than V-9. It is unlikely that this difference contributes to the difference seen in magnetic behaviour and that it is simply caused by an impurity in V-7.

Table 3. 22: Selected A – F bond lengths for V-7 and V-9 where A = K or N.

$[NH_4]_2VF_5$-β (V-7)	K_2VF_5 (V-9)
N1 – F2 2.818(7)	**K1** – F3 2.691(4)
F3 x2 2.887(9)	F2 x2 2.739(1)
F2 2.914(6)	F2 x2 2.857(4)
F4 x2 2.973(4)	F4 x2 2.871(4)
F4 x2 3.077(3)	F3 2.991(8)
F1 x2 3.099(3)	F1 x2 3.049(5)
N2 – F3 2.807(1)	**K2** – F4 2.617(2)
F4 x2 2.883(8)	F4 2.660(2)
F2 x2 2.885(6)	F2 x2 2.746(6)
F3 2.982(8)	F3 x2 2.854(6)
F4 x2 2.989(2)	F1 x2 2.973(3)
F1 x2 3.052(3)	F2 x2 2.991(4)

3.3 Conclusions

Temperature has a very large effect on the outcome of the reactions discussed in this chapter. The pressures generated inside an autoclave by elevated temperatures can lead to the condensation of structures, with the heat increasing the reactivity of the starting materials. Not only can the temperature affect the oxidation state of the product, but also the crystallite size and morphology. On a more in depth level it can also influence how the building units of each crystal structure condense and pack, giving several crystalline distinct phases of the same structure type.

All six $AVOF_3$ compounds synthesised in this work display distinct crystaline phases of the same structure type. These crystalline phases are influenced by temperature, with the $AVOF_3$-α ($A = K^+$ and Rb^+) compounds forming at 100 ^oC and the $AVOF_3$-β compounds forming at 160 ^oC. Cation size also has a direct effect on the outcome of the products. When all six compounds are compared, it is found that only K^+ and Rb^+ cations allow for any polymorphs to form, the larger size of Cs^+ and NH_4^+ do not allow the compounds to display distinct crystalline phases even when synthesised at lower or higher temperatures.

There appears to be no difference in terms of structural dimensionality of the products between carrying out these types of experiments in the traditional hydrothermal/solvothermal manner or using an ionic liquid in place of the conventional solvents. The reaction outcome was generally the same, either chains or ladder compounds were obtained. A table of reactions, detailing all synthetic procedures that led to the compounds discussed in this chapter is given in the supplementary information. The only real difference was the yield and purity. Products obtained from ionothermal reactions tendd to be of a hger phase purity than those produced from traditional hydrothermal methods.

In the traditional solvothermal and hydrothermal reaction, solvent choice plays

an important role in crystallisation and phase purity. It was generally found that when water alone was used (in quantities of 3-4 mL) that no product was crystallised. However, when ethylene glycol was added to the solvent mixture (in ratios of 3:1, 2:1 or 1:1 water:glycol), crystallisation was more favourable., and phase purity was reasonably high. When the glycol levels started to exceed the water levels used, crystallisation still occurred, but phase purity was greatly reduced as large quantities of black powder formed along with the crystalline phase. It was also found that when ethylene glycol was used on its own that crystallisation was not favourable, and generally black powders were recovered after the eperiments. In the case of dimethyl sulfoxide (DMSO), another polar solvent, the effects were similar to that of water:ethylene glycol mixtures. DMSO on its own generally produced only a coloured liquid and crystallisation was not favourable, but upon mixing with water crystallisation of products was greatly improved. Several examples of reactions and products can be found in excel tables in the supplementary information.

In the case of the A_2VF_5 ($A = K^+$ or NH_4^+) temperature has a different effect on the reaction outcome – the condensation of the chains. $[NH_4]_2VF_5$-α, synthesised at 130 ^oC, displays a linear chain comprised of corner sharing VF_6 octahedral units. As the temperature is increased to 160 ^oC, $[NH_4]_2VF_5$-β is synthesised, displaying a more condensed zig-zag chain of corner sharing VF_6 octahedral units. K_2VF_5, synthesised at 200 ^oC, also displays this condensed, zig-zag, chain, although more experiments are required to see if at lower temperatures a linear polymorph can be obtained.

All compounds discussed display antiferromagnetic behaviour, based on the same 1D Hiesenberg model, showing no apparant sign of ordering, apart from V-7 which has a T_N around 25 K. This ordering of V-7 is likely due to an impurity present as the reaction yielded green crystals as well as some black powder which may not have been completely separated. These physical properties compare well to the analogous structures already described in the literature. It is worth noting that

all values of θ, C, J and μ_{eff} are extracted from fits to a model and therefor are not necessarily reliable. The aim was to show that the Heisenberg model fit all of the data better than the Bleaney-Bowers model, as shown in the trend of the extracted J values of each compound, indicating that the magnetic interactions are along the V – F – V bonds of the ladder 'leg' in the $AVOF_3$ structures. This was a much simples process for the A_2VF_5 structures as in the single chains there are only a single magnetic pathway along the chains.

3.4 References

1. D. W. Aldous, R. J. Goff, J. P. Attfield and P. LIghtfoot, *Inorg. Chem.*, 2007, **46**, 1277-1282.
2. D. W. Aldous, N. F. Stephens and P. Lightfoot, *Inorg. Chem.*, 2007, **46**, 3996-4001.
3. G. M. Sheldrick, 1997.
4. D. W. Aldous, N. F. Stephens and P. Lightfoot, *Dalton Trans.*, 2007, 2271-2282.
5. T. Chirayil, P. Zavalij and M. Whittingham, *Chem. Mater.*, 1998, **10**, 2629-2640.
6. R. Finn, J. Zubieta and R. Haushalter, *Prog. Inorg. Chem.*, 2003, **51**, 421-601.
7. F. H. Aidoudi, D. W. Aldous, R. J. Goff, A. M. Z. Slawin, J. P. Attfield, R. E. Morris and P. Lightfoot, *Nature Chem.*, 2011, **3**, 801-806.
8. F. Himeur, P. K. Allen, S. J. Teat, R. J. Goff, R. E. Morris and P. Lightfoot, *Dalton Trans.*, 2010, **39**.
9. R. E. Morris, *Chem. Comm.*, 2009, 2990-2998.
10. E. R. Parnham, E. A. Drylie, P. S. Wheatley, A. M. Z. Slawin and R. E. Morris, *Angew. Chem. Int. Ed.*, 2006, **45**, 4962-4966.
11. E. R. Cooper, C. D. Andrews, P. S. Wheatley, P. B. Webb, P. Wormald and R. E. Morris, *Nature*, 2004, **430**, 1012-1016.
12. L. Clark, J. C. Orain, F. Bert, M. A. De Vries, F. H. Aidoudi, R. E. Morris, P. Lightfoot, J. S. Lord, M. T. F. Telling, P. Bonville, J. P. Attfield, P. Mendels and A. Harrison, *Phys. Rev. L.*, 2013, **110**, 207208-207201 - 207208-207205.
13. G. Pausewang, *Z. Anorg. Allg. Chem.*, 1971, **381**, 189-197.
14. R. Stomberg, *Acta Chem Scand Ser*, 1986, **40**.
15. K. Waltersson, *J. Solid State Chem.*, 1979, **29**, 195-204.
16. M. Leimkuhler and R. Matters, *J. Solid State Chem.*, 1986, **65**, 260-264.
17. K. Waltersson, *Cryst. Struct. Comm.*, 1978, **7**, 507-511.
18. N. Buchholz, M. Leimkuhler, L. Kiriazis and R. Mattes, *Inorg. Chem.*, 1988, **27**, 2035-2039.

19. P. Bukovec, S. Milicev, A. Demsar and L. Golic, *J. Chem. Soc., Dalton Trans.*, 1981, 1802-1806.
20. M. HIlbers, M. Leimkuhler and R. Mattes, *Z. Natur., B: Chem. Sci.*, 1989, **44**, 383-388.
21. M. P. Crosnier-Lopez, H. Duroy and J. L. Fourquet, *Z. Anorg. Allg. Chem.*, 1993, **619**, 1597-1602.
22. A. Muller, R. Rohlfing, A. L. Barra and D. Gatteschi, *Adv. Mater*, 1993, **5**, 915-917.
23. C. Ninclaus, D. Riou and G. Ferey, *Chem. Comm.*, 1997, 851-852.
24. D. W. Aldous, N. F. Stephens and P. Lightfoot, *Dalton Trans.*, 2007, 4207-4213.
25. H. J. Koo, M. H. Whangbo, P. D. VerNooy, C. C. Torardi and W. J. Marshall, *J. Inorg. Chem.*, 2002, **41**, 4664.
26. D. C. Johnston, J. W. Johnson, D. P. Goshorn and A. Jacobson, *J. Phys. Rev. B*, 1987, **35**, 219.
27. W. Oullette, M. H. Yu, O. C. C.J and J. Zubieta, *Inorg. Chem.*, 2006, **45**, 7628-7641.
28. G. Ferey, *J. Fluorine Chem.*, 1995, **72**, 187-193.
29. K. Adil, M. Leblanc, V. Maisonneuve and P. Lightfoot, *Dalton Trans.*, 2010, **39**, 5983-5993.
30. H. Lijie, Y. Hongming, H. Keke, Y. Chen, L. Guanghua, H. Qiaoru, Y. Yang and F. Shouhua, *J. Solid State Chem.*, 2009, **182**, 2208-2212.
31. R. von der Muehll, S. Andersson and J. Galy, *Acta Cryst. B*, 1971, **27**, 2345-2353.
32. J. Graulich and D. Babel, *Z. Anorg. Allg. Chem.*, 2003, **629**, 1223-1228.

4.0 Copper selenite $S = ½$ pseudo-kagome compounds

The crystal structures of two new compounds, $Cu_3Y(SeO_3)_2O_2Cl$ and $Cu_3La(SeO_3)_2O_2Cl$, based on a related material, $Cu_3Bi(SeO_3)_2O_2Br$[1], will be discussed in this chapter. They have been given the identifiers Cu-1 and Cu-2 respectively. Both compounds are magnetically active, adopting a d^9 $S = ½$ electronic configuration. The structural and magnetic behaviour of both compounds have been analysed via powder diffraction and neutron diffraction.

Powder diffraction experiments were performed on a STOE Stadi P diffractometer equipped with a Ge(111) monochromator (Cu $K_{\alpha 1}$ radiation, 2θ range 10 –115 °), which confirmed phase purity according to the previously suggested structural model obtained from single crystal data.[1, 2]

A study of the magnetic structure was carried out at ISIS neutron facility on the GEM beamline. Data were collected from ambient temperature down to 5 K in regular steps. A structural model was first refined against the data using the Rietveld method in the GSAS[3] and EXPGUI[4] software suites. The magnetic refinements were done in conjunction with GSAS and EXPGUI as well as SARA*h* Representational Analysis,[5] and SARA*h* refine[6] which calculate symmetry-allowed magnetic structures based on the nuclear cell symmetry and the magnetic k-vector. This allows GSAS to refine the magnetic moments of the copper atoms, giving an accurate magnetic model.

4.1 Introduction

This section will discuss the synthesis and characterisation of the structural and physical properties of two new copper (II) selenite pseudo-kagome systems, with comparisons to an analogous structure.

For the last two or three decades, frustrated magnetic systems have been studied and proposed as likely candidates for quantum spin liquids (QSLs), due to their large ground state degeneracy.[7] The large ground state degeneracy introduced by magnetic frustration can induce a large variety of magnetic behaviours depending on other details of the specific system.[7] An important requirement for a material to qualify as a QSL is quantum magnetism ($S = ½$). Much recent work in the area of QSLs has focused on herbertsmithite, $Cu_3Zn(OH)_6Cl_2$, which shows no long range magnetic order down to 50 mK despite its strong antiferromagnetic interactions (suggested by the large negative θ).[8, 9] It has been proposed that $Zn_xCu_{4-x}(OH)_6Cl_2$ would be an ideal candidate for the $S = ½$ kagome system, where antiferromagnetically interacting spins form a two-dimensional network of corner-sharing triangles. It has been shown that, for $x = 0$, $Cu_4(OH)_6Cl_2$, the kagome layers are weakly coupled via octahedral coordinated Cu^{2+} at the triangular sites located in between the Cu^{2+} kagome layers. It was proposed that if Zn^{2+} ions replaced the Cu^{2+} ions at the inter-layer sites only, leaving Cu^{2+} at the kagome sites then $ZnCu_3(OH)_6Cl_2$ (Fig. 4. 1) would be the perfect two-dimensional QSL kagome system. However, neutron diffraction has shown that the inter-layer sites are 36% occupied by the Cu^{2+} and 64% occupied by the Zn^{2+} and the kagome sites are 90% occupied by Cu^{2+} and 10% by Zn^{2+}.[10] $Cs_2ZrCu_3F_{12}$, is another example of a Cu^{2+} d^9 $S = ½$ kagome system.[11, 12] The single crystal diffraction data show that, at room temperature, the compound forms two-dimensional copper-fluoride kagome sheets, which extend in the *ab*-plane, these sheets are linked in the *c*-direction by ZrF_6 octahedral units; Cs^+ ions occupy the large open spaces in the structure (Fig. 4. 2). Variable-temperature synchrotron powder diffraction experiments show that a first order phase transition occurs near 225 K, where the structure

transforms from rhombohedral ($R\bar{3}m$) to monoclinic ($P2_1/m$). The kagome plane becomes buckled during this transition, and it is thought that this phase transition is responsible for the long range antiferromagnetic order in $Cs_2ZrCu_3F_{12}$.[11]

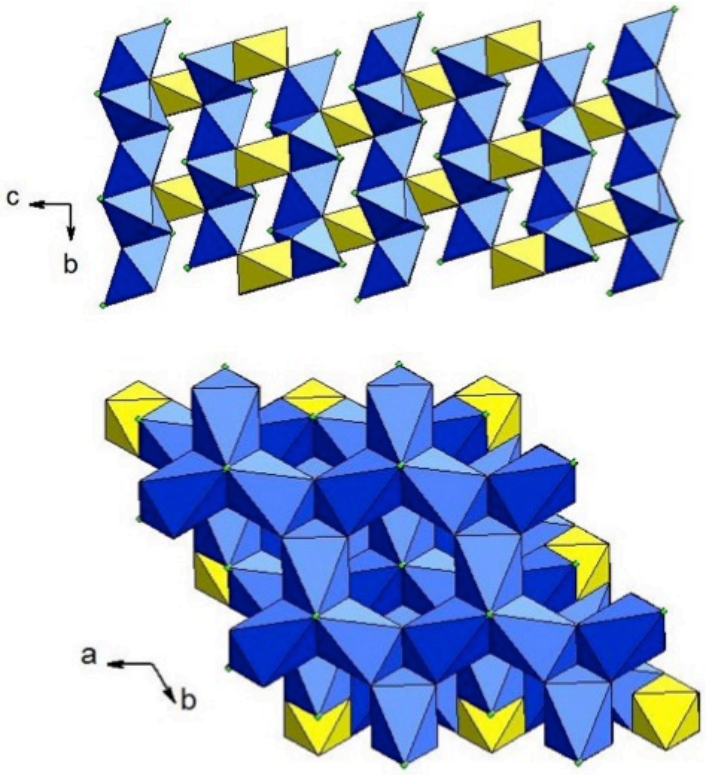

Fig. 4. 1: The copper kagome layers connected via the zinc octahedral units (top) and the copper kagome layers viewed down axis *c* (bottom) of the $ZnCu_3(OH)_6Cl_2$ strucutre. Copper units are blue and zinc units are yellow.

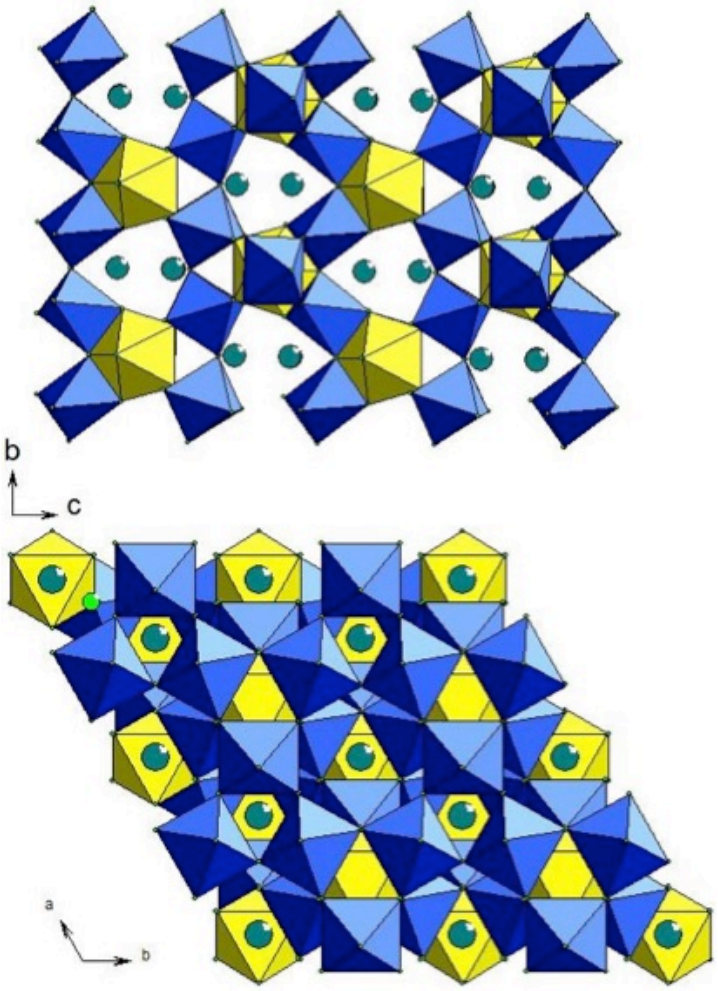

Fig. 4. 2: The monoclinic (top) and rhombohedral (bottom) phases of $Cs_2ZrCu_3F_{12}$ viewed down the layers of the kagome plane. Copper fluoride octahedral units are in blue, zirconium fluoride octahedral units are in yellow and Cs^+ cations are in dark green.

4.2 Synthesis

We would like to thank Dr. Peter Berdonosov of Moscow State University for the preparation of samples Cu-1 and Cu-2. Cu-1 and Cu-2 were prepared from a stoichiometric mixture of high purity Y_2O_3 (Cu-1), La_2O_3 (Cu-2), CuO, $CuCl_2$ and SeO_2. All preparatory procedures with SeO_2 were carried out in an argon filled glove box. The stoichiometric reactant mixture was thoroughly ground with an agate pestle and mortar and transferred into quartz tube which was sealed under vacuum and placed into a tube furnace. The mixture was heated to 300 °C at 0.4 ^oC min^{-1} and held at this temperature for 24 hours. The temperature was then raised to 575 °C at 0.4 ^oC min^{-1} and maintained at this temperature for a further 72 hours. These reactions produced a green-coloured powder indicating a copper (II) oxidation state.

Once cooled the quartz tubes were cut using a band saw and the samples were X-rayed to check for purity before being resealed in new evacuated quartz tubes to be stored for neutron diffraction experiments.

The SeO_2 was obtained from selenous acid (H_2SeO_3) , which was dehydrated under a vacuum at a moderate temperature and then sublimed in a flowing mixture of dry air and NO_2 prepared by thermal decomposition of $Pb(NO_3)_2$.

4.3 Structural characterisation

At room temperature, the network of copper atoms in $Cu_3Y(SeO_3)_2O_2Cl$ (Cu-1) forms a buckled kagome lattice, with layers stacked in the direction of the *c* axis (Fig. 4. 3). The buckling of the layer can be viewed along axis *a* and *b* (Fig. 4. 4), showing how different it is from an ideal kagome network.

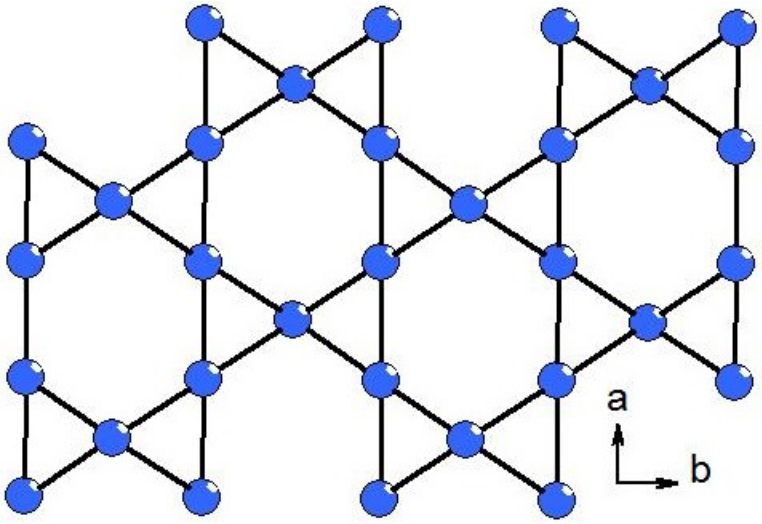

Fig. 4. 3: The network of copper atoms in Cu-1 viewed along axis *c* showing the kagome layer.

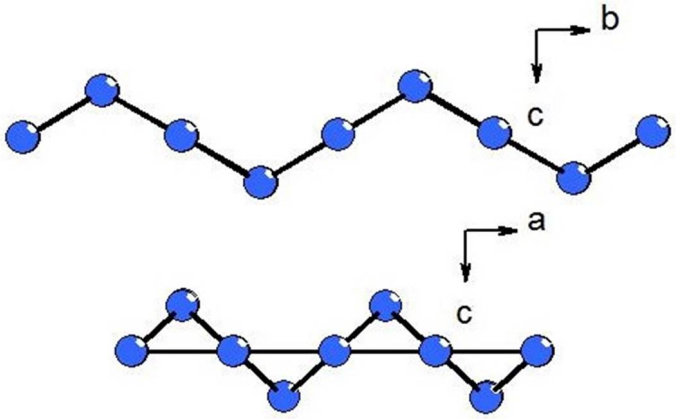

Fig. 4. 4: Buckling of the kagome layer in Cu-1, as viewed along axis *a* (top) and axis *b* (bottom).

There appears to be no evidence for a structural phase transition between the high temperature (280 K) and low temperature (5 K) runs based on the powder neutron diffraction patterns (Fig. 5. 5). Diffraction patterns were collected at intervals from 280 K to 5 K at 40 μA per run. The exact experimental set up for each sample is presented in Table 4. 1. Refinements were carried out on the low-angle and high-resolution data banks in GSAS using the least-squares method with 78 variables refined.

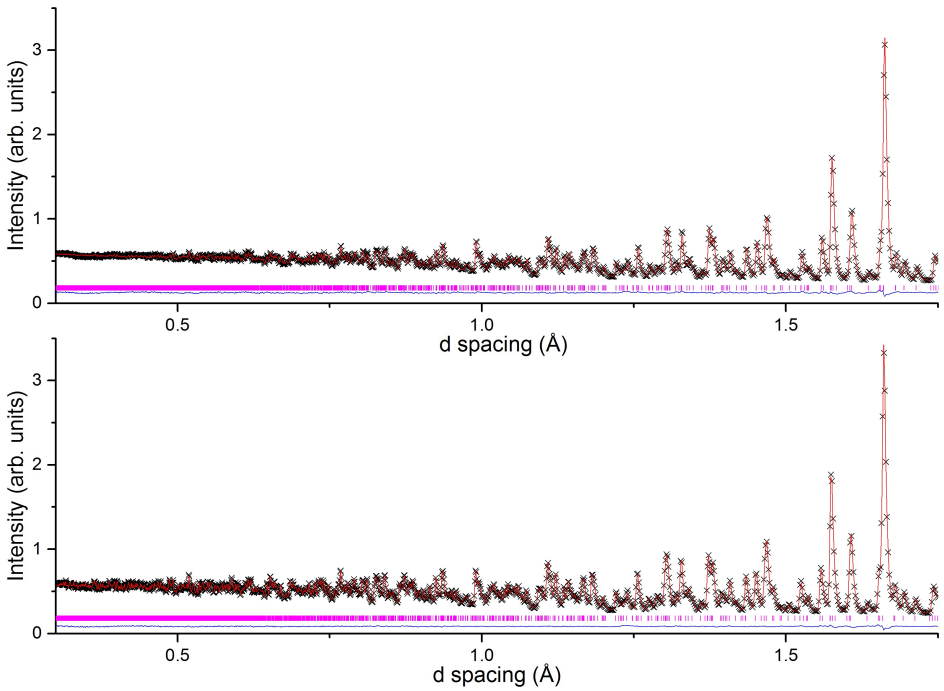

Fig. 4. 5: The high resolution bank from GEM neutron diffraction experiment for $Cu_3Y(SeO_3)_2O_2Cl$. The high temperature (280 K) data refinement (top) and the low temperature (5 K) data refinement (bottom) showing no structural phase transition. The black crosses are the experimental pattern, the red line is the model fit, and the blue line is the difference curve, the phase ticks are shown in pink.

Table 4. 1 Data collection temperatures for the neutron diffraction of Cu-1 and Cu-2.

Cu-1 $Cu_3Y(SeO_3)_2O_2Cl$	Cu-2 $Cu_3La(SeO_3)_2O_2Cl$
5 K	2.5 K
10 K	10 K
20 K	20 K
27 K	27 K
30 K	30 K
33 K	33 K
35 K (T_N)	35 K
40 K	**40 K (T_N)**
45 K	45 K
60 K	50 K
80 K	60 K
100 K	80 K
120 K	100 K
200 K	200 K
280 K	280 K

The full structure is comprised of the kagome network of copper atoms connected via oxygen atoms in a square planar array, and capped by SeO_3 trigonal units. The Y^{2+} cations and Cl^- anions occupy the interstitial sites in the structure. There are two crystallographically distinct copper sites in the kagome layer, Cu1 and Cu2 (which has half the multiplicity of Cu1) (Fig. 4. 6), a list of refined coordinates for the RT and 5 K runs is given in Table 4. 2 and Table 4. 3 respectively. The Cu1 sites all occupy the same plane in the layer while the Cu2 sites sit 'below' the Cu1 sites when viewed along axis *b* giving the layer its buckled nature (Fig. 4. 7).

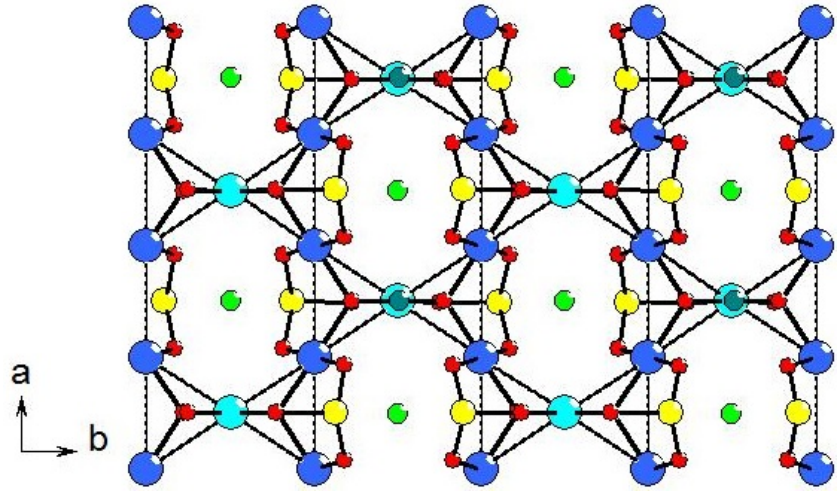

Fig. 4. 6: The full kagome network of $Cu_3Y(SeO_3)_2O_2Cl$ showing the two crystallographically unique copper sites. The Cu – Cu bonds are shown in dotted lines. Cu1 is in blue, Cu2 is in light blue, Y is dark green, Se is yellow, Cl light green and O red. The structure is viewed down axis *c*.

Table 4. 2 Refined atomic coordinates for Cu-1 at 280 K.

Atom site	*x*	*y*	*z*	Uiso
Y	0.25000	0.25000	0.26589(7)	0.00577(6)
Cu1	0.00000	0.00000	0.00000	0.00940(4)
Cu2	0.25000	0.25000	0.79564(5)	0.00536(6)
Se	0.25000	0.56057(6)	0.58989(5)	0.00415(5)
Cl	0.25000	0.75000	0.14651(3)	0.02209(6)
O1	0.25000	0.11055(5)	0.99668(7)	0.00443(4)
O2	0.03961(2)	0.58797(5)	0.73737(6)	0.00772(4)
O3	0.25000	0.11914(7)	0.57488(4)	0.00759(5)

Table 4. 3 Refined atomic coordinates for Cu-1 at 5 K.

Atom site	*x*	*y*	*z*	Uiso
Y	0.25000	0.25000	0.26625(4)	0.00228(6)
Cu1	0.00000	0.00000	0.00000	0.00187(6)
Cu2	0.25000	0.25000	0.79505(4)	0.00187(5)
Se	0.25000	0.56036(6)	0.59963(3)	0.00112(4)
Cl	0.25000	0.75000	0.14414(3)	0.00579(7)
O1	0.25000	0.11072(3)	0.99635(6)	0.00181(5)
O2	0.03930(3)	0.58775(5)	0.73711(3)	0.00243(4)
O3	0.25000	0.11914(5)	0.57448(7)	0.00283(4)

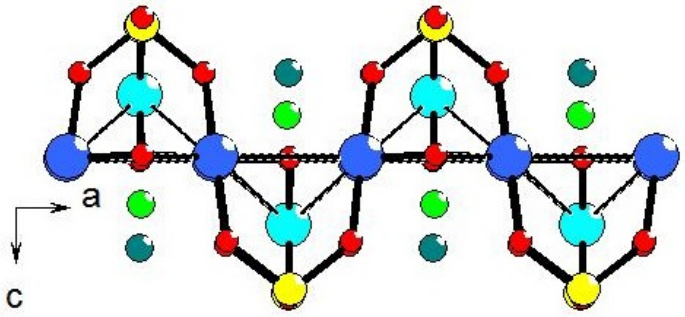

Fig. 4. 7: The kagome layer viewed along axis *b* showing the buckling effect from the two crystallographically distinct copper sites.

$Cu_3Y(SeO_3)_2O_2Cl$ is crystallographically isostructural to $Cu_3La(SeO_3)_2O_2Cl$. Both possess a buckled kagome layer with two distinct copper sites, capped by the SeO_3 trigonal units. The main difference between the two compounds is that the lanthanum sample has a larger unit cell volume than the yttrium sample due to the larger ionic radius of lanthanum. Unit cell parameters for both samples are given in Table 4. 4. A list of refined coordinates for $Cu_3La(SeO_3)_2O_2Cl$ at 280 K and 2.5 K are given in Table 4. 5 and Table 4. 6 respectively.

Both compounds show a decrease in unit cell size upon cooling from 280 K to 5 K. There are some small variations in the unit cell parameters at low temperatures, but these remain within the calculated errors of the refinements (Fig. 4. 8). It seems that the anomalous changes in the axis *a* at low temperatures in the lanthanum sample are of a magnitude that could constitute a real effect, and there have been examples in the literature where a negative thermal expansion has been present in materials.[13]

Cu-2 also does not show any structural phase changes on cooling from 280 K to 5 K, as can be seen from the refinements of the high resolution powder neutron diffraction data (Fig. 4. 9).

These observations are supported by existing structures which are analogous to those reported here, $Cu_3Bi(SeO_3)_2O_2Br$[1, 2], which also does not undergo a structural phase change upon cooling from RT to 5 K.

Table 4. 4: The unit cell parameters for Cu-1 and Cu-2 at 5 K.

Compound	Cu-1	Cu-2
Formula	$Cu_3Y(SeO_3)_2O_2Cl$	$Cu_3La(SeO_3)_2O_2Cl$
Space group	*Pmmn*	*Pmmn*
a (Å)	6.29291(6)	6.39525(4)
b (Å)	9.47362(9)	9.72544(7)
c (Å)	6.96496(6)	7.14895(5)
α (°)	90	90
β (°)	90	90
γ (°)	90	90
V (Å^3)	413.57(2)	444.63(2)

Table 4. 5 Refined atomic coordinates for Cu-2 at 280 K.

Atom site	*x*	*y*	*y*	Uiso
La	0.25000	0.25000	0.26694(4)	0.00553(3)
Cu1	0.00000	0.00000	0.00000	0.00858(3)
Cu2	0.25000	0.25000	0.79913(6)	0.00707(8)
Se	0.25000	0.59986(7)	0.59986(7)	0.00514(5)
Cl	0.25000	0.75000	0.14309(3)	0.02655(6)
O1	0.25000	0.10750(6)	0.98938(8)	0.00312(6)
O2	0.04232(9)	0.58065(8)	0.74295(4)	0.00943(8)
O3	0.25000	0.12175(4)	0.58499(8)	0.01067(9)

Table 4. 6 Refined atomic coordinates for Cu-2 at 2.5 K.

Atom Site	*x*	*y*	*y*	Uiso
La	0.25000	0.25000	0.26758(5)	0.00212(2)
Cu1	0.00000	0.00000	0.00000(6)	0.00184(3)
Cu2	0.25000	0.25000	0.79586(5)	0.00184(3)
Se	0.25000	0.56037(4)	0.59953(8)	0.00119(7)
Cl	0.25000	0.75000	0.14229(5)	0.00568(5)
O1	0.25000	0.10750(2)	0.99035(6)	0.00163(4)
O2	0.04339(6)	0.58114(5)	0.74292(6)	0.00240(2)
O3	0.25000	0.12188(7)	0.58482(4)	0.00262(3)

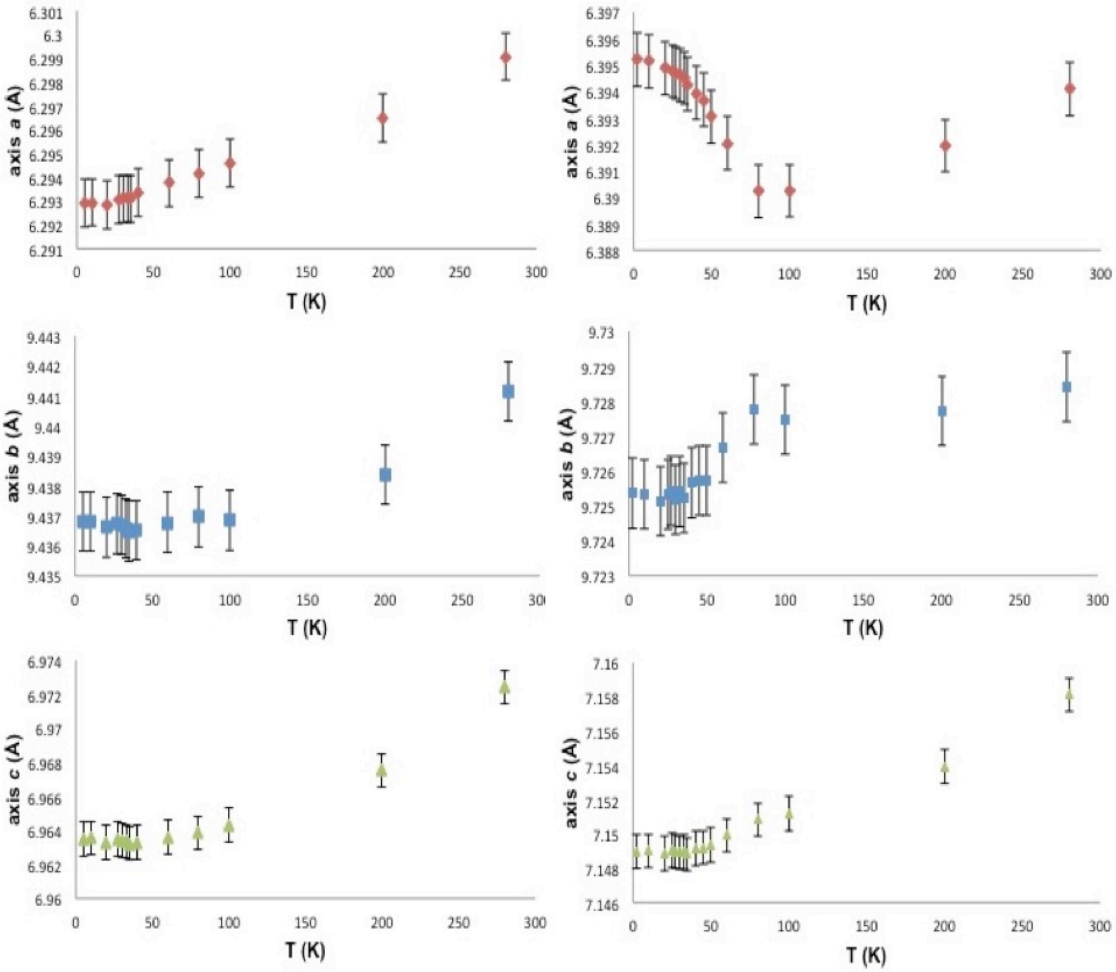

Fig. 4. 8: The unit cell parameters (*a*, *b* and *c*) vs. temperature (K) for $Cu_3Y(SeO_3)_2O_2Cl$ (left) and $Cu_3La(SeO_3)_2O_2Cl$ (right). The *b* and *c* parameters for both compounds follow roughly the same trend while the *a* parameter of the lanthanum sample show negative thermal expansion.

The $Cu_3Bi(SeO_3)_2O_2Br$ compound is isostructural to the yttrium/lanthanum chloride compounds. It crystallises in the orthorhombic space group *Pmmn*, with a slightly larger unit cell volume than both, at 451.39(4) $Å^3$.

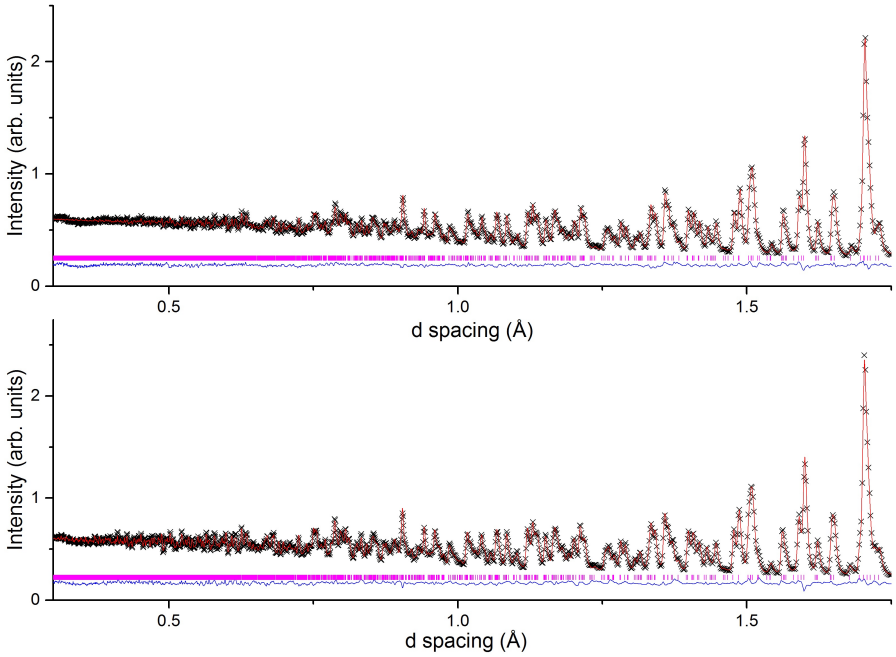

Fig. 4. 9: The high resolution bank from GEM neutron diffraction experiment for $Cu_3La(SeO_3)_2O_2Cl$. The high temperature (280 K) data refinement (top) and the low temperature (5 K) data refinement (bottom) showing no structural phase transition. The black crosses are the experimental pattern, the red line is the model fit, and the blue line is the difference curve, this phase ticks are shown in pink.

The $BiCu_3(SeO_3)_2O_2Br$ bromide sample displays ferromagnetic interactions according to the positive theta value obtained powder susceptibility measurements, as its high temperature behaviour follows a Curie-Weiss law, and orders at around $T_N \approx 24$ K. A neutron diffraction study was also carried out and used to model the magnetic moments of the two copper sites. The following section will discuss the low temperature neutron diffraction study of $Cu_3Y(SeO_3)_2O_2Cl$ and $Cu_3La(SeO_3)_2O_2Cl$ and how they compare to $Cu_3Bi(SeO_3)_2O_2Br$.

4.4 Neutron diffraction study

A low temperature powder neutron diffraction study was carried out on $Cu_3Y(SeO_3)_2O_2Cl$ and $Cu_3La(SeO_3)_2O_2Cl$. Data were collected at regular intervals from room temperature down to 2.5 K (Table 4. 1). Due to time constraints it was not possible to run both samples in exactly the same manner, but a thorough low temperature exploration was carried out. Cu-1 was not run at 2.5 K due to cooling problems so it was decided, in the interest of time and experimental completeness, to allow the temperature to equilibrate at 5 K and run from there. Cu-1 has a T_N around 35 K which is observed in the neutron data as two magnetic peaks occurring around 4.6 and 4.9 Å. The peaks do not change considerably in intensity over the temperature range down to 5 K, and they are not present at all above 35 K. An initial structural refinement was performed on the GSAS program to fit the structural model to the range of temperatures (Fig. 4. 10) before attempts were made to fit the magnetic model. Cu-2 displays an impurity peak in the neutron data which can be observed from RT down to 2.5 K. This does not seem to have an effect on the evolution of the magnetic Bragg peaks, and only manifests as a single peak at around 4 Å in all data sets from high to low temperature. There are, again, two magnetic peaks observed in Cu-2 observed at 4.7 and 5 Å which appear at a T_N of 40 K. The magnetic peaks stay fairly constant in intensity over the temperature range down to 2.5 K, and are not present at all above 40 K. Structural refinements were carried out on the whole temperature range before any magnetic model was used to improve the fits at low temperature.

Since the magnetic reflections occur at positions distinct from the nuclear reflections then it can be assumed that the magnetic ground state is antiferromagnetic. The main magnetic reflections of both compounds at positions; 021, $02\bar{1}$ and; $11\bar{1}$, $1\bar{1}\bar{1}$, $1\bar{1}1$ and 111 were indexed by the magnetic wave vector $k = (0,0,½)$, a doubling of axis *c*. This *c* axis doubling was required in order to successfully fit the magnetic peaks. This irreducible representation for the magnetic structure was chosen based on the previous single crystal and powder

neutron diffraction study of $Cu_3Bi(SeO_3)_2O_2Br$[1] since the structures were analogous, and displayed magnetic reflections in the same positions. Fitting the moments using the conventional colour group method, assigning a 'red' or 'black' to each magnetic atom giving it an 'up' or 'down' orientation, was difficult since there was evidence that the two distinct copper sites would have different magnetic moments. This meant that there would be a lot of trial and error involved and no guarantee that a reliable fit to both peaks could be achieved. It was decided that a representational analysis would be a more appropriate method, as this would provide a limited number of magnetic models based on the propagation wave vector and crystal symmetry that could be fit to the data.[14,] The $Cu_3Y(SeO_3)_2O_2Cl$ sample was fitted well using the model provided by Pregelj.[1] There were several possible symmetry elements that could be used to describe the magnetic behaviour of the compounds in the space group *Pmmn* using the *k*-vector (0, 0, ½) ; these are given in Table 4. 7.

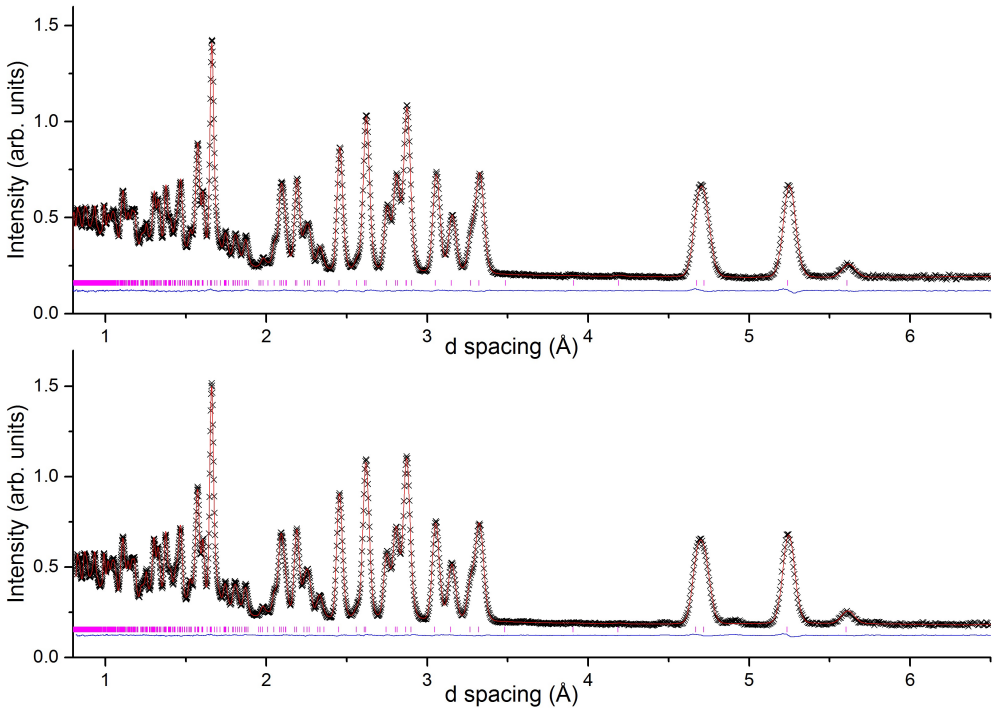

Fig. 4. 10: The 280 K structural refinement (top) and the 35 K structural refinement (bottom) for $Cu_3Y(SeO_3)_2O_2Cl$. Magnetic peaks are clearly visible between 4.7 and 4.9 Å in the 35 K refinement, but have not yet been fitted with the magnetic phase.

Table 4. 7: Irreducible representations for the Cu 1 and Cu 2 sites of the *Pmmn* space group and $k = (0, 0, ½)$ magnetic wave vector.

Site Cu 1	Γ_1	Γ_3	Γ_5	Γ_7
x, y, z	*u, v, w*	*u, v, w*	*u, v, w*	*u, v, w*
$-x+½, -y+½, z$	-*u*, -v, *w*	-*u*, -v, *w*	*u, v*, -*w*	*u, v*, -*w*
-*x*, $y+½$, -*z*	-*u, v*, -*w*	*u*, -*v, w*	-*u, v*, -*w*	*u*, -*v, w*
$x+½$, -*y*, -*z*	*u*, -*v*, -*w*	-*u, v, w*	-*u, v, w*	*u*, -*v*, -*w*

Site Cu 2	Γ_2	Γ_3	Γ_5	Γ_6	Γ_7	Γ_8
x, y, z	0, 0, *u*	0, 0, *u*	0, *u*, 0	*u*, 0, 0	*u*, 0, 0	0, *u*, 0
-*x*, $y+½$, -*z*	0, 0, -*u*	0, 0, *u*	0, *u*, 0	-*u*, 0, 0	*u*, 0, 0	0, -*u*, 0

Using the Cu1 Γ_7 and Cu2 Γ_2 settings generated by SARA*h* provided a good magnetic model to fit the $Cu_3Y(SeO_3)_2O_2Cl$ data with (Fig. 4. 11). The *wRp* values for the refinements dropped significantly with the addition of the magnetic model even though the magnetic reflections are very weak compared to the nuclear reflections. A list of *wRp* values for the nuclear and magnetic refinements for Cu-1 and Cu-2 are given in Table 4. Initial magnetic moments for each copper site were set for Cu1 at; $m_y = 0.72$ μB and $m_z = 0.57$ μB and Cu2 at; $m_z = 0.90$ μB, determined from the $Cu_3Bi(SeO_3)_2O_2Cl$ single crystal data. The moments were allowed to refine during each experiment and were plotted against temperature (Fig. 4. 12). The Cu2 moment shows a steady decrease with respect to temperature, approximately halving in size before disappearing at T_N. The Cu1 moments do not seem to follow this behaviour and stay more or less constant, with some fluctuations until T_N.

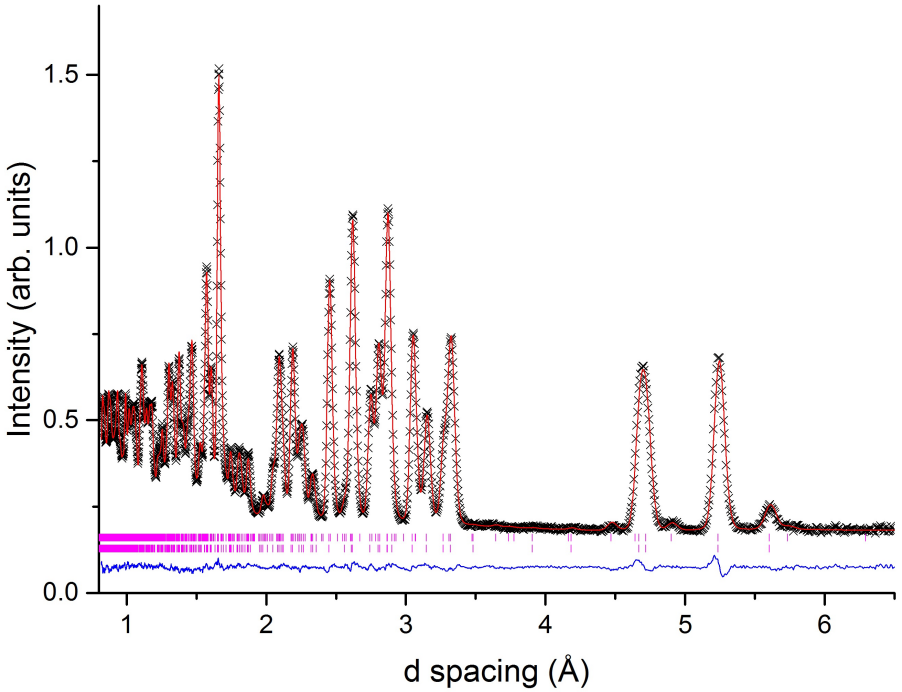

Fig. 4. 11: The 5 K powder neutron diffraction data for $Cu_3Y(SeO_3)_2O_2Cl$ showing the refinement and fit of the magnetic reflections from the low angle bank. The data were fit with the Cu1 Γ_7 and Cu2 Γ_2 settings generated by SARA*h*. The top tick-marks represent the magnetic phase.

Table 4. 8: The *wRp* values for the nuclear and magnetic refinements from the low angle bank for Cu-1 and Cu-2.

$Cu_3Y(SeO_3)_2O_2Cl$	*wRp* low angle bank (nuclear)	*wRp* low angle bank (magnetic)
5 K	0.0214	0.0207
10 K	0.0267	0.0261
20 K	0.0258	0.0254
27 K	0.0261	0.0260
30 K	0.0250	0.0251
33 K	0.0252	0.0255
35 K	0.0259	0.0260
40 K	0.0258	0.0261
280 K	0.0222	n/a
$Cu_3La(SeO_3)_2O_2Cl$	*wRp* low angle bank (nuclear)	*wRp* low angle bank (magnetic)
2.5 K	0.0405	0.0316
10 K	0.0436	0.0354
20 K	0.0430	0.0344
25 K	0.0434	0.0348
27 K	0.0432	0.0342
30 K	0.0434	0.0343
33 K	0.0421	0.0331
35 K	0.0426	0.0332
40 K	0.0418	0.0328
45 K	0.0430	0.0335
280 K	0.0440	n/a

It was determined that the impurity, present at around 4 Å, in Cu-2 would not affect the evolution if the magnetic Bragg peaks, and therefore the sample could be analysed in the same way as Cu-1. The magnetic reflections occur at 4.8 and 5 Å when the temperature drops below 40 K and can easily be seen when compared to the room temperature refinement (Fig. 4. 13). The Cu1 Γ_7 and Cu2 Γ_2 settings generated by SARA*h* were used again for this compound, and this model provided a good fit for the magnetic reflections occurring below 40 K (Fig. 4. 14).

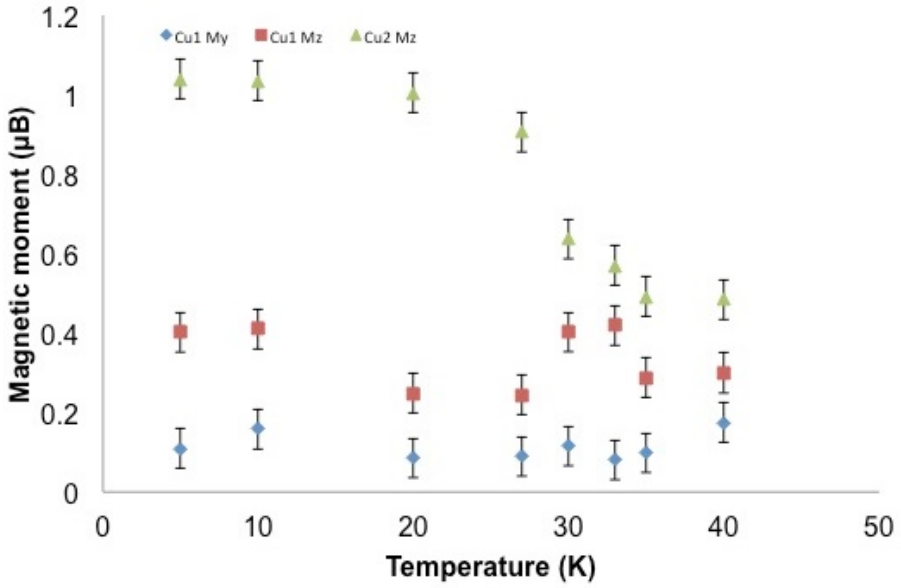

Fig. 4. 12: The magnetic moments (μB) with respect to temperature (K) for the $Cu_3Y(SeO_3)_2O_2Cl$ neutron data.

The Cu1 and Cu2 moments show steady decreases with respect to temperature, approximately halving in size before disappearing at T_N (40 K) (Fig. 4. 15).

Not only do the Cu1 and Cu2 sites on the compounds have different magnetic moments in terms of magnitude, they are also aligned differently throughout the magnetic structure. Cu2 was fit to the data using the Γ_2 setting generated by SARA*h* (0, 0, *u*) and (0, 0, -*u*) at ~1 μB (based on $Cu_3Bi(SeO_3)_2O_2Cl$). These spins are aligned with axis *c* in a ferromagnetic manner within the kagome layer, but antiferromagnetic between each layer moving along axis *c*. This was very simple to model and visualise as there is only one magnetic moment on m_z for Cu2.

Cu1 was more complex to model as it has moments of two different magnitudes

on m_y and m_z which are not aligned with any axis. The Γ_7 setting generated by SARA*h* (*u*, *v*, *w*) (*u*, *v*, -*w*) (*u*, -*v*, *w*) (*u*, -*v*, -*w*) were used to fit the Cu1 moments.

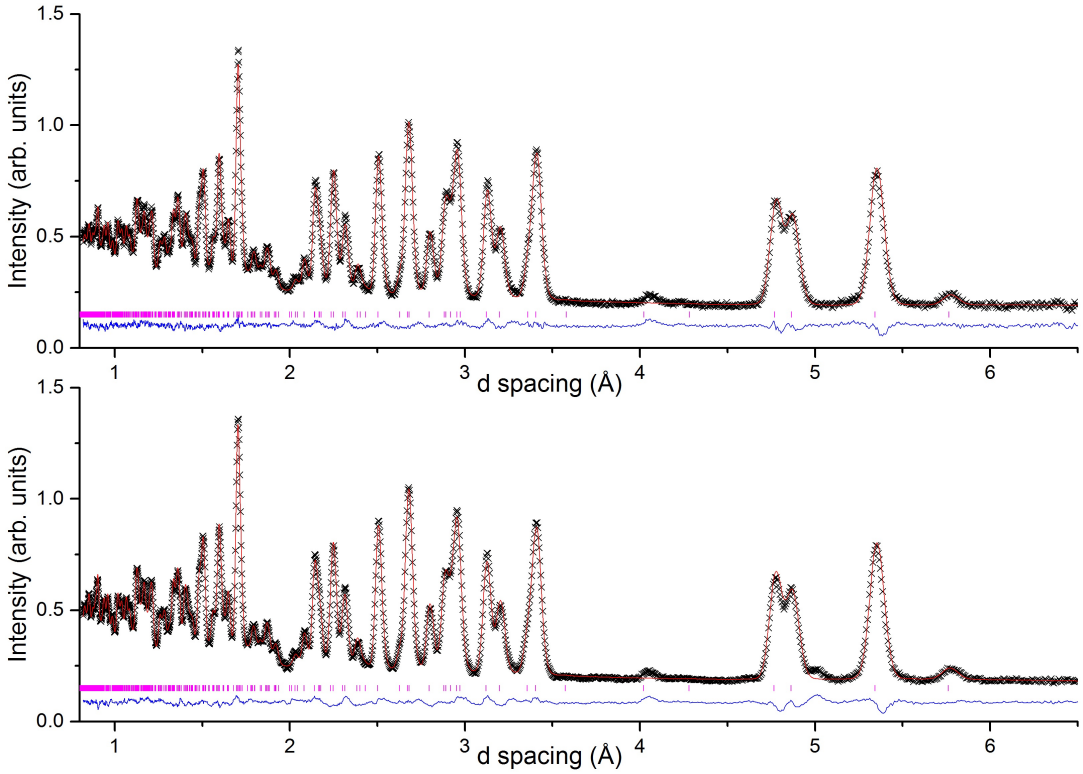

Fig. 4. 13: The 280 K structural refinement (top) and the 40 K structural refinement (bottom) for $Cu_3La(SeO_3)_2O_2Cl$. Magnetic peaks are clearly visible at 4.8 and 5 Å in the 40 K refinement, but have not yet been fitted.

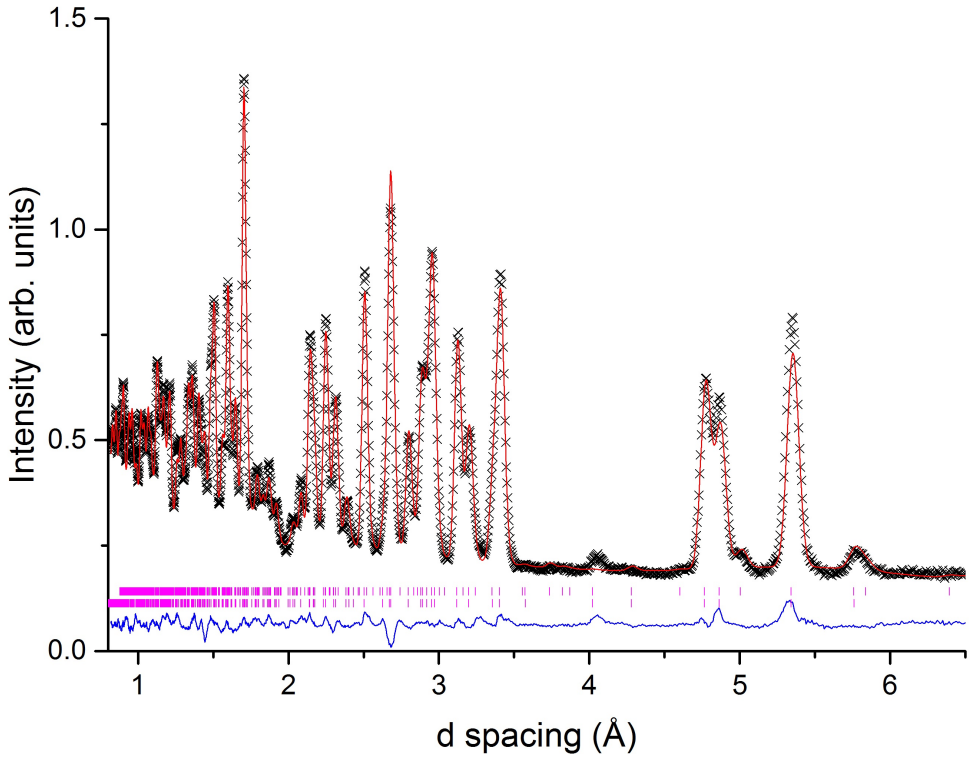

Fig. 4. 14: The 2.5 K powder neutron diffraction data for $Cu_3La(SeO_3)_2O_2Cl$ showing the refinement and fit of the magnetic reflections from the low angle bank. The data were fit with the Cu1 Γ_7 and Cu2 Γ_2 settings generated by SARA*h*. The top tick-marks represent the magnetic phase.

The m_y and m_z moments on Cu1 were set at ~0.7 μB and ~0.55 μB (based on $Cu_3Bi(SeO_3)_2O_2Cl$). The Cu1 moments are aligned in such a way that they are parallel to axis *c* with an additional alternating component along axis *b* and are canted ~ $\pm$ 50 ° from *c* towards *b*. Once again they are aligned ferromagnetically within the kagome layer and antiferromagnetically between the layers.

When Cu1 and Cu2 are combined, it builds up a relatively complicated magnetic structure showing the arrangement of the two different copper sites on the kagome layer, with the magnetic moments aligned differently depending on the representational analysis settings (Fig. 4. 16).

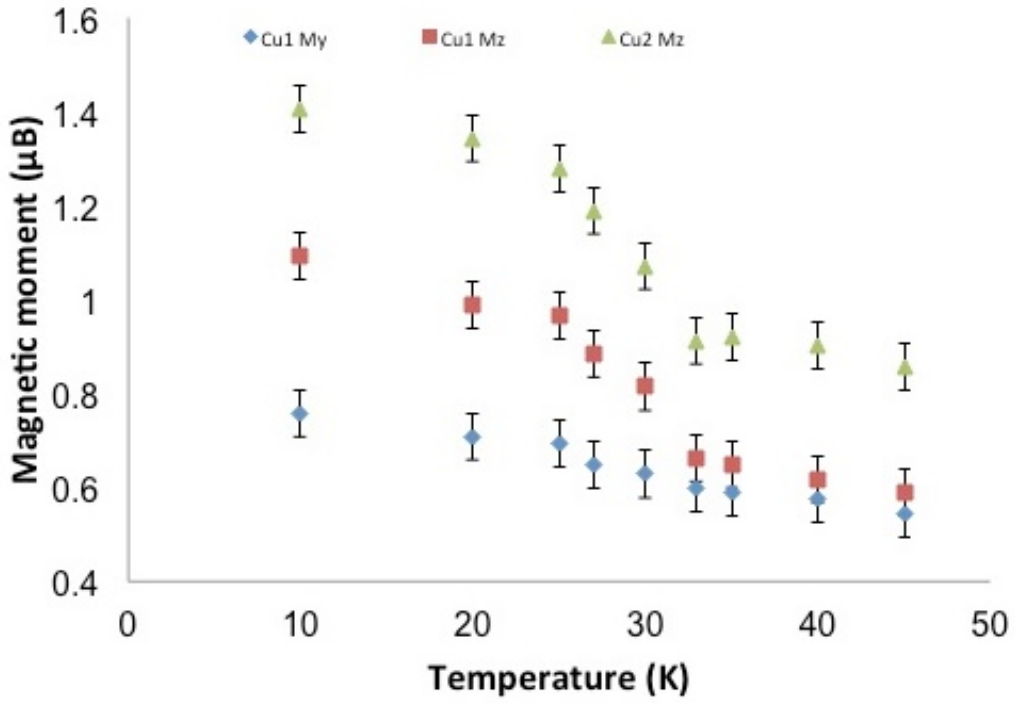

Fig. 4. 15: The magnetic moments (μB) with respect to temperature (K) for the $Cu_3La(SeO_3)_2O_2Cl$ neutron data.

Other models were tried from the list provided by SARA*h*, but none fit as well as the two that were selected. This is due to the complex nature of the magnetic structure having specific magnetic moment vectors, and the spin model would not have been satisfied using other irreducible representations. However, it is worth noting that, had single crystal data been available, it may have been possible to fit another model to the data. The Γ_7 Γ_2 model was chosen because it was used to fit the single crystal neutron data most effectively in the case of the bismuth analogue.

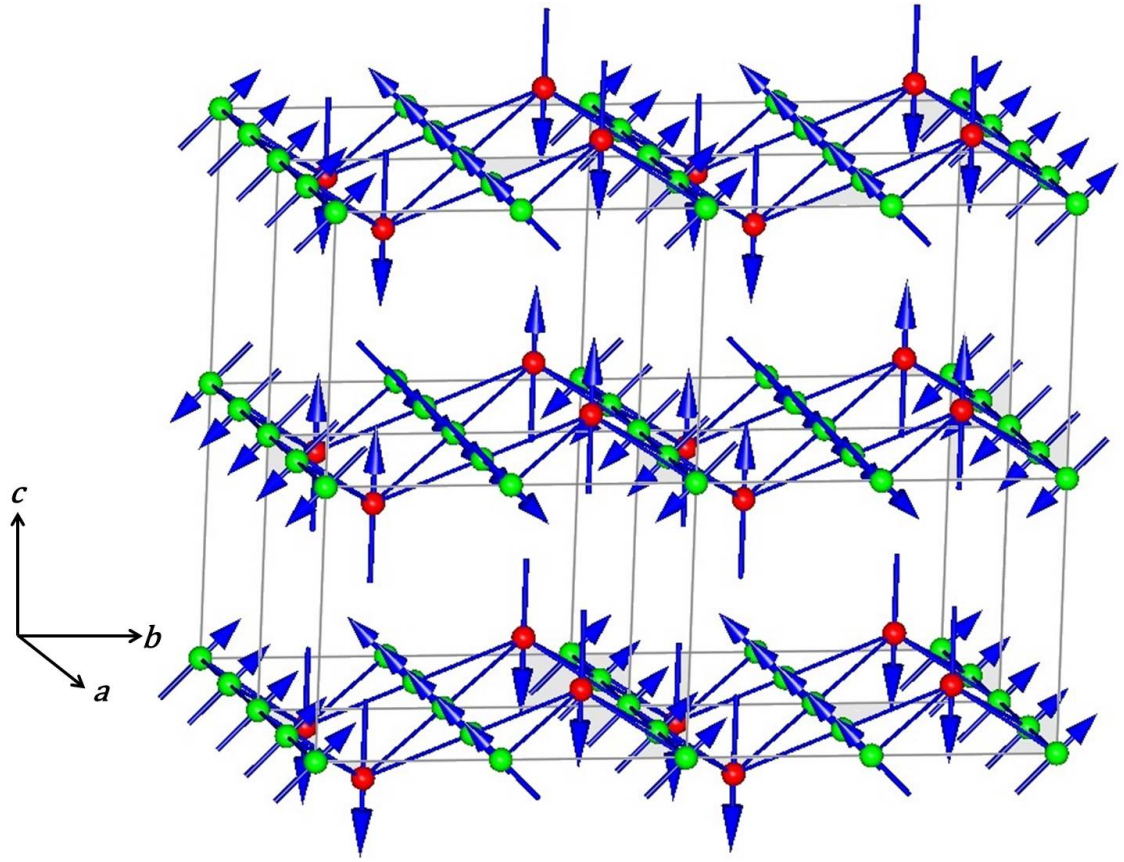

Fig. 4. 16: The magnetic structure of $Cu_3Y(SeO_3)_2O_2Cl$ and $Cu_3La(SeO_3)_2O_2Cl$ showing the different alignments of Cu1 (green) and Cu2 (red). Cu2 (red) is aligned with axis *c* ferromagnetically within the kagome layer, but antiferromagnetically between the layers. Cu1 follows the same ferro/antiferromagnetic alignment and Cu2, but it is canted alternately from axis *c* into axis *b*.

4.5 Conclusions

The pseudo-kagome systems $Cu_3Y(SeO_3)_2O_2Cl$ (Cu-1) and $Cu_3La(SeO_3)_2O_2Cl$ were synthesised via solid state synthesis techniques. Cu-1 was determined to be phase pure by PXRD analysis, while a small impurity was detected in Cu-2. Both samples are analogous to $Cu_3Bi(SeO_3)_2O_2Br$ and were studied, using neutron diffraction, to test for the same kind of magnetic behaviour exhibited by this compound.

The magnetic properties of the layered pseudo-kagome systems $Cu_3Y(SeO_3)_2O_2Cl$ (Cu-1) and $Cu_3La(SeO_3)_2O_2Cl$ (Cu-2) have been studied using powder neutron diffraction and compared to results obtained from an analogous compound $Cu_3Bi(SeO_3)_2O_2Cl$. Upon doubling the *c* axis, to obtain the magnetic unit cell, of both compounds using the *k* vector (0, 0, ½) it was possible to refine the data using the Γ_7 Γ_2 irreducible representations obtained from SARA*h* refine and the analogous $Cu_3Bi(SeO_3)_2O_2Br$ compound.

Both samples were subject to low temperature neutron diffraction studies, and it was found that below $T_N = 35$ K (Cu-1) and $T_N = 40$ K (Cu-2) the magnetic ground state can be described as ferromagnetic individual kagome layers with antiferromagnetic interlayer coupling. The magnetic models were refined using a combination of the single crystal data, obtained from the bismuth analogue, and representational analysis. Moments on Cu2 sites are aligned parallel to axis *c* while those on the Cu1 sites alternate between $\sim \pm 50^{\circ}$ tilt from *c* towards *b*. This is in good agreement with the $Cu_3Bi(SeO_3)_2O_2Cl$ model described by Pregelj[1], which exhibits the same kind of magnetic structure below $T_N = 27.4$ K.

It may be worth trying to grow single crystals of Cu-1 and Cu-2 to perform single crystal neutron diffraction studies. This would yield more accurate data as to the exact magnetic space group and magnetic model of these compounds and may provide a more detailed model of their magnetic behaviour.

4.6 References

1. M. Pregelj, O. Zaharko, A. Gunther, A. Loidl, V. Tsurkan and S. Guerrero, *Phys. Rev. B*, 2012, **86**, 1444091 - 1444097.
2. P. Millet, B. Bastide, V. Pashchenko, S. Gnatchenko, V. Gapon, T. Ksari and A. Stepano, *J. Mater. Chem.*, 2001, **11**, 1157.
3. A. C. Larson and R. B. Von Dreele, *Los Alamos National Lab. Report*, 2000, 86-748.
4. B. H. Toby, *J. Appl. Cryst.*, 2001, **34**, 210-213.
5. A. S. Wills, *Physica B*, 2000, **276**, 680-681.
6. A. S. Wills, *Z Kristallogr Suppl*, 2009, **30**, 39-44.
7. A. Harrison, *J. Phys.: Condens. Matter*, 2004, **16**, 553-572.
8. M. P. Shores, E. A. Nytko, B. M. Bartlett and D. G. Nocera, *J. Am. Chem. Soc.*, 2005, **127**, 13462-13463.
9. M. A. deVries, K. V. Kamenev, W. Kockelmann, J. Sanchez-Benitez and A. Harrison, *Phys. Rev. Lett.*, 2008, **100**, 157205.
10. S. H. Lee, H. Kikuchi, Y. Qiu, B. Lake, Q. Huang, K. Habicht and K. Kiefer, *Nat. Mater.*, 2007, **6**, 853-857.
11. S. A. Reisinger, C. C. Tang, S. P. Thompson, F. D. Morrison and P. Lightfoot, *Chem. Mater.*, 2011, **23**, 4234-4240.
12. M. Muller and B. Muller, *Anorg. Allg. Chem.*, 1995, **621**, 993 - 1000.
13. J. S. O. Evans, T. A. Mary, T. Vogt, M. A. Subramanian and W. A. Sleight, *J. Am. Chem. Soc.*, 1996, **8**, 2809-2823.
14. J. Rodrigues-Carvajal, *Physica B*, 1993, **192**, 55.

5.0 Miscellaneous compounds of vanadium

The crystal structures of seven new vanadium compounds will be discussed in this chapter. They have been given the identifiers V-10 to V-16 in the chronological order in which they were synthesised. Compounds were analysed using single crystal X-ray diffraction and powder X-ray diffraction, as well as CHN microanalysis for hybrid compounds. Magnetic measurements were carried out on V-16. Crystallographic information for all compounds is presented in Table 5. 1, Table 5. 2 and Table 5. 3. Atomic coordinates are given in appendix A, and bond angles are contained in the appropriate CIF.

Single crystals were analysed using a Rigaku SCX-mini desktop diffractometer equipped with graphite monochromated Mo K_α ($\lambda = 0.71075$ Å) radiation. Intensity data were collected via the 'multi-scan' method to remove any false spots. Data were collected at 173 K. All structures were solved by direct methods and refined by full-matrix least-squares cycles in SHELXL-97.[1] Hydrogen atoms were, where possible, located using Fourier techniques and refined isotropically. Generally they were located at geometrically calculated positions and fixed to the atom in question to 'ride' with the refinement.

Powder diffraction experiments were carried out on a PANalytical Empyrean powder diffractometer equipped with monochromated Cu $K_{\alpha 1}$ ($\lambda = 1.5406$ Å) X-rays. The diffractometers are operated in reflection mode with data collected at ambient temperature.

Dr. Lucy Clark collected magnetic data on an MPMS Quantum Design SQUID magnetometer (University of Edinburgh).

CHN analysis was performed using a Carlo Flash 2000 Elemental Analyser and was collected by Stephen Boyer at the London Metropolitan University. Obtained values were compared to theoretical values to test for sample purity.

Table 5. 1: Crystallographic information for V-10 through V-12.

Compound	V-10	V-11	V-12
Formula	$Cs_2V_2O_3(SO_4)_2$	$Rb_2VF_3(SO_4)$	$[H_4TETA]_2[V_{10}O_{28}].4H_2O$
Space group	*Pna2₁*	*Pbcn*	$P\bar{1}$
a/Å	26.267(5)	11.158(5)	8.8292(10)
b/Å	8.272(5)	8.724(4)	11.2556(3)
c/Å	5.068(3)	7.165(3)	11.4808(3)
α/°	90	90	64.530(3)
β/°	90	90	74.120(3)
γ/°	90	90	63.811(2)
V/ Å^3	1101.2(1)	697.5(5)	919.34(11)
Z	4	4	1
GFM	608.82	374.94	1330.02
ρ_{calc} / g cm^{-3}	3.281	3.571	2.402
μ / mm^{-1}	7.835	15.609	2.542
Crystal size (mm)	0.28x0.19x0.13	0.18x0.14x0.11	0.23x0.22x0.17
F(000)	984	688	666
Reflections Collected	6489	3228	5859
Independent Reflections	1974	735	3240
R_{int}	0.0868	0.0498	0.0645
Data/Restraints/Parameters	1573/1/154	646/0/53	2598/14/336
GOF on F^2	1.033	1.123	1.052
R_1, wR_2 [$I > 2\theta(I)$]	0.0762, 0.1824	0.0389, 0.0885	0.0600, 0.1624
R_1, wR_2 (all data)	0.0945, 0.1941	0.0482, 0.0922	0.0734, 0.1741

Table 5. 2: Crystallographic information for V-13 and V-14.

Compound	V-13	V-14
Formula	$[CN_3H_6]_3[VF_6]$	$[CN_3H_6][V_2O_2F_5]$
Space group	$Pa\bar{3}$	$P2_1/c$
a/Å	14.095(3)	7.514(3)
b/Å	14.095(3)	11.753(4)
c/Å	14.095(3)	18.132(6)
α/°	90	90
β/°	90	91.512(11)
γ/°	90	90
V/ Å^3	2800.2(10)	1600.7(1)
Z	4	4
GFM	486.26	577.94
ρ_{calc} / g cm^{-3}	1.153	0.954
μ / mm^{-1}	0.742	1.158
Crystal size	0.08x0.07x0.05	0.25x0.08x0.04
F(000)	1000	448
Reflections Collected	16185	8805
Independent Reflections	853	2762
R_{int}	0.0929	0.1032
Data/Restraints/Parameters	778/0/83	1622/0/46
GOF on F^2	1.319	0.970
R_1, wR_2 [$I > 2\theta(I)$]	0.0455, 0.1372	0.1597, 0.3712
R_1, wR_2 (all data)	0.0575, 0.1607	0.2070, 0.3971

Table 5. 3: Crystallographic information for V-15 and V-16.

Compound	V-15	V-16
Formula	$[V_2O_2F_2(H_2O)_2].H_2O$	$[CN_3H_6]_3[V_2O_2F_7]$
Space group	$C2/c$	$C2/c$
a/Å	14.453(8)	7.460(2)
b/Å	4.8879(19)	12.893(3)
c/Å	9.663(5)	16.686(5)
α/°	90	90
β/°	103.240(2)	100.812(3)
γ/°	90	90
V/ Å^3	664.5(6)	1604.89(17)
Z	4	4
GFM	263.93	447.14
ρ_{calc} / g cm^{-3}	2.638	1.885
μ / mm^{-1}	2.873	1.282
Crystal size	0.06x0.04x0.03	0.12x0.08x0.06
F(000)	512	896
Reflections Collected	3138	7665
Independent Reflections	750	1809
R_{int}	0.0856	0.0844
Data/Restraints/Parameters	585/0/63	1223/0/142
GOF on F^2	1.013	0.945
R_1, wR_2 [$I > 2\theta(I)$]	0.0348, 0.0629	0.0422, 0.0958
R_1, wR_2 (all data)	0.0577, 0.0707	0.0780, 0.1097

5.1 Vanadium miscellaneous structures

This section will discuss the synthesis and characterisation of the structural and physical properties of seven new vanadium-containing compounds, with comparisons to analogous compounds.

The aim was to synthesise new, magnetically active vanadium compounds, attempting to incorporate sulfate, phosphate, or selenium/ tellurium oxyanions to help facilitate an increase in the dimensionality of the structures.

5.1.1 Introduction

Compounds with high dimensionality (2D, 3D) are desirable for the interesting physical properties that they can exhibit in appropriate oxidation states.[2-5] It can often be difficult to achieve the desired dimensionality without the addition of some kind of linker, such as sulfate or selenite groups, to help connect isolated metal polyhedral units to one another. The compounds $(VO)(SeO_3)(H_2O)$[6] and $Li_2V_2(SO_4)_3$[7] each consist of isolated face-sharing vandium-containing dimers, which are connected via the SeO_3 groups into 2D (Fig. 5. 1) and SO_4 groups into 3D (Fig. 5. 2) structures, respectively.

The increased dimensionality can lead to an improvement in, for example, electronic conductivity or redox-potential (for battery applications) due to inductive effects through phosphate or sulfate tetrahedral linkers. It can also lead to more interesting magnetic properties as isolated units become connected, leading to new interaction pathways. Examples of other structures which have increased in dimensionality from the incorporation of linking groups are $[C_6H_{16}N_2][VO(SeO_3)(HSeO_3)]_2$[5], $Li(VO_2)_3(TeO_3)_2$[8] and $LiVOPO_4$[9] along with many others.[5, 10, 11]

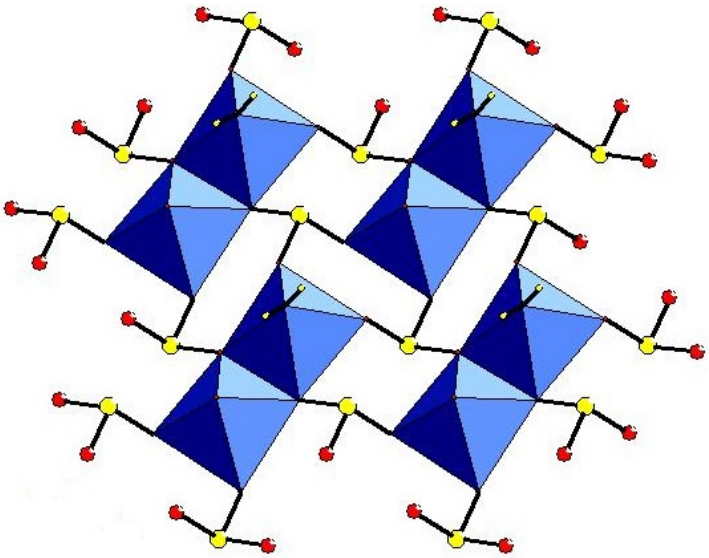

Fig. 5. 1: The hydrated vanadium oxide edge-sharing dimers connected into the 2D structure of $(VO)(SeO_3)(H_2O)$ by the corner-sharing selenite trigonal units. Vanadium (IV) octahedral units are blue, selenium is yellow and oxygen is red.

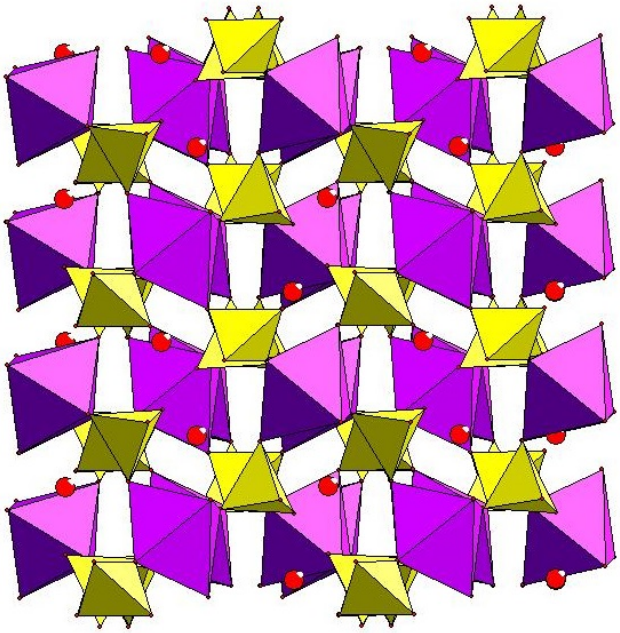

Fig. 5. 2: The edge-sharing vanadium oxide dimers connected into the 3D structure of $Li_2V_2(SO_4)_3$ by corner-sharing SO_4 tetrahedral units. Vanadium (II) octahedral units are purple, sulfate tetrahedral units are yellow and Li^+ is red.

5.1.2 Synthesis

Seven vanadium compounds of varying dimensionality have been synthesised and will be described in this chapter. These compounds range from monomers up to 2D layered structures. The compounds have vanadium oxidation states from V^{3+} to V^{5+}.

V-10, 11, 13, 15 & 16 were prepared solvothermally in 40mL Teflon lined steel autoclaves. V-14 was prepared ionothermally in a 27 mL Teflon lined steel autoclave. V-12 was prepared as an aqueous reaction in a 20 mL polypropylene bottle.

V-10, $Cs_2V_2O_3(SO_4)_2$: $VOSO_4$ (3 mmol, 0.489 g) and Cs_2CO_3 (1 mmol, 0.326 g) were dissolved in 48% HF (31 mmol, 0.5 mL). Water (1 mmol, 2 mL) and ethylene glycol (80 mmol, 5 mL) was added to the resultant mixture and allowed to settle before being sealed and heated for 72 hours at 100 ^oC. The product consisted of blue block-like crystals, indicating V(IV).

V-11, $Rb_2VF_3(SO_4)$: $VOSO_4$ (3 mmol, 0.489 g) and RbF (2 mmol, 0.209 g) were dissolved in 48% HF (31 mmol, 0.5 mL). A 1:1 ratio of water (1 mmol, 2 mL) and ethylene gylcol (32 mmol, 2 mL) was added to the solution which was allowed to settle and then sealed and heated at 160 ^oC for 72 hours. The product consisted of green block-like crystals, indicating V(III).

V-12, $[H_4TETA]_2[V_{10}O_{28}].4H_2O$: V_2O_5 (1 mmol, 0.182 g) and triethylenetetramine (2 mmol, 0.5 mL) were dissolved in 48% HF (31 mmol, 0.5 mL). A 3:1 ratio of water (3 mmol, 6 mL) and ethylene glycol (32 mmol, 2 mL) was added then sealed and heated at 60 ^oC for 72 hours. The reaction was cooled to room temperature at a rate of 0.1 $^oC\ min^{-1}$. The product consisted of orange block-like crystals, indicating V(V).

V-13, $[CN_3H_6]_3[VF_6]$: V_2O_5 (1 mmol, 0.182 g) and guanidinium carbonate (0.5 mmol, 0.091 g) were dissolved in 48% HF (31 mmol, 0.5 mL). A 5:3 ratio of water (1.25 mmol, 2.5 mL) and ethylene glycol (24 mmol, 1.5 mL) was added, sealed, and heated at 160 ^oC for 72 hours. The product consisted of green prismatic crystals, indicating V(III).

V-14, $[CN_3H_6][V_2O_2F_5]$: VOF_3 (1 mmol, 0.124 g) and guanidinium carbonate (0.5 mmol, 0.091 g) were dissolved in 48% HF (6.2 mmol, 0.1 mL) and mixed in 1-ethyl-2-methylimidazolium trifluoromethylsulfonylimide (~3mmol, 1.5 g) before being sealed and heated for 48 hours at 160 ^oC. The product consisted of ble plate-like crystals, indicating V(IV).

V-15, $[V_2O_2F_2(H_2O)_2].H_2O$: VF_3 (2 mmol, 0.215 g) and diethylamine (1 mmol, 0.5 mL) were dissolved in 48% HF (31 mmol, 0.5 mL). Ethylene glycol (3.2 mmol, 0.2 mL) was added to the resultant mixture along with H_2SeO_3 (1 mmol, 0.129 g) and allowed to settle before being sealed and heated at 120 ^oC for 96 hours. The product consisted of small blue block-like crystals, indicating V(IV).

V-16, $[CN_3H_6]_3[V_2O_2F_7]$: V_2O_5 (1 mmol, 0.182 g) and guanidine carbonate (1 mmol, 0.182 g) were dissolved in 48% HF (31 mmol, 0.5 mL). Water (1 mmol, 2 mL) was added to the resultand mixture before it was sealed, and heated at 160 ^oC for 24 hours. The product consisted of blue block-like crystals indicating V(IV).

All compounds with the exception of V-15 were filtered and washed in water. V-15 was washed with methanol to remove the ionic liquid from the sample. V-11, and 13 were green in colour, with block-like morphologies, indicating V(III), this was confirmed upon BVS calculation. V-10, 14, 15 and 16 were blue in colour, indicating V(IV), with plate and block-like morphologies. V-12 was brown/orange in colour, indicating V(V), with a prismatic morphology, this will be discussed in more detail in the relevant section. If mixed phases or impurities were present, the samples were separated using an optical microscope.

5.2 Monomers

V-13, $[CN_3H_6]_3VF_6$, is comprised of isolated VF_6 octahedral units (Fig. 5. 3). The unit cell is comprised of the inorganic VF_6 monomeric units that sit on the corners, edges, faces and centres of each cell, surrounded by the organic protonated guanidine molecules (Fig. 5. 4). There are two crystallographically unique vanadium sites in the structure, V1 (0, 0, 0) and V2 (0, 0, ½). There is only one crystallographic guanidine site. The VF_6 octahedral units are completely symmetrical, sitting on the three-fold rotation sites, due to the nature of the cubic $Pa\bar{3}$ space group, requiring only a single fluorine atom to populate the octahedral units by symmetry operations. V1 – F1 = 1.946(7) Å and V2 – F2 = 1.945(6) Å, so the two octahedral units are slightly different in size. The monomeric VF_6 units exhibit an alternate tilting effect when viewed along a principal axis (Fig. 5. 5). The protonated guanidinium ions also exhibit a similar tilt when viewed perpendicular to each axis, as well as an alternating 'up' and 'down' orientation (Fig. 5. 6).

The vanadium sites are both in the V(III) oxidation state, which have been confirmed using bond valence sum (BVS) calculations. The V – F bond lengths are presented in Table 5. 4 along with the BVS calculations for each vanadium site. The VF_6 octahedral units are hydrogen bonded through the guanidine moieties to form the full 3D structure. A list of hydrogen bond lengths are given in Table 5. 5.

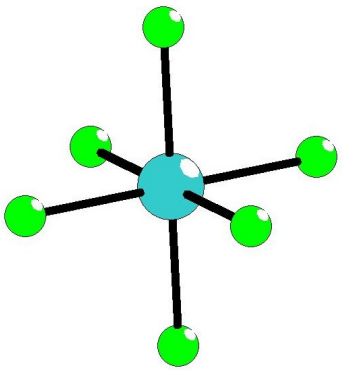

Fig. 5. 3: The VF_6 octahedral unit in $[CN_3H_5]_3[VF_6]$, vanadium is turquoise and fluorine is green.

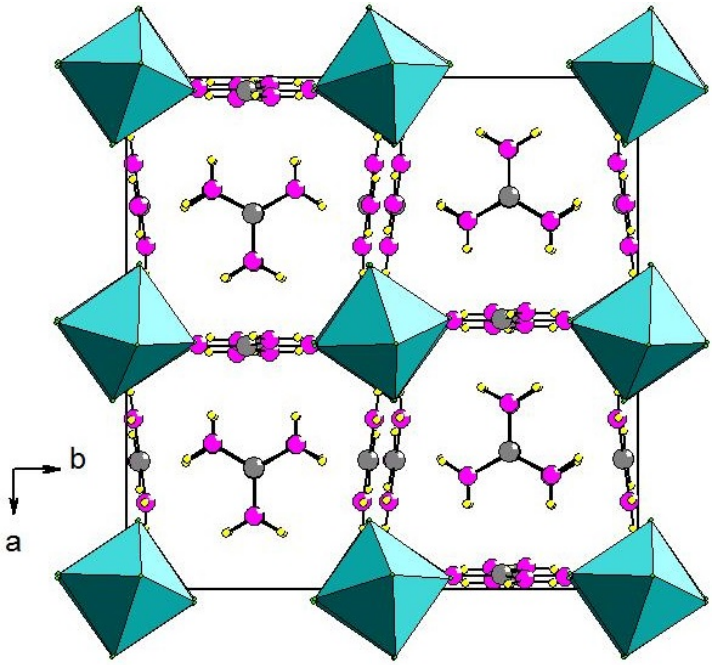

Fig. 5. 4: The $Pa\bar{3}$ unit cell of $[CN_3H_6]_3[VF_6]$ viewed along axis *c*. Vanadium (and vanadium octahedral units) is in turquoise, fluorine is green, nitrogen is purple, carbon is grey and hydrogen is yellow.

Table 5. 4: V – F bond lengths and bond valence sums for V1 and V2 in $[CN_3H_6]_3[VF_6]$.

Bond	Length (Å)	S_{ij}
V1 – F1 x6	1.946(7)	0.517 x6
		ΣV1 = 3.102
V2 – F2 x6	1.945(6)	0.519 x6
		ΣV2 = 3.114

The sample is not phase pure, evidenced by the experimental PXRD pattern compared to the theoretical pattern obtained from the single crystal data (Fig. 5. 7) and the results of the CHN analysis which are given in Table 5. 6. It seems likely, based on this information that the bulk product is made up of recrystallised guanidine.

Table 5. 5: Hydrogen bond lengths in $[CN_3H_6]_3[VF_6]$.

D – H	Length (Å)	H --- A	Length (Å)	*d*(D – H --- A) (Å)
N2 – H5	0.784(11)	H5 – F1	2.069(16)	2.853(15)
N1 – H3	0.894(13)	H3 – F1	2.096(12)	2.990(11)
N4 – H4	0.835(11)	H4 – F1	2.132(13)	2.967(12)
N2 – H2	0.876(18)	H2 – F2	2.049(19)	2.925(17)
N3 – H6	0.773(19)	H6 – F2	2.079(14)	2.852(13)
N1 – H1	0.871(15)	H1 – F2	2.134(11)	3.005(16)

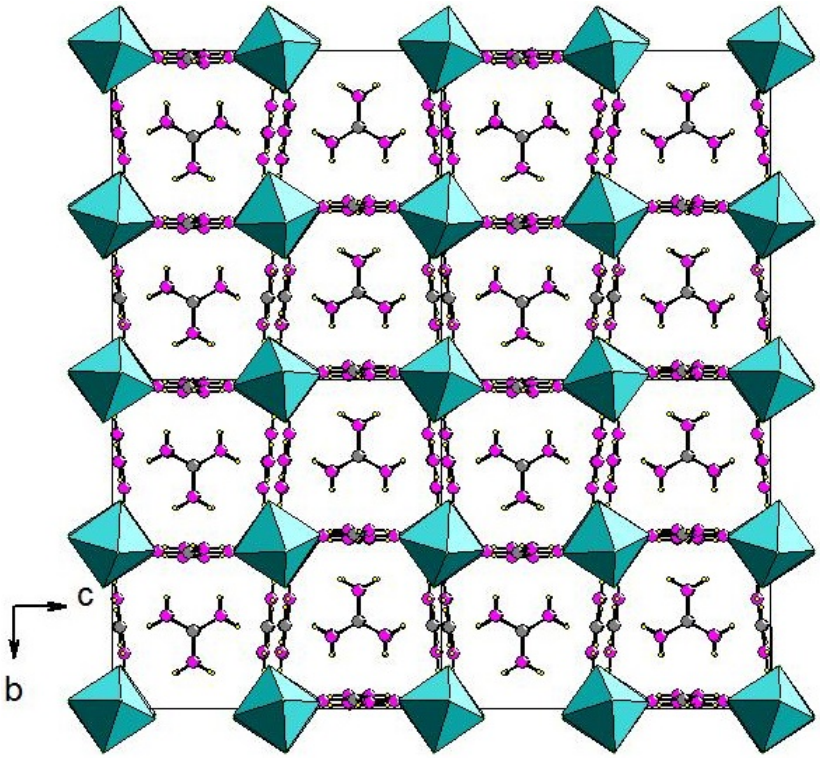

Fig. 5. 5: The extended packing of the 2x2 unit cell in $[CN_3H_6]_3[VF_6]$, showing the octahedral tilts perpendicular to axis *b* and axis *c*. Vanadium (and its octahedral units) is turquoise, fluorine is green, nitrogen is purple, carbon is grey and hydrogen is yellow.

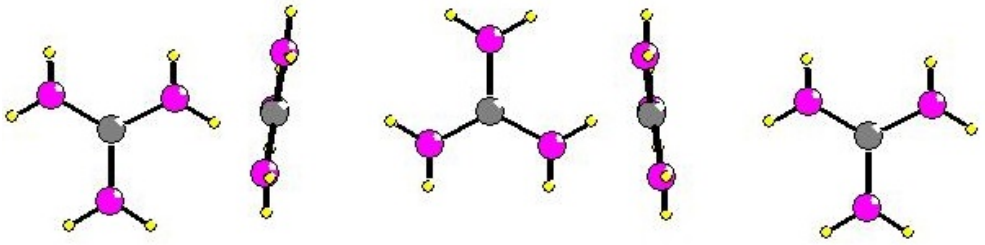

Fig. 5. 6: The alternating up and down orientation and perpendicular tilt of the guanidinium ions.

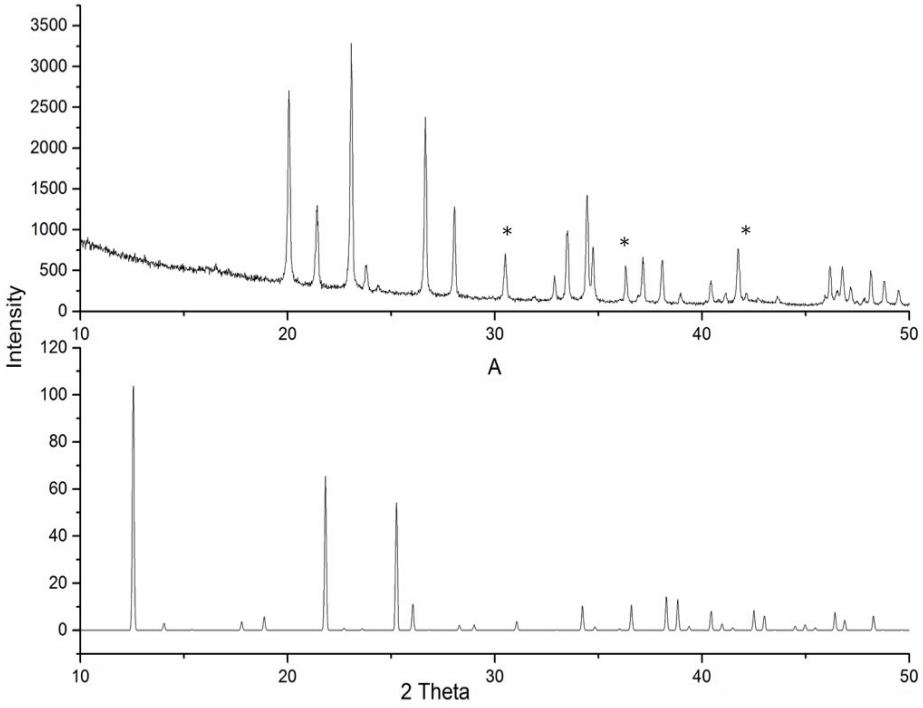

Fig. 5. 7: The experimental PXRD pattern (top) and the theoretical pattern (bottom) for V-13. Teflon peaks are marked with an asterisk. It can be seen that the experimental pattern represents a different phase than the theoretical pattern obtained from single crystal data.

Table 5. 6: CHN analysis data for V-13.

Element	%age calculated	%age found
Carbon	2.47	9.23
Nitrogen	2.68	13.08
Hydrogen	1.25	2.42

Na_3VF_6 is comprised of the same octahedral VF_6 monomeric units as V-13.[12] The main difference is that there is only a single crystallographic vanadium site in Na_3VF_6 where there are two in V-13. Na_3VF_6 crystallises in the monoclinic $P2_1/c$ space group and shows a similar octahedral tilting arrangement as V-13 (Fig. 5. 8). There are two crystallographically unique sodium sites, Na1 (0, 0, ½) which is 6-coordinate and Na2 (½, 0.055, 0.240) which is 8-coordinate. The structure is in the V(III) oxidation state.

$[NH_4]_2NaVF_6$ is also closely related to V-13.[12] It too consists of octahedral VF_6 monomer units with the NH_4^+ and Na^+ cations occupying the interstitial sites. However, there is no tilting of the octahedral units (Fig. 5. 9) resulting in the increased symmetry of the $Fm\bar{3}m$ space group, and like Na_3VF_6 there is only a single crystallographic vanadium site. The sodium ion sits on the (0, -½, ½) position and is 6-coordinate, as is Na1 of Na_3VF_6. BVS calculations for both compounds, along with V – F bonds lengths are presented in Table 5. 7.

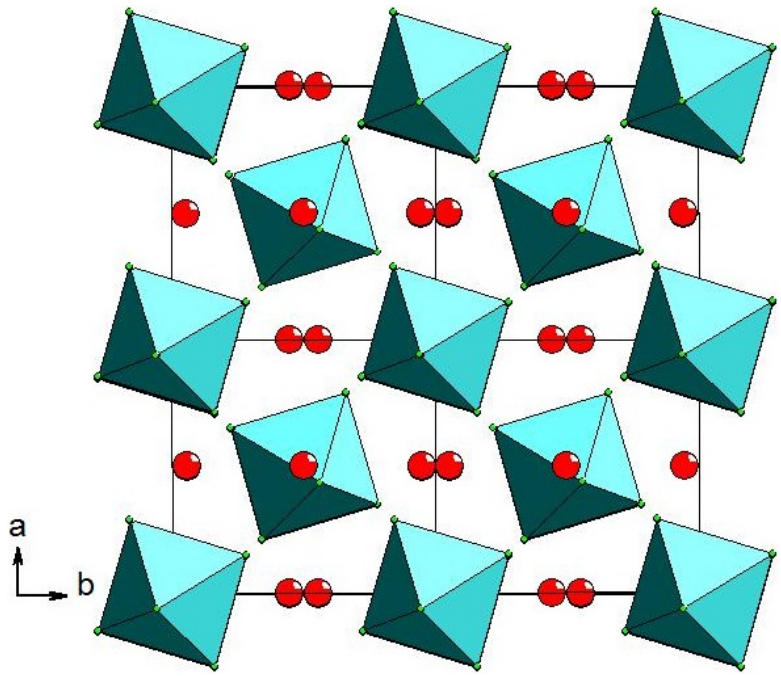

Fig. 5. 8: The extended 2x2 unit cell of Na_3VF_6 as viewed along axis *c* showing the alternating octahedral tilts running along axis *a*. Sodium is in red, and the VF_6 octahedral units are in turquoise.

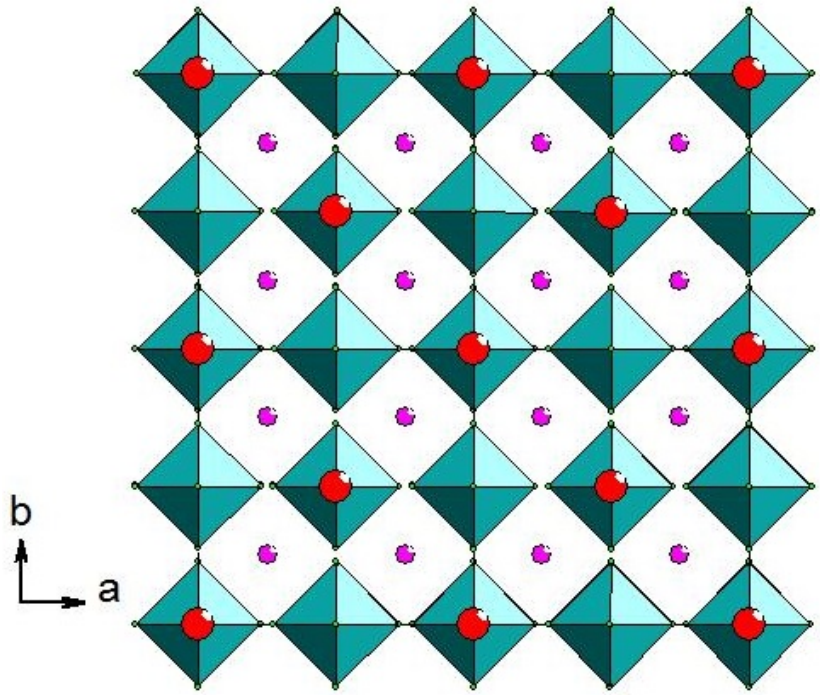

Fig. 5. 9: The extended 2x2 unit cell of $[NH_4]_2NaVF_6$ in the *Fm*-3*m* space group. There is no octahedral tilting in this compound unlike V-13 and Na_3VF_6. Sodium is red, nitrogen is purple and the VF_6 octahedra are turquoise.

Table 5. 7: V – F bond lengths and BVS for Na_3VF_6 (top) and $[NH_4]_2NaVF_6$ (bottom).

Bond	Length (Å)	S_{ij}
V1 – F1 x2	1.818(3)	0.557 x2
V1 – F2 x2	1.859(4)	0.543 x2
V1 – F3 x2	1.867(7)	0.540 x2
		ΣV1 = 3.280
V1 – F1 x6	1.927(5)	0.522 x6
		ΣV1 = 3.132

Due to the different counter cation species and their respective atomic radii, there are large differences between the V – V distances in V-13 and those of the two

analogous compounds described above. The larger guanidine moieties in V-13 space the VF_6 units further apart than the Na^+/NH_4^+ cations in Na_3VF_6 and $[NH_4]_2VF_6$. V – V distances for all three compounds are given inTable 5. 8.

Table 5. 8: The V – V distances for the three related VF_6-containing compounds.

Compound	V – V distance (Å)
$[CN_3H_6]_3VF_6$ (V-13)	7.048(2)
Na_3VF_6	5.640(2)
$[NH_4]_2NaVF_6$	6.015(6)

The 6-coordination of the sodium cation on the Na1 site in Na_3VF_6 and $[NH_4]_2NaVF_6$ are indicative of a perovskite type structure. Na_3VF_6 has a monoclinic cryolite-type structure, while $[NH_4]_2NaVF_6$ has a cubic elpasolite-type structure. While these structures bear significant resemblance to V-13, the absence of any 6-coordinate guanidine sites in V-13 preclude it from being described as either of these perovskite-type structures.

5.3 Dimers

V-16, $[CN_3H_6]_3[V_2O_2F_7]$, is comprised of face-sharing octahedral $VOF_2F_{3/2}$ dimer units bridged through fluorine (Fig. 5. 10). The unit cell is comprised of these $VOF_2F_{3/2}$ dimeric units with protonated guanidinium ions stacked perpendicular to the VOF units (Fig. 5. 11). The compound crystallises in the monoclinic $C2/c$ space group. The shorter, non-bridging, vanadyl bonds sit exo to the dimeric units in the structure. There is a single crystallographic vanadium site with four unique fluorine sites and one oxygen site. There are two unique guanidine moieties, two carbon sites and six nitrogen sites. These models were of sufficient data quality that the hydrogen atoms bonded to nitrogen could be freely refined. This compound is analogous to $Cs_3V_2O_2F_7$ which also exhibits vanadium (IV) face-sharing dimeric $VOF_2F_{3/2}$ octahedral units with the same conformation as V-17 (Fig. 5. 10).[13, 14] There are other compounds which also exhibit face-sharing vanadium (oxy)fluoride dimeric units; $(NMe_4)_3V_2F_9$ with vanadium (III) face-sharing dimer units and; $[NH_4]_3[V_2O_4F_5]$ with vanadium (V) face-sharing dimer units.[15] Face-sharing vanadium dimers appear to be less common than corner-sharing; $[NMe_4]Cs[V_2O_2F_8(H_2O)]$[16] $K_2[NMe_4][V_2O_2F_9]$[16] and edge-sharing; $[NMe_4]_2[V_2O_2F_6(H_2O)_2]$[17] dimers, of which there are many more examples in the literature.[16, 18-20] Selected V – O and V – F bond lengths along with BVS calculations for V-17 are presented in Table 5. 9. The guanidium ions form hydrogen bonds through fluorine and oxygen with the dimers, creating the full 3D structure. A full list of H – F and H – O bonds is given in Table 5. 10.

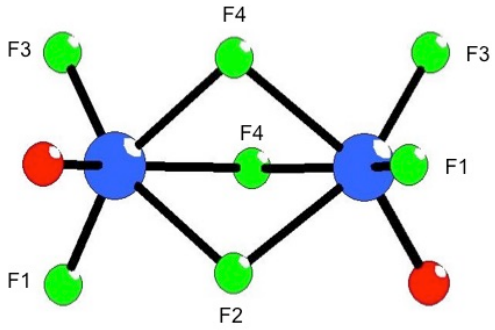

Fig. 5. 10: The vanadium (IV) face-sharing dimeric units in $[CN_3H_6]_3[V_2O_2F_7]$ and its analogue $Cs_3V_2O_2F_7$. The dimers are each bridged through fluorine and have the short vanadyl bonds exo to the dimer unit. Vanadium is blue, fluorine is green and oxygen is red.

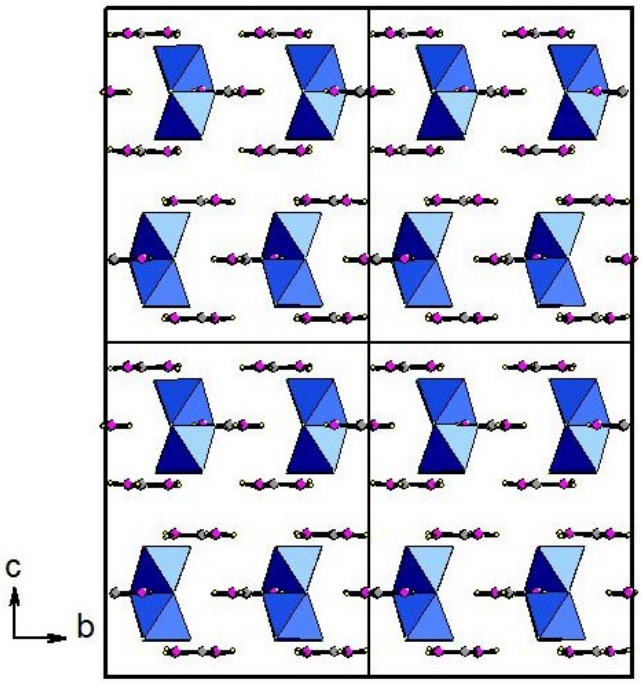

Fig. 5. 11: The extended 2x2 $C2/c$ unit cell for $[CN_3H_6]_3[V_2O_2F_7]$ showing the packing of the dimers along axis c and the perpendicular relation of the guanidinium ions relative to the dimers. Vanadium oxyfluoride dimers are in blue, carbon is grey, nitrogen is purple and hydrogen is yellow.

Table 5. 9: The V – O and V – F bond lengths and BVS calculations for V-16.

Bond	Length (Å)	S_{ij}
V1 – O1	1.669(3)	1.365
V1 – F3	1.696(2)	1.011
V1 – F1	1.731(5)	0.925
V1 – F4	2.092(3)	0.349
V1 – F2	2.109(1)	0.333
V1 – F4	2.125(3)	0.319
		ΣV1 = 4.302

Table 5. 10: Hydrogen bonds in $[CN_3H_6]_3[V_2O_2F_7]$.

D – H	Length (Å)	H ---A	Length (Å)	*d*(D – H --- A) (Å)
N3 – H8	0.851(18)	H8 – F1	2.104(12)	2.955(16)
N2 – H5	0.823(13)	H5 – F1	2.125(11)	2.948(14)
N4 – H2	0.782(19)	H2 – F2 x2	2.147(18)	2.929(17)
N3 – H3	0.892(16)	H3 – F3	2.059(12)	2.951(18)
N4 – H4	0.899(12)	H4 – F4	2.017(18)	2.916(16)
N2 – H6	0.942(13)	H6 – O1	2.026(10)	2.968(12)

5.4 Chains

V-11, $Rb_2VF_3(SO_4)$, is comprised of corner-sharing $VF_2F_{2/2}(O_{2/2}SO_2O_{2/2})$ octahedral and tetrahedral units (Fig. 5. 12). The corner-sharing octahedral vanadium units form 1D chains that are bi-capped by the sulfate tetrahedral units (Fig. 5. 13). The compound crystallises in the orthorhombic *Pnab* space group, with the chains running along the direction of axis *a* and the heavy Rb^+ cations occupying the interstitial sites (Fig. 5. 14).

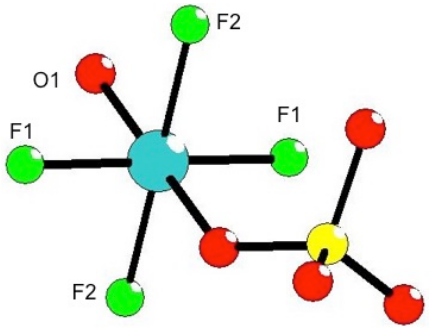

Fig. 5. 12: The $VF_{2/2}O_{2/2}(SO_2O_{2/2})$ octahedral and tetrahedral units that comprise the bi-capped 1D chain in V-11. Vanadium is turquoise, fluorine is green, oxygen is red and sulphur is yellow.

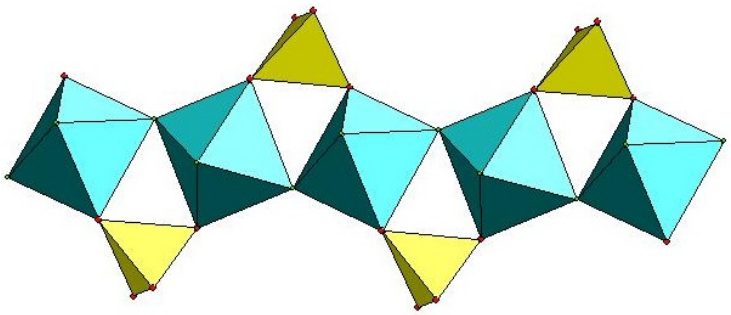

Fig. 5. 13: The bi-capped 1D vanadium (III) fluorosulfate chain that comprises V-11. V-centred octahedral units are turquoise and SO_4tetrahedral units are yellow.

Vanadium is in the (III) oxidation state and is represented by a single crystallographic site on the (0, ½, ½) position, with two fluorine positions and one oxygen position surrounding it. Selected V – O and V – F bond lengths along with

BVS for V-11 are given in Table 5. 11. The experimental and theoretical PXRD patterns are shown in Fig. 5. 15. The sample appears to be relatively pure when compared to the theoretical pattern.

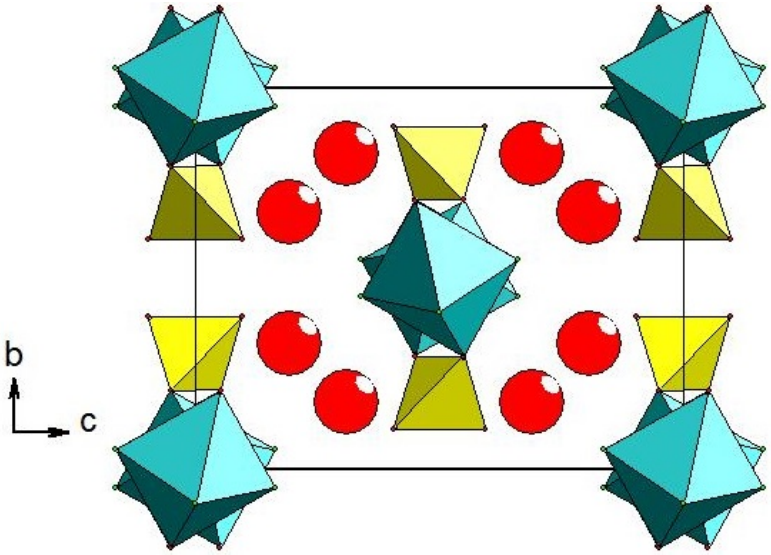

Fig. 5. 14: The packed unit cell of $Rb_2VF_3(SO_4)$ showing the 1D vanadium chains bi-capped by sulfate running parallel with axis *a* and the sulfate tetrahedral units extending into axis *b*. The large 8-coordinate Rb^+ cations occupy the interstitial sites in the structure. Vanadium octahedral units are turquoise, sulfate tetrahedral units are yellow and Rb^+ is red.

Table 5. 11: Selected V – O and V – F bond lengths and BVS for V-11.

Bond	Length (Å)	S_{ij}
V1 – F1 x2	1.870(5)	0.635 x2
V1 – F2 x2	1.961(2)	0.497 x2
V1 – O1 x2	2.006(3)	0.491 x2
		$\Sigma V1 = 3.246$

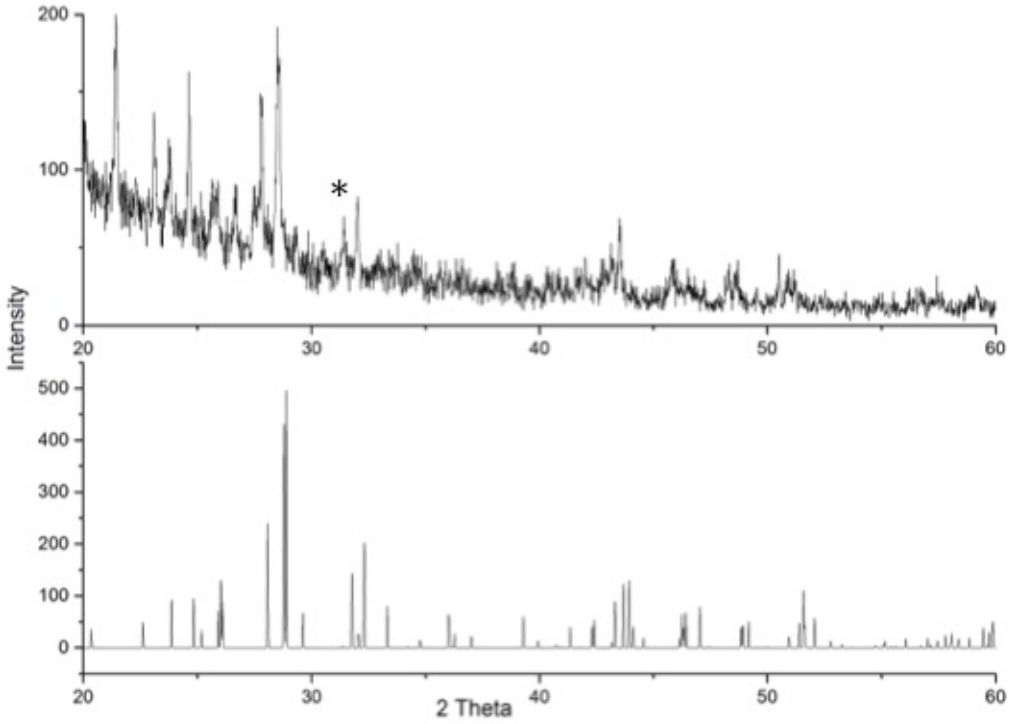

Fig. 5. 15: The experimental PXRD pattern (top) and the theoretical pattern obtained from single crystal refinement (bottom) of V-11.

Due to the relatively small amount of powder available for X-ray, the sample was loaded into a Teflon disc and inserted into the metal PXRD disc before it was X-rayed. The Teflon accounts for the peaks that occur at around 21 and 24 degrees. The PXRD pattern for the empty Teflon holder is included in the appendix for reference.

V-10, $CsV_2O_3(SO_4)_2$, was produced from a reaction similar to V-11, incorporating sulfate into the reaction in an attempt to increase the connectivity and dimensionality of the product. V-10 consists of an edge-sharing square-pyramidal vanadium oxide chain with corner-sharing vanadium oxide octahedral units bonded at alternating corners (Fig. 5. 16). This extended vanadium chain is bi-capped by sulfate tetrahedral units (Fig. 5. 17). The chains run parallel with axis *a*, in a manner similar to V-10, with the sulfate tetrahedral units protruding into axis *b* (Fig. 5. 18).

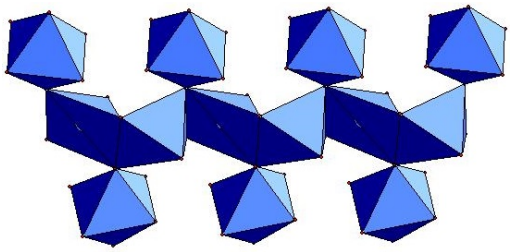

Fig. 5. 16: The vanadium oxide chain structure in $Cs_2V_2O_3(SO_4)_2$ showing the square planar edge-sharing V (IV) oxide chain with alternating V (IV) oxide corner-sharing octahedral units.

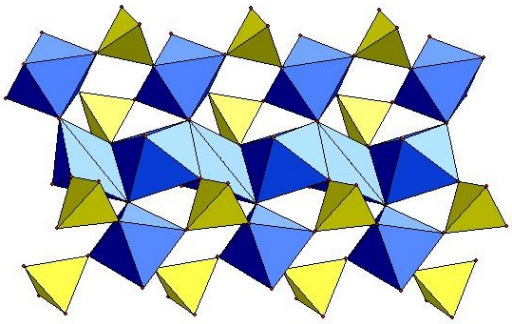

Fig. 5. 17: The vanadium (IV) oxide chain bi-capped by sulfate tetrahedral units. Vanadium polyhedra are in blue and sulfate tetrahedra are in yellow.

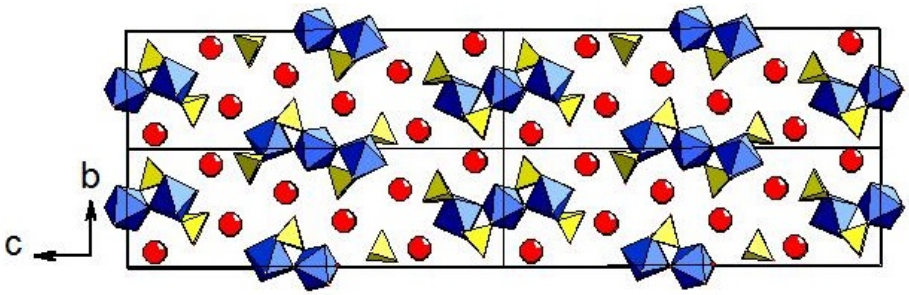

Fig. 5. 18: The extended 2x2 unit cell of $Cs_2V_2O_3(SO_4)_2$ viewed along axis *a* showing the vanadium oxide sulfate chains running parallel to the axis. Cs^+ cations occupy the interstitial sites. Vanadium units are blue, sulphate units are yellow and Cs^+ is red.

Both vanadium sites are in the V (IV) oxidation state, and both have short V = O, vanadyl bonds, which are common in V (IV) compounds. Selected V – O bonds lengths and BVS calculations are presented in Table 5. 12.

Table 5. 12: Selected V – O bonds and BVS calculations for $Cs_2V_2O_3(SO_4)_2$.

Bond	Length (Å)	S_{ij}
V1 – O1	1.573(5)	1.583
V1 – O4	1.880(2)	0.691
V1 – O9	1.992(3)	0.510
V1 – O11	2.052(2)	0.434
V1 – O5	2.062(2)	0.422
V1 – O8	2.118(5)	0.363
		ΣV1 = 4.003
V2 – O10	1.572(6)	1.588
V2 – O6	1.907(4)	0.662
V2 – O11	2.016(4)	0.488
V2 – O11	2.070(8)	0.413
V2 – O6	2.074(1)	0.409
		ΣV2 = 3.560

5.5 Clusters

V-12, $[H_4TETA]_2[V_{10}O_{26}].4H_2O$, consists of ten edge-sharing V (V) octahedral units that form the $V_{10}O_{28}$ cluster (Fig. 5. 19). These clusters are templated by the protonated tetramethylenetriamine (H_4TETA) units that sit in the spaces along with the non-coordinated water molecules (Fig. 5. 20). Selected V – O bond lengths and BVS calculations are presented in Table 5. 13.

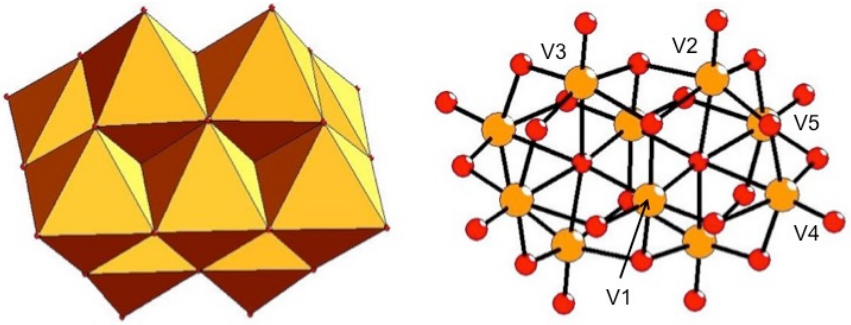

Fig. 5. 19: The $V_{10}O_{28}$ cluster comprised of face-sharing octahedral building units.

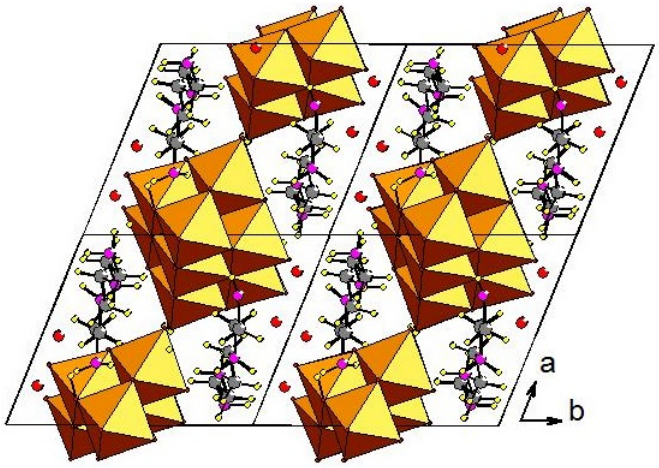

Fig. 5. 20: The extended 2x2 unit cell of $[H_4TETA]_2[V_{10}O_{28}].4H_2O$, viewed along axis *c* showing the cluster units separated by the H_4TETA units and non-bonded water molecules. The V (V) cluster units are orange, carbon is grey, nitrogen is purple and hydrogen is yellow. The free water molecules are red, and the hydrogen atoms could not be located.

Table 5. 13: Selected V – O bond lengths and BVS calculations for V-12.

Bond	Length (Å)	S_{ij}	Bond	Length (Å)	S_{ij}
V1 – O4	1.681(2)	1.182	V4 – O13	1.605(3)	1.452
V1 – O5	1.719(3)	1.067	V4 – O9	1.822(4)	0.808
V1 – O2	1.900(1)	0.654	V4 – O11	1.873(2)	0.704
V1 – O1	1.947(4)	0.576	V4 – O10	1.911(8)	0.635
V1 – O3	2.114(2)	0.367	V4 – O4	2.074(5)	0.409
V1 – O3	2.134(2)	0.348	V4 – O3	2.297(4)	0.224
		ΣV1 = 4.933			**ΣV4 = 4.977**
V2 – O8	1.617(1)	1.406	V5 – O14	1.605(2)	1.452
V2 – O12	1.798(2)	0.862	V5 – O9	1.849(4)	0.751
V2 – O11	1.853(1)	0.743	V5 – O6	1.867(2)	0.715
V2 – O1	1.986(3)	0.513	V5 – O12	1.915(6)	0.628
V2 – O2	2.022(5)	0.470	V5 – O5	2.044(3)	0.443
V2 – O3	2.236(8)	0.264	V5 – O3	2.301(4)	0.221
		ΣV2 = 5.014			**ΣV5 = 4.952**
V3 – O7	1.626(3)	1.372			
V3 – O6	1.813(6)	0.828			
V3 – O10	1.844(4)	0.761			
V3 – O2	1.975(9)	0.534			
V3 – O1	1.944(2)	0.507			
V3 – O3	2.237(4)	0.263			
		ΣV3 = 5.015			

The oxidation state of V(V) is calculated using BVS calculations, but does not charge balance properly given the formula $[H_4TETA]_2[V_{10}O_{28}]$. It may be the case that the TETA moiety is less protonated on the nitrogen sites than the refinement suggests. If $[H_3TETA]_2$ were taken instead then this would work well with the V(V) oxidation state calculated. Sample purity is rather low, shown by PXRD (Fig. 5. 21), with the bulk phase being made up of recrystallised starting materials, and is confirmed by CHN analysis data, given in Table 5. 14.

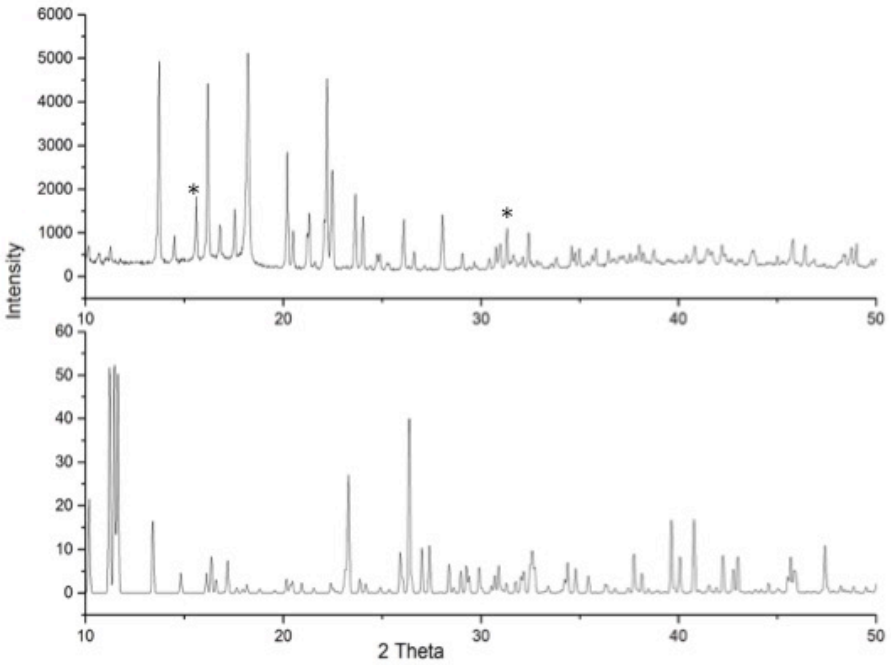

Fig. 5. 21: The experimental PXRD pattern (top) and the theoretical pattern (bottom) for V-12, teflon peaks are marked with an asterisk. The experimental pattern obtained from single crystal data does not represent the bulk phase.

Table 5. 14: CHN analysis data for V-12.

Element	%age calculated	%age found
Carbon	10.84	14.97
Nitrogen	8.43	11.21
Hydrogen	3.32	6.26

5.6 Layers

V-14, $[CN_3H_6]V_2O_2F_5$ consists of $VOF_{5/2}$ edge-sharing dimer octahedral units that share corners with other dimers to form a 2D zig-zag layer of ladder units (Fig. 5. 22). The layers are separated by protonated guanidine molecules that conform with the zig-zag conformation of the layer (Fig. 5. 23). Selected V – F and V – O bond lengths along with BVS calculations for V-15 are given in Table 5. 15.

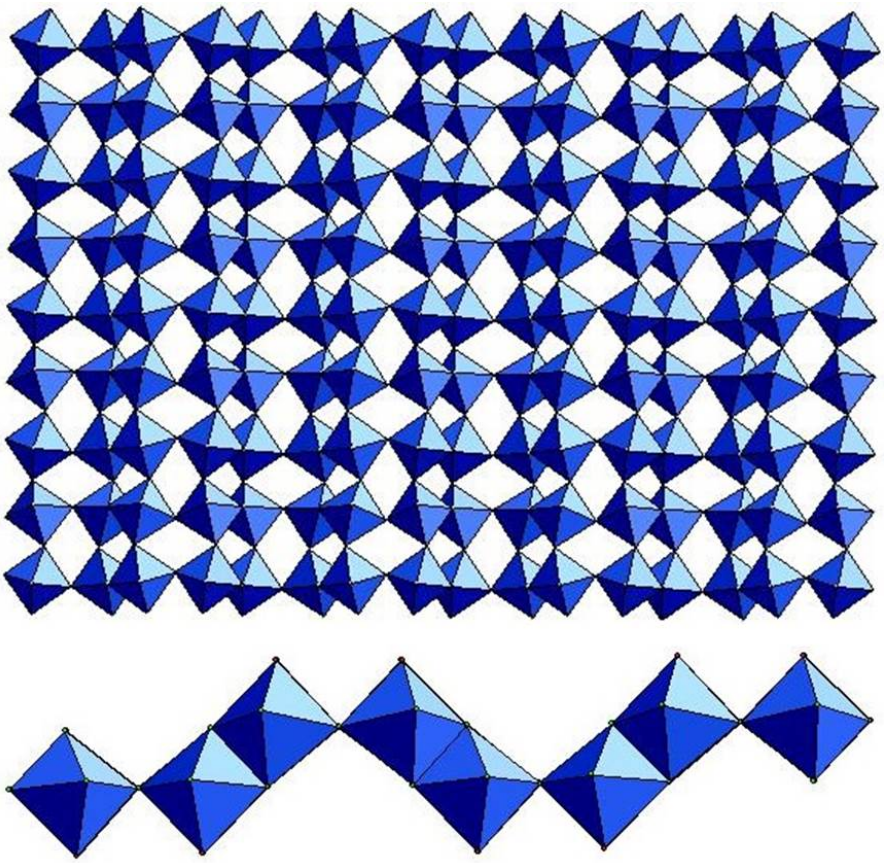

Fig. 5. 22: 2D layer built up of corner and edge-sharing V (IV) dimers bridged through fluorine viewed perpendicular to the plane of the layer (top) and the zig-zag conformation that can be seen when viewed along the plane of the layer (bottom).

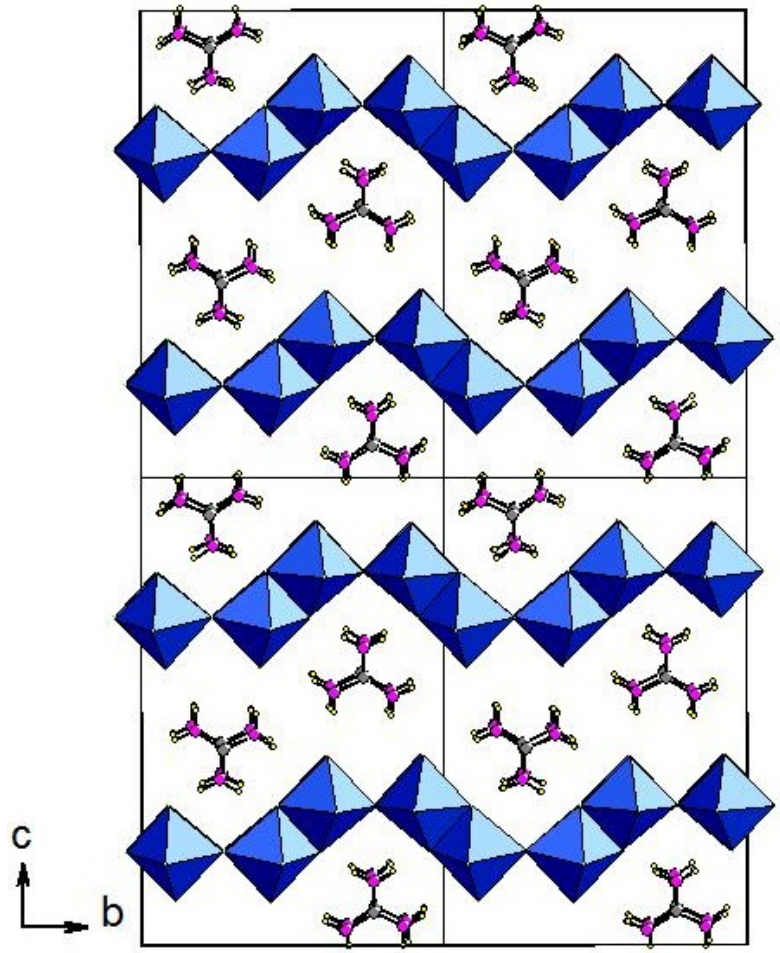

Fig. 5. 23: The extended 2x2 unit cell of $[CN_3H_6][V_2O_2F_5]$ viewed along axis *a* showing the zig-zag conformation of the VOF layers templated by the protonated guanidine moieties. VOF octahedral units are blue, carbon is grey, nitrogen is purple and hydrogen is yellow.

This compound is related to three previously synthesised structures; $[C_3N_2H_5][V_2O_2F_5]$, $[C_4N_2H_5][V_2O_2F_5]$, and $[C_7N_2H_6][V_2O_2F_5]$ which all exhibit the same layer as V-14 (Fig. 5. 22), spaced by the differently sized organic moieties, benzimidazolium, pyrazinium and imidazolium respectively.[21] All compounds were synthesised in the same way, varying only the organic template, using ionic liquid in place of traditional solvent as was done with V-14. All of these compounds are also in the V (IV) oxidation state that corresponds well with V-14. The protonated guanidine moieties form hydrogen bonds through the F and O ligands of each layer, a full list of H – F and H – O bonds is given in Table 5. 16.

Table 5. 15: Selected V – F and V – O bond lengths and BVS calculations for V-14.

Bond	Length (Å)	S_{ij}	Bond	Length (Å)	S_{ij}
V1 – O1	1.612(2)	1.425	V3 – O4	1.606(3)	1.448
V1 – F6	1.940(3)	0.526	V3 – F5	1.935(6)	0.533
V1 – F9	1.944(1)	0.520	V3 – F7	1.942(2)	0.523
V1 – F1	1.950(4)	0.512	V3 – F8	1.955(1)	0.505
V1 – F10	1.963(2)	0.494	V3 – F4	1.955(1)	0.505
V1 – F2	2.155(2)	0.294	V3 – F3	2.179(3)	0.274
		ΣV1 = 3.924			**ΣV3 = 3.946**
V2 – O3	1.609(4)	1.436	V4 – O2	1.596(7)	1.488
V2 – F6	1.940(3)	0.526	V4 – F3	1.947(4)	0.516
V2 – F2	1.959(2)	0.499	V4 – F5	1.950(8)	0.512
V2 – F8	1.966(8)	0.490	V4 – F9	1.967(2)	0.489
V2 – F7	2.000(3)	0.447	V4 – F10	1.978(2)	0.474
V2 – F1	2.184(3)	0.272	V4 – F4	2.161(2)	0.289
		ΣV2 = 3.826			**ΣV4 = 3.930**

Table 5. 16: Hydrogen bonds lengths in $[CN_3H_6][V_2O_2F_5]$.

D – H	Length (Å)	H --- A	Length (Å)	*d*(D – H --- A) (Å)
N1 – H1A	0.860(14)	H1A – F1	1.988(16)	2.848(11)
N6 – H6B	0.860(14)	H6B – F2	2.107(16)	2.967(13)
N4 – H4B	0.860(14)	H4B – O2	2.127(14)	2.987(18)
N2 – H2B	0.860(14)	H2B – O3	2.088(12)	2.948(12)

The sample is not phase pure, as evidenced by the experimental PXRD pattern when compared to the theoretical pattern obtained from the single crystal refinement (Fig. 5. 24). It seems likely that the bulk phase is comprised of recrystallised guanidine.

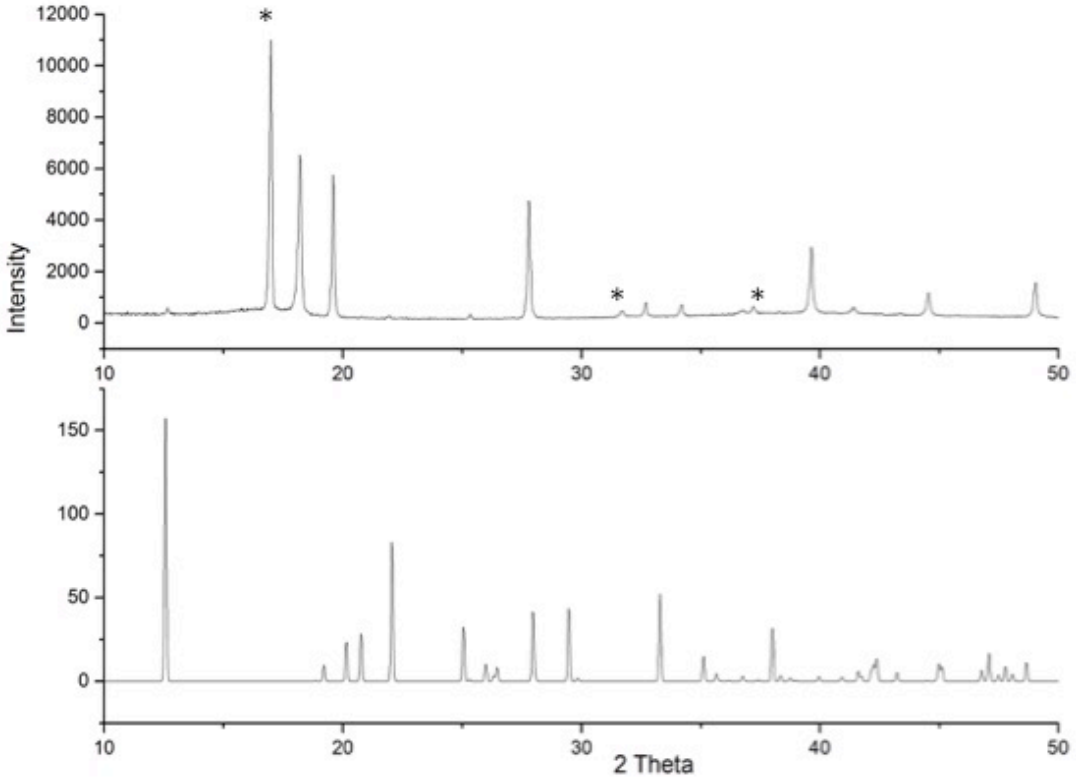

Fig. 5. 24: The experimental PXRD pattern (top) and the theoretical pattern (bottom) for V-14. The single crystal phase appears to be different from the bulk phase.

V-15, $V_2O_2F_4(H_2O)_2.H_2O$, consists of edge-sharing dimer $VO(OH_2)F_{4/2}$ octahedral building units that share corners with other dimers to form a 2D layer of corner and edge-sharing dimers (Fig. 5. 25) with non-coordinated water molecules separating the layers (Fig. 5. 26). Selected V – O and V – F bond lengths along with BVS calculations for V-16 are given in Table 5. 17. V-15 exhibits a similar layer structure to VOF_3 (Fig. 5. 27) in which edge-sharing dimers share corners with other dimers to form a 2D layer perpendicular to axis *a* (Fig. 5. 28).

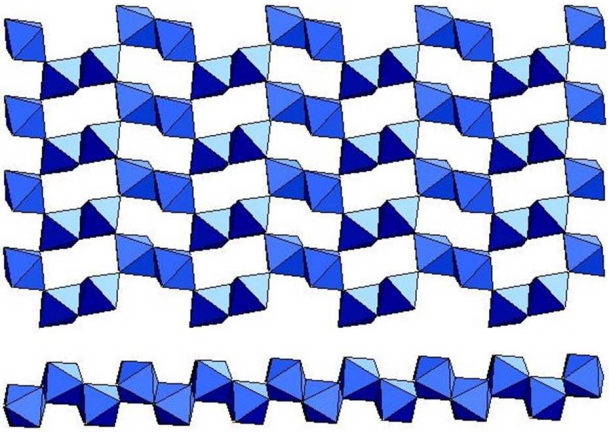

Fig. 5. 25: Layer built up of corner and edge-sharing V (IV) octahedral units (top), and the zig-zag conformation seen when the layer is viewed parallel to the plane (bottom). The hydrogens have been omitted from the water ligands for clarity.

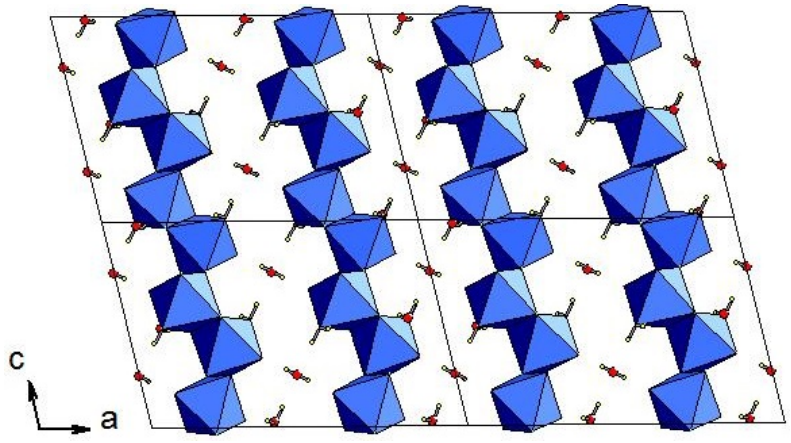

Fig. 5. 26: The extended 2x2 unit cell of $V_2O_2F_4(H_2O)_2.H_2O$ viewed along axis *b* showing the V (IV) layers separated by the non-coordinated water molecules.

Table 5. 17: Selected V – O and V – F bond lengths and BVS calculations for V-15.

Bond	Length (Å)	S_{ij}
V1 – O2	1.593(5)	1.676
V1 – F2	1.946(2)	0.514
V1 – F1	1.970(3)	0.482
V1 – F2	1.974(3)	0.477
V1 – O1	2.028(8)	0.517
V1 – F1	2.176(1)	0.276
		$\Sigma V1 = 3.942$

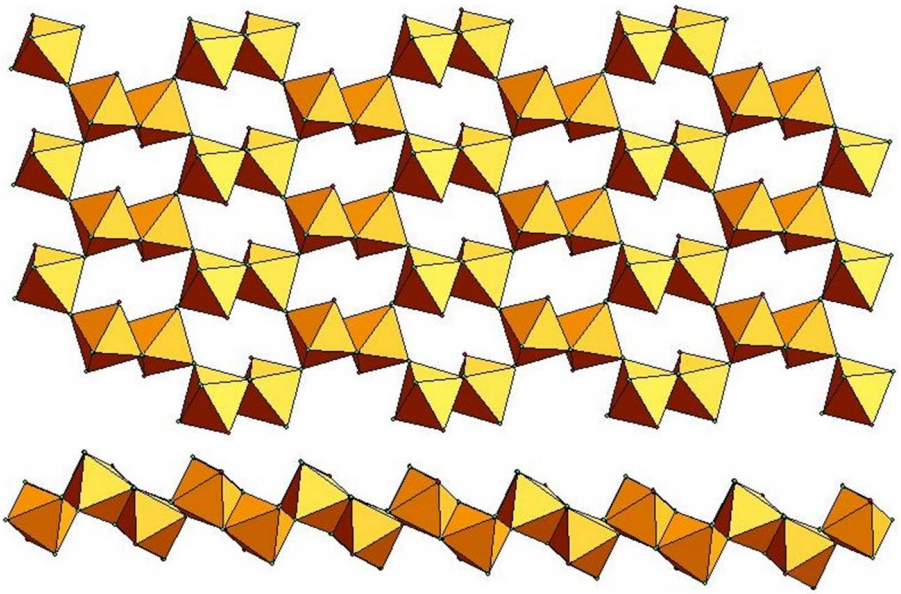

Fig. 5. 27: Structure of VOF_3: Layer built up of corner and edge-sharing V (V) octahedral units (top), and the zig-zag conformation seen when the layer is viewed parallel to the plane (bottom).

While the layers stack in a similar manner, they are set in such a manner in V-15 that the zig-zag conformation runs anti-parallel with each layer (Fig. 5. 26), and in VOF_3 the layers run parallel with each other (Fig. 5. 28).

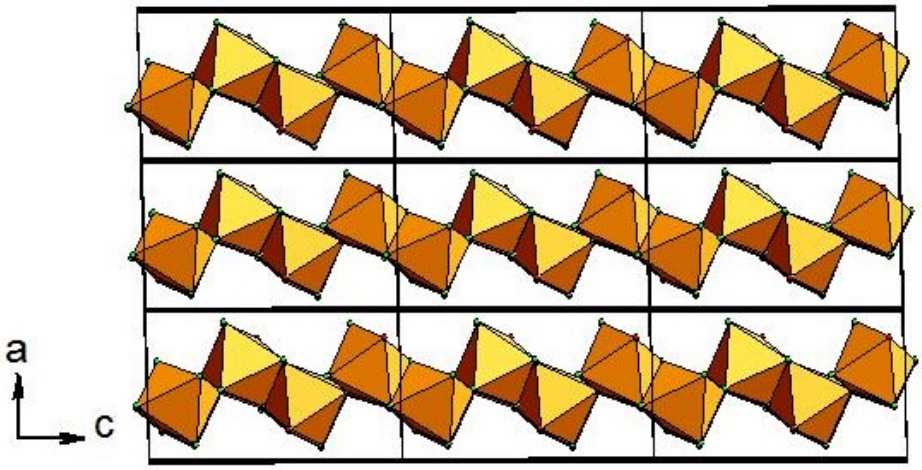

Fig. 5. 28: The extended 2x2 unit cell of VOF_3 viewed along axis *b* showing the separation between the V (V) layers.

The V – V inter-layer distances in V-15 are considerably longer, by 0.58 Å, than in VOF_3 due to the absence of hydrogen bonding in VOF_3. V – V bond lengths for both structures are given in Table 5. 18. V-15 was synthesised hydrothermally under oxidative conditions, which is unusual for this type of reaction since most are carried out under reduction. Initially it was hoped that the selenious acid would act to increase the connectivity of the compound and possibly impart its three-fold symmetry on the overall structure, acting as a template. However, no selenium was incorporated into the structure, and it simply acted as an oxidising agent, making this a purely V(IV) layered compound. This is an interesting discovery, as it is the first example of a purely V(IV) layered compound to be synthesised without the use of ionic liquids.

Table 5. 18: V – V distances for $V_2O_2F_2(H_2O)_2.H_2O$ V-15 and VOF_3.

Compound	V – V distance edge-shared (Å)	V – V distance corner-shared (Å)	V – V distance inter-layer (Å)
$V_2O_2F_4(H_2O)_2.H_2O$	3.330(2)	3.704(5)	5.650(8)
VOF_3	3.131(4)	3.871(3)	5.070(6)

DC magnetic susceptibilities for V-15 were measured in an applied field of 1.5 T from 2 K to 300 K. This was done in a zero field cooled (ZFC) and field cooled (FC) cycle. The data were fitted using a Curie-Weiss plot at three different temperature regions, yielding three different Weiss temperatures extracted from the fits (Fig. 5. 29). The high temperature region, 150 K to 300 K, yields a positive Weiss temperature indicating ferromagnetic interactions. The two low temperature regions yield negative Weiss temperatures, indicating antiferromagnetic interactions. A full list of extracted Curie constants and Weiss temperatures along with estimated μ_{eff} values are given in Table 5. 19. Single crystal diffraction measurements were carried out at 290 K, 173 K, and 140 K, which did not show any phase changes over the measured range. This indicates that the ferromagnetic to antiferromagnetic switching is not due to structural changes.

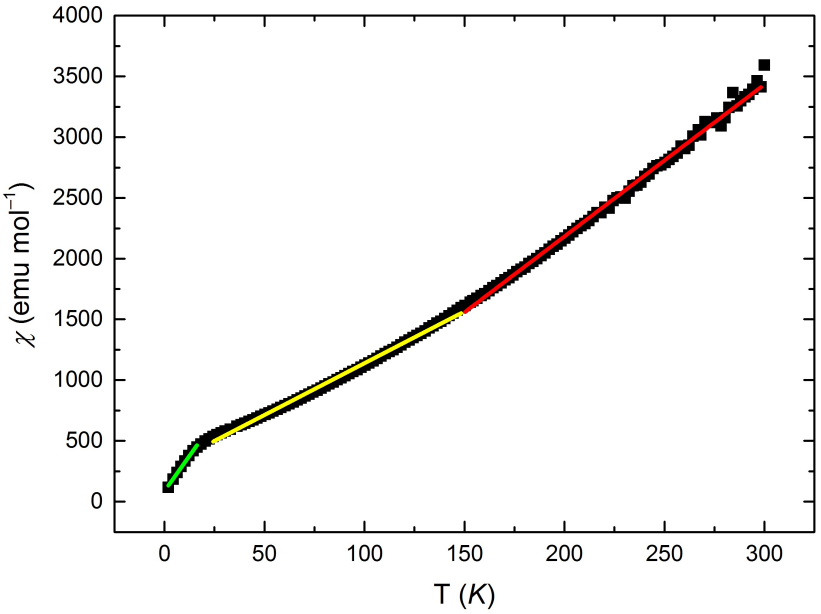

Fig. 5. 29: Inverse susceptibility plots of V-15 for the three separate temperature regions. The red line is the high T fit yielding a positive Weiss temperature, the yellow and green lines are the low T fits, each yielding negative Weiss temperatures.

Table 5. 19: Weiss temperatures, Curie constants and effective magnetic moments for V-15 at the specified temperature region.

Temperature region (K)	Weiss temperature, θ (K)	Curie constant, C, (K emu mol^{-1})	μ_{eff}, (μB)
300 – 150	25.363(1)	0.080(2)	0.80
150 – 25	-33.660(6)	0.117(9)	0.98
20 - 2	-3.736(5)	0.043(1)	0.59

This magnetic crossover is also seen in In_2VO_5, occurring at 120 K instead of 150 K as seen in V-15.[22] The calculated values of μ_{eff} for V-15 are considerably lower (0.91 μB) compared with μ_{eff} values for $S = ½$ magnetic moments (1.73 μB). This is most likely due to the inclusion of V (V) impurities in the sample, so these values are perhaps not overly reliable, and no evidence can be found in the literature for this sort of magnetic behaviour in vanadium samples.

The theoretical pattern of the single crystal structure was compared to its experimental pattern (Fig. 5. 30). It was also compared to VOF_3 since the layers are of a similar structure, and to see if the V(V) impurities were caused by this compound (Fig. 5. 30). It can clearly be seen that V-15 does not compare well to VOF_3, but the sample itself is relatively pure when compared to the theoretical pattern. There does appear to be a preferred orientation problem with the sample however, as the peaks are in the right places, but the intensity is not.

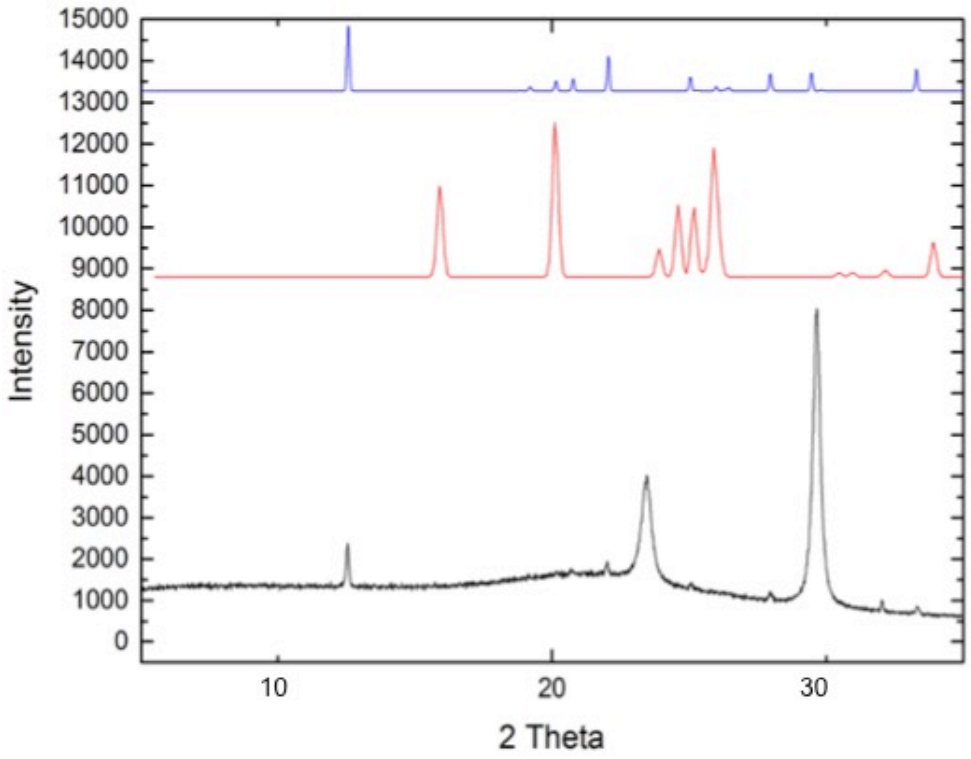

Fig. 5. 30: The theoretical pattern of V-15 (top, blue), the experimental pattern of V-15 (bottom, black) and the comparison to VOF_3 (middle, red).

5.7 Conclusions

Out of the seven crystal structures described in this chapter, five were prepared using solvothermal/hydrothermal methods, while V-14 was prepared ionothermally and V-12 was prepared as an aqueous reaction. These experiments produced a range of products with oxidation states varying from V(III) to V(V) and morphologies from 0D monomers to 2D layers.

Once again it can be seen that temperature plays a large role in the formation of these compounds and their dimensionality. V-10, $Cs_2V_2O_3(SO_4)_2$ and V-11, $Rb_2VF_3(SO_4)$ are both chain compounds which incorporate sulphate anions into their structure. V-10 was synthesised at 100 ^oC and exhibits two chains of corner-sharing V(IV) octahedral, bi-capped by sulfate tetrahedral units, that are connected via shared corners with V(IV) square planar units. However V-11 was synthesised at 160 ^oC, and exhibits a single chain of corner-sharing V(III) octahedral units bi-capped by sulfate tetrahedral units. So, in V-11, the higher temperatures have once again reduced the vanadium from its V(V) starting oxidation state down to V(III), while in V-10 the lower temperatures have kept the vanadium in its V(IV) oxidation state from its V(IV) starting material. V-10 would be an ideal candidate to try in a reaction with ionic liquid, since it stays as V(IV) using ethylene glycol as a solvent and displays a higher dimensionality chain than V-10, it seems probable that it may form a V(IV) layer, capped by sulfate tetrahedral units, at higher temperatures.

V-13, $[CN_3H_6]_3[VF_6]$, V-14, $[CN_3H_6]V_2O_2F_5]$, and V-16, $[CN_3H_6]_3[V_2O_2F_7]$ are all very different compounds in terms of crystal structure and oxidation state, but share a common guanidine moiety. V-13 was prepared using a mix of water and ethylene glycol, which has acted as a reducing agent in combination with the high temperature of 160 ^oC to lower the vanadium oxidation state from (V) to (III). V-16 was prepared using only water as a solvent, with the high temperature reducing the oxidation state of vanadium from (V) to (IV). Both V-13 and V-16 a 0D

structures, V-13 is a cubic monomer and V-16 is a monoclinic dimer. V-14 was prepared using VOF_3 as a starting material with IL as a solvent, which has allowed the compound to adopt a 2D layer, while the high temperature has lowered the vanadium oxidation state from (V) to (IV).

While ILs are very useful in the synthesis of higher dimensionality V(IV) compounds, they are very expensive to synthesise. If the method used in the production of V-15, $[V_2O_2F_2(H_2O)_2].H_2O$, could be refined and made more reliable this would be very useful, as not only is water much cheaper than IL, it is also much less time consuming to come by, as no lengthy synthetic procedure is required to obtain it.

The main issue with these samples is phase purity, and how to improve it. In some cases, a simple adjustment of reactant ratios or solvent choice solved the problem, but this was quite a time consuming process. In many cases it was not possible to obtain pure samples and the desired crystalline products had to be separated from the black residue by use of sieving or sonication. Examples of reaction conditions and products can be found in the supplementary information; these will give an idea of the scope of the experiments carried out during this work.

5.8 References

1. G. M. Sheldrick, *Acta. Cryst.*, 2008, **64**, 112-122.
2. T. Amemiya, M. Yano, K. Morita, T. Umegaki, T. Ono, H. Tanaka, K. Fujii and H. Uekusa, *Phys. Rev. B*, 2009, **80**, 100406-100401 - 100406-100404.
3. E. Williams, S. Morris and M. Weller, *Dalton Trans.*, 2012, **41**, 10845-10853.
4. R. Finn, J. Zubieta and R. Haushalter, *Prog. Inorg. Chem.*, 2003, **51**, 421-601.
5. J. Olshansky, T. Tran, K. Hernandez, M. Zeller, P. Halasyamani, J. Schrier and A. Norquist, *Inorg. Chem.*, 2012, **51**, 11040-11048.
6. G. Huan, J. W. Johnson, A. J. Jacobson, D. P. Goshorn and J. S. Merola, *Chem. Mater.*, 1991, **3**, 539-541.
7. G. M. B. Vaughan, J. Gaubicher, T. le Mercier, J. Angenault, M. Quarton and Y. Chabre, *J. Chem. Mater.*, 1999, **9**, 2809-2812.
8. M. G. Johnston and W. T. A. Harrison, *Acta. Cryst., Section C: Cryst. Struct. Comm.*, 2007, **63**, 57-59.
9. A. V. Lavrov, V. P. Nikolaev, G. G. Sadikov and M. A. Porai Koshits, *Doklady Akademii Nauk SSSR*, 1982, **266**.
10. P. S. Berdonosov, A. V. Olenev and V. A. Dolgikh, *Cryst. Rep.*, 2012, **57**, 200-204.
11. M. Jinxiao, W. Chengxin, C. Ning, L. Rong and P. Yuanming, *J. Solid State Chem.*, 2010, **183**, 2763 2769
12. E. Alter and R. Hoppe, *Z. Anorg. Allg. Chem.*, 1975, **412**, 110-120.
13. K. Waltersson, *Cryst. Struct. Commun.*, 1978, **7**, 507-511.
14. G. Pausewang, *Z. Anorg. Allg. Chem.*, 1971, **381**, 189-197.
15. N. Bucholz, M. Leimkuhler, L. Kiriazis and R. Mattes, *Inorg. Chem.*, 1988, **27**, 2035-2039.
16. M. HIlbers, M. Leimkuhler and R. Mattes, *Z. Naturforsch., B: Chem. Sci.*, 1989, **44**, 383-388.
17. P. Bukovec, S. Milicev, A. Demsar and L. Golic, *J. Chem. Soc., Dalton Trans.*, 1981, 1802-1806.
18. M. Lozinesk, E. Goreshnik and B. Zemva, *Z. Anorg. Allg. Chem.*, 2012, **638**,

2123-2128.

19. D. W. Aldous, N. F. Stephens and P. Lightfoot, *Dalton Trans.*, 2007, 2271-2282.
20. D. W. Aldous, N. F. Stephens and P. Lightfoot, *Dalton Trans.*, 2007, 4207-4213.
21. F. H. Aidoudi, C. Black, K. S. A. Arachchige, A. M. Z. Slawin, R. E. Morris and P. Lightfoot, *Dalton Trans*, 2013, **00**, 1-8.
22. S. A. J. Kimber, M. A. de Vries, J. Sanchez-Benitez, K. V. Kamanev and J. P. Attfield, *Phys. Rev. B*, 2008, **77**, 1-10.

6.0 Summary and Conclusions

The main aim of the project was to synthesise new vanadium-containing materials that were magnetically active, specifically $S = ½$ extended layer compounds. An initial exploration into vanadium compounds was carried out using hydrothermal and solvothermal synthetic methods. After several 1D chain and ladder-like compounds had been produced by these methods, ionic liquids were synthesized and used in ionothermal synthesis to try and increase the dimensionality of the products.

$KVOF_3$-α (V-1), $KVOF_3$-β (V-2), $RbVOF_3$-α (V-3), $RbVOF_3$-β (V-4), $CsVOF_3$ (V-5), $[NH_4]_2VF_5$-α (V-8), $[NH_4]_2VF_5$-β (V-7), K_2VF_5 (V-9), $Cs_2V_2O_2(SO_4)_2$ (V-10), $Rb_2VF_3(SO_4)$ (V-11), $[H_4TETA]_2[V_{10}O_{28}].4H_2O$ (V-12), $[CN_3H_6]_3[VF_6]$ (V-13) and $[CN_3H_6]_3[V_2O_2F_7]$ (V-16) were all synthesised *via* traditional hydrothermal and solvothermal reduction reactions at temperatures between 60 ^oC and 200 ^oC. These reactions produced a mixture of vanadium-containing compounds from monomers and dimers to chains, ladders and clusters.

$[NH_4]VOF_3$ (V-6) and $[CN_3H_6][V_2O_2F_5]$ (V-14) were produced *via* ionothermal synthesis techniques at 160 ^oC. V-14 condensed into a 2D layer structure, while also retaining its V^{4+} oxidation state, in contrast to the hydrothermally produced samples, which, even if the V^{4+} oxidation state was retained, the samples tended to remain as 0D or 1D structures.

One exception to this was V-15, $[V_2O_2F_2(H_2O)_2].H_2O$, which was produced via a solvothermal reaction, but starting with V(III) and oxidizing to V(IV) while also condensing into a new layered material solely comprised of V(IV).

All of the materials above were fully structurally characterised using single crystal and powder X-ray diffraction, and some were physically characterised using SQUID magnetometry where appropriate.

Two pseudo-kagome copper (II) selenite compounds, $Cu_3YSeO_3)_2O_2Cl$ (Cu-1) and $Cu_3L(SeO_3)_2O_2Cl$ (Cu-2) based on $Cu_3Bi(SeO_3)_2O_2Br$ were synthesized by solid state methods. A detailed powder neutron diffraction study was carried out on these compounds to monitor the evolution of magnetic structure at low temperature. A magnetic model was produced from the refinements of the data for both compounds. The magnetic ground state of the compounds can be described as ferromagnetic layers with antiferromagnetic interlayer coupling.

Phase purity, particularly where the traditional solvothermal experiments were concerned, was a big issue during this project. Samples produced generally contained at least a small amount of impurity even after several attempts at modifying the reactions to produce purer samples. Examples of reactions, found in the supplementary information, which detail the experimental procedures that were used and modified in attempts to synthesise and purify each compound.

7.0 Further work

Although 1443 syntheses were carried out during this work, these are detailed in the supplementary information, with many other reactions that could yet be performed to synthesise related new materials. Reactant ratios could be altered, as well as solvent volume and concentration in solvothermal type reactions. Further study into ionothermal synthesis could provide more layered compounds, perhaps using molybdenum and titanium, since they can also readily adopt $S = ½$ configurations, in place of vanadium and copper. Tables detailing reactions that were carried to synthesise all compounds discussed during this work are given in the supplementary information.

A more detailed exploration of the solvothermal synthesis of the V-15, $[V_2O_2F_2(H_2O)_2].H_2O$, layer would be useful for producing more layered compounds without the use of the expensive ionic liquids. Other metal centres that readily adopt a $S = ½$ configuration could also be tried here, as well as attempting to incorporate different cationic species to template the structure and see if they have any effect on the type of layer that is produced.

Attempts to synthesise copper-containing kagome compounds using hydrothermal or solvothermal methods would be worthwhile looking into, perhaps also using ionic liquids. Tellurite analogues of the selenite compounds studies here could also be prepared to see if there are any structural or physical effects that occur.

Appendix A: Atomic coordinates

Table A. 1: Atomic coordinates for $KVOF_3$- α (V-1).

Atom site	*x*	*y*	*z*	Uiso
V1	0.14676(8)	0.25435(3)	0.31798(6)	0.0084(4)
K1	0.10779(7)	0.000000	0.76375(8)	0.0131(5)
K2	0.35161(6)	0.000000	1.13860(3)	0.0143(5)
F1	0.13299(1)	0.000000	0.37748(8)	0.0312(6)
F2	0.18968(2)	0.28570(6)	0.59947(7)	0.0072(3)
F3	0.18799(4)	0.500000	0.27338(9)	0.0168(6)
F4	0.16223(1)	0.19888(2)	0.07439(4)	0.0208(7)
O1	0.02513(1)	0.29409(2)	0.28261(2)	0.0077(6)

Table A. 2: Atomic coordinates for $KVOF_3$- β (V-2).

Atom site	*x*	*y*	*z*	Uiso
V1	0.63636(7)	-0.00405(6)	0.60302(8)	0.0092(1)
K1	-0.08898(2)	0.250000	0.40027(4)	0.0121(3)
K2	0.17644(7)	0.250000	0.64386(8)	0.0147(1)
F1	0.57323(8)	0.250000	0.61377(7)	0.0145(6)
F2	0.69928(4)	-0.250000	0.55981(4)	0.0149(6)
F3	0.88799(3)	0.05370(6)	0.58559(4)	0.0112(3)
F4	0.37515(2)	-0.03690(1)	0.56086(4)	0.0096(1)
O1	0.61998(7)	-0.04409(4)	0.72302(4)	0.0224(3)

Table A. 3: Atomic coordinates for $RbVOF_3$-α (V-3).

Atom site	*x*	*y*	*z*	Uiso
V1	0.000000	0.19237(2)	1.01711(1)	0.0158(5)
Rb1	0.500000	-0.00681(6)	0.71968(6)	0.0169(5)
F1	0.000000	0.03205(1)	0.89664(8)	0.0484(5)
F2	0.000000	0.26946(9)	1.16936(6)	0.0499(8)
F3	-0.500000	0.17027(2)	1.02917(6)	0.0112(3)
O1	0.000000	0.34559(7)	0.93913(2)	0.0813(2)

Table A. 4: Atomic coordinates for $RbVOF_3$-β (V-4).

Atom site	*x*	*y*	*z*	Uiso
V1	0.15766(1)	0.91354(2)	-0.500000	0.0114(7)
Rb1	0.20092(5)	0.66980(8)	0.000000	0.0177(2)
F1	0.15228(7)	1.04575(3)	-0.500000	0.0108(2)
F2	0.04518(2)	0.79565(1)	-0.500000	0.0205(4)
F3	0.11706(3)	0.91519(1)	-1.000000	0.0184(5)
O1	0.38893(8)	0.89458(5)	-0.500000	0.0130(2)

Table A. 5: Atomic coordinates for $CsVOF_3$ (V-5).

Atom site	*x*	*y*	*z*	Uiso
V1	0.17915(2)	0.96904(2)	0.00000	0.0041(4)
Cs1	-0.00408(6)	0.70451(6)	0.50000	0.0088(3)
F1	0.04396(6)	1.10082(5)	0.00000	0.0071(2)
F2	0.15577(5)	0.96510(5)	-0.50000	0.0133(4)
F3	0.23301(6)	0.81230(5)	0.00000	0.0091(3)
O1	0.33628(7)	1.03303(6)	0.00000	0.0109(5)

Table A. 6: Atomic coordinates for $[NH_4]VOF_3$ (V-6).

Atom site	*x*	*y*	*z*	Uiso
V1	0.000000	0.19270(3)	0.98419(8)	0.0092(3)
N1	-0.500000	0.50629(1)	0.78039(8)	0.0162(8)
F1	0.000000	0.02986(7)	1.10218(7)	0.0471(6)
F2	-0.500000	0.16971(8)	0.96977(3)	0.0076(5)
F3	0.000000	0.27447(6)	0.83336(5)	0.0616(3)
O1	0.000000	0.34347(5)	1.06355(9)	0.0779(2)

Table A. 7: Atomic coordinates for $[NH_4]_2VF_5$-β (V-7).

Atom site	*x*	*y*	*z*	Uiso
V1	0.250000	0.32977(4)	0.56719(7)	0.0222(7)
N1	0.250000	0.83435(3)	0.59149(5)	0.0170(2)
N2	0.250000	0.50118(9)	0.27789(4)	0.0105(5)
F1	0.000000	0.500000	0.500000	0.0243(5)
F2	0.250000	0.49550(6)	0.69025(3)	0.0257(3)
F3	0.250000	0.21269(7)	0.42445(3)	0.0309(6)
F4	0.01411(1)	0.19945(7)	0.61840(5)	0.0510(2)

Table A. 8: Atomic coordinates for $[NH_4]_2VF_5$-α (V-8).

Atom site	*x*	*y*	*z*	Uiso
V!	0.000000	0.500000	0.000000	0.0207(9)
N1	0.42620(9)	0.250000	0.19553(3)	0.0260(6)
N2	-0.00733(6)	0.750000	0.36299(3)	0.0402(1)
F!	0.08532(8)	0.250000	0.01319(3)	0.0328(9)
F2	0.10883(1)	0.53080(2)	0.15947(1)	0.0472(1)
F3	0.27033(8)	0.55166(8)	-0.06483(7)	0.0301(9)

Table A. 9: Atomic coordinates for K_2VF_5 (V-9).

Atom site	*x*	*y*	*z*	Uiso
V1	0.250000	0.17135(2)	0.56256(8)	0.01256(3)
K1	0.250000	-0.34084(1)	0.585975(3)	0.0142(1)
K2	0.250000	-0.01435(7)	0.27363(3)	0.0155(1)
F1	0.000000	0.000000	0.500000	0.0172(6)
F2	0.00843(2)	0.32182(1)	0.61426(3)	0.0134(9)
F3	0.250000	0.02586(2)	0.69690(4)	0.0251(5)
F4	0.250000	0.27676(8)	0.40975(3)	0.0245(9)

Table A. 10: Atomic coordinates for $Cs_2V_2O_3(SO_4)_2$ (V-10).

Atom site	*x*	*y*	*z*	Uiso
V1	0.44903(7)	0.41839(5)	0.13206(10)	0.0045(1)
V2	0.24339(3)	1.04034(4)	0.49520(9)	0.0363(8)
Cs1	0.44489(2)	0.64694(5)	0.27595(1)	0.0133(10)
Cs2	0.44593(6)	0.87871(4)	0.07645(9)	0.0388(2)
S1	0.44062(1)	1.13395(11)	0.33075(4)	0.0190(4)
S2	0.46709(7)	0.73155(6)	0.42511(6)	0.0011(3)
O1	0.45873(4)	0.35551(6)	0.18853(5)	0.0395(3)
O2	0.45261(10)	1.04496(6)	0.28464(8)	0.0209(1)
O3	0.48394(7)	1.30688(5)	0.32414(3)	0.0717(4)
O4	0.23989(5)	1.05914(6)	0.367781(0)	0.0596(7)
O5	0.71026(3)	1.11561(6)	0.35425(14)	0.0836(10)
O6	0.47307(1)	0.85305(7)	0.46711(5)	0.0115(8)
O7	0.43387(8)	0.57470(12)	0.44485(10)	0.0485(9)
O8	0.19250(1)	0.73400(3)	0.3983(14)	0.0280(1)
O9	0.65211(4)	0.77627(10)	0.38964(5)	0.0596(10)
O10	0.41234(9)	1.18590(2)	0.47462(9)	0.0161(2)
O11	0.45229(10)	0.50536(10)	0.05890(3)	0.0351(9)

Table A. 11: Atomic coordinates for $Rb_2VF_3(SO_4)$ (V-11).

Atom site	*x*	*y*	*z*	Uiso
V1	0.000000	0.500000	0.500000	0.0060(5)
Rb1	0.19925(1)	0.82583(3)	0.69205(6)	0.0163(4)
S1	0.250000	0.19339(1)	0.500000	0.0098(5)
F1	0.02121(3)	0.45008(6)	0.33756(6)	0.0112(8)
F2	0.250000	0.59149(8)	0.500000	0.0035(7)
O1	0.09835(8)	0.29486(2)	0.55094(2)	0.0117(4)
O2	0.17460(4)	0.10454(7)	0.40391(3)	0.0150(5)

Table A. 12: Atomic coordinates for $[H_4TETA]_3[V_{10}O_{28}].4H_2O$ (V-12).

Atom site	*x*	*y*	*z*	Uiso
V1	0.16133(2)	0.52690(9)	0.51384(3)	0.0095(3)
V2	0.21332(4)	0.24701(7)	0.47811(8)	0.0105(2)
V3	0.04074(8)	0.28994(2)	0.73392(9)	0.0088(7)
V4	0.32599(6)	0.48295(8)	0.25477(8)	0.0101(4)
V5	-0.02680(4)	0.56676(1)	0.77059(1)	0.0121(8)
C1	-0.14905(4)	0.14500(7)	1.28583(2)	0.0135(10)
C2	-0.22038(10)	0.21999(2)	1.15449(3)	0.0135(1)
C3	0.48088(6)	0.23024(4)	0.80178(4)	0.0056(9)
C4	0.49728(8)	0.20955(7)	0.93840(3)	0.0115(3)
C5	0.37893(8)	0.78787(3)	0.40599(7)	0.0098(4)
C6	0.22518(9)	0.85728(1)	0.48577(5)	0.0121(3)
N1	-0.10484(7)	0.14409(9)	1.06566(2)	0.0140(7)
N2	0.73292(9)	0.21540(3)	0.37672(5)	0.0108(8)
N3	-0.34953(4)	1.18109(6)	0.72721(9)	0.0086(5)
N4	0.32327(9)	0.26949(3)	0.99994(3)	0.0108(7)
O1	0.01312(6)	0.71770(3)	0.41982(8)	0.0062(5)
O2	0.22682(5)	0.32733(7)	0.60057(2)	0.0043(3)
O3	0.07867(9)	0.48110(1)	0.38722(2)	0.0006(7)
O4	0.33673(3)	0.52782(7)	0.40888(1)	0.0071(4)
O5	0.18127(4)	0.56525(5)	0.63725(4)	0.0084(4)
O6	0.07897(8)	0.36958(2)	0.82526(5)	0.0056(8)
O7	0.13592(10)	0.12162(9)	0.81215(2)	0.0106(2)
O8	0.311071(4)	0.08034(10)	0.55617(8)	0.0090(2)
O9	-0.23771(1)	0.55776(3)	0.84316(5)	0.0101(1)
O10	-0.18188(3)	0.32107(9)	0.80361(8)	0.0095(2)
O11	0.39336(6)	0.29585(9)	0.37243(9)	0.0085(8)
O12	0.13186(10)	0.24704(2)	0.35074(1)	0.0067(2)
O13	0.50593(9)	0.48812(6)	0.17810(8)	0.0115(7)
O14	0.02663(8)	0.60255(3)	0.87096(2)	0.0151(4)

Table A. 13: Atomic coordinates for $[CN_3H_6]_3[VF_6]$ (V-13).

Atom site	*x*	*y*	*z*	Uiso
V1	0.000000	0.000000	0.000000	0.0126(2)
V2	0.000000	0.000000	0.500000	0.0126(2)
C1	-0.02727(2)	-0.23435(1)	0.24881(6)	0.0185(2)
N1	-0.02434(5)	-0.14073(8)	0.24792(4)	0.0412(3)
N2	-0.01650(4)	-0.27988(7)	0.33077(5)	0.0389(9)
N3	-0.04045(3)	-0.28134(8)	0.16888(1)	0.0392(10)
F1	-0.02489(8)	0.02780(10)	0.13291(4)	0.0223(7)
F2	0.02645(6)	0.02031(12)	0.36612(5)	0.0226(12)

Table A. 14: Atomic coordinates for $[CN_3H_6]x[V_2O_2F_5]$ (V-14).

Atom site	*x*	*y*	*z*	Uiso
V1	0.50822(9)	0.89082(4)	0.31782(3)	0.0014(9)
V2	0.49142(5)	1.07368(10)	0.18040(7)	0.0236(10)
V3	1.00338(6)	1.07343(8)	0.18047(6)	0.0067(4)
V4	0.99902(3)	0.89073(13)	0.31829(9)	0.0266(6)
C1	0.29310(3)	0.73719(2)	0.06998(1)	0.0466(9)
C2	0.78212(6)	0.72708(8)	0.08157(6)	0.0362(9)
N1	0.73386(4)	0.73840(2)	0.14753(3)	0.0437(8)
N2	0.22396(2)	0.73487(8)	0.13418(6)	0.0413(4)
N3	0.80154(6)	0.82188(9)	0.0420(10)	0.0914(7)
N4	0.34140(9)	0.63764(7)	0.03941(2)	0.1356(4)
N5	0.32429(1)	0.82930(5)	0.03168(3)	0.0762(9)
N6	0.81382(1)	0.62669(3)	0.05150(2)	0.0985(4)
F1	0.54626(6)	1.05218(4)	0.29860(6)	0.0245(8)
F2	0.46035(10)	0.91152(7)	0.20108(7)	0.0028(5)
F3	0.96636(7)	1.05215(2)	0.29816(11)	0.0029(7)
F4	1.03544(1)	0.91151(8)	0.20134(7)	0.0384(4)
F5	0.95062(3)	1.23036(1)	0.20210(3)	0.0220(7)
F6	0.54565(4)	1.23192(2)	0.20141(8)	0.0223(9)
F7	0.75200(9)	1.03916(9)	0.17282(10)	0.0593(3)
F8	0.24700(5)	1.10347(1)	0.21389(8)	0.0012(9)
F9	0.25594(10)	0.92437(7)	0.32590(4)	0.0196(7)
F10	0.74978(10)	0.86072(2)	0.28518(13)	0.0382(1)
O1	0.55402(6)	0.88902(4)	0.40533(1)	0.0227(7)
O2	0.96498(4)	0.88831(9)	0.40450(1)	0.0540(7)
O3	0.44845(4)	1.07673(5)	0.09319(2)	0.0232(2)
O4	1.03303(5)	1.07634(8)	0.093047()	0.0218(3)

Table A. 15: Atomic coordinates for $[V_2O_2F_2(H_2O)_2].H_2O$ (V-15).

Atom site	*x*	*y*	*z*	Uiso
V1	0.18501(6)	0.19659(3)	0.61920(10)	0.0090(2)
F1	0.19757(2)	0.45144(6)	0.46661(7)	0.0150(1)
F2	0.21057(5)	-0.11694(2)	0.74641(5)	0.0147(5)
O1	0.10714(7)	-0.06838(3)	0.47757(6)	0.0157(7)
O2	0.09779(9)	0.33928(3)	0.66570(9)	0.0144(5)
O3	0.000000	0.19756(2)	0.250000	0.0155(3)

Table A. 16: Atomic coordinates for $[CN_3H_6]_3[V_2O_2F_7]$ (V-16).

Atom site	*x*	*y*	*z*	Uiso
V1	0.03837(18)	0.69876(6)	0.34471(3)	0.0284(3)
C1	0.06492(8)	0.36436(3)	0.42510(9)	0.0192(1)
C1	0.500000	0.53255(3)	0.250000	0.0186(2)
N1	0.500000	0.63568(8)	0.250000	0.0114(8)
N2	0.06566(9)	0.26139(4)	0.42663(3)	0.0186(4)
N3	-0.08956(6)	0.41627(10)	0.42637(7)	0.0212(8)
N4	0.65415(9)	0.48079(7)	0.25027(8)	0.0122(1)
N5	0.21790(4)	0.41593(5)	0.42496(4)	0.0237(4)
F1	-0.12977(4)	0.63863(12)	0.38677(6)	0.0290(2)
F2	0.000000	0.58793(2)	0.250000	0.0163(3)
F3	0.05108(10)	0.81723(3)	0.38967(8)	0.0301(5)
F4	0.16625(3)	0.75434(7)	0.25186(3)	0.0142(4)
O1	0.22885(8)	0.63950(8)	0.39097(5)	0.0161(4)